Charge separation of bouncing water drops on hydrophobic and superhydrophobic surfaces

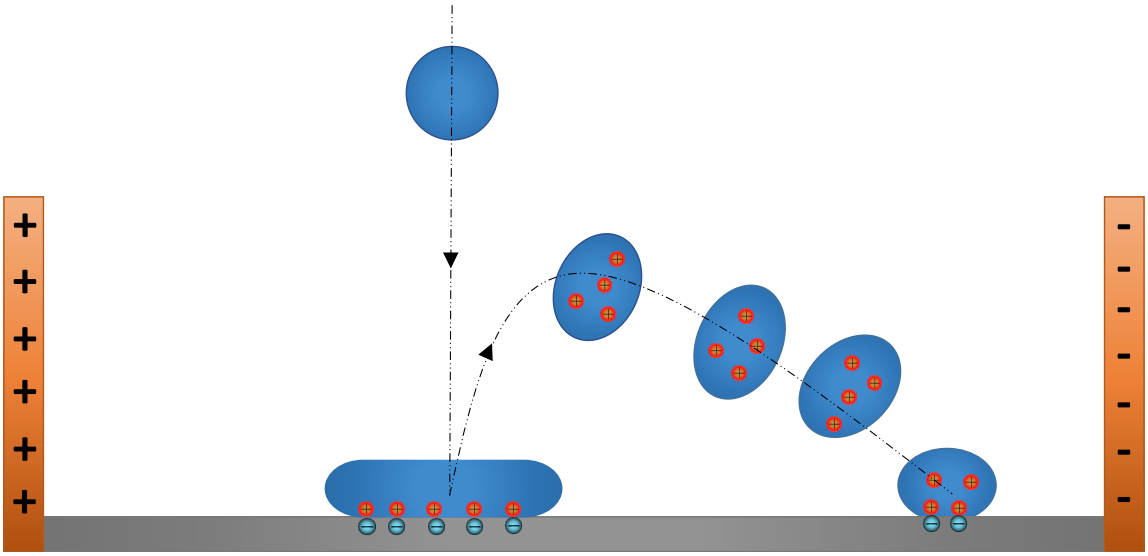

Dissertation

zur Erlangung des Grades

"Doktor der Naturwissenschaften" am Fachbereich Physik,

Mathematik und Informatik

der Johannes Gutenberg-Universität

in Mainz

Diego Díaz

geboren in Santiago de Chile, Chile

Mainz, den 20 Januar 2023

Supervisor: Prof. Dr. Hans-Jürgen Butt
Second supervisor: Prof. Dr. Joachim Elmers
Date of exam: 02.05.2023

Abstract

In this thesis, I investigate experimentally and theoretically the mechanism behind the charge separation of neutral water drops rebounding from *hydrophobic* and *superhydrophobic* surfaces. So far, charging by drop impact has not been systematically quantified and it is not clear which are the main parameters that control the process. In addition, a quantitative theoretical model to describe the phenomenon is missing.

To address these issues, I designed a method for drop charge detection based on electric fields and high-speed video imaging. The method allows to analyze the trajectory of bouncing drops deflected in an external lateral electric field upon impact. Coatings made of superhydrophobic silicone nanofilaments and hydrophobic Teflon were used as impact targets.

From the lateral deflection of drops rebounding from *superhydrophobic* surfaces, the following outcome was observed: when neutral water drops impact and rebound from both hydrophobic and superhydrophobic surfaces, they acquire a positive electrical charge, since the deflection is always in the direction of the applied electric field. Here, to understand the underlying physics of the phenomenon, I study the relative importance of five of these potential variables: impact speed, drop contact area, contact line retraction speed, drop size, and type of surface. I additionally derived a theoretical model based on a previously reported sliding drop electrification model. The model assumes that drops gain progressively positive charge during the drop retraction motion. Both theoretical and experimental results reveal that the maximum contact area is the main controlling parameter of the charging mechanism.

Drop charging on *hydrophobic* surfaces confirms the relevant influence of the contact area, with values of charge up to two order of magnitude higher than the observed for *superhydrophobic* surfaces. From the spontaneous charging on these surfaces, one important result was observed: Self-generated charges lead to significant electrostatic forces between the drop and surface. These forces affect the drop motion in two ways. First, the electrostatic forces slow down the

drop retraction motion. This motion takes place when drops, prior the rebound, convert back the excess of surface energy into kinetic energy after spreading on the surface. Second, the electrostatic forces reduce the maximum rebounding height. I calculated the electrostatic forces using an energy conservation approach. My results indicate that electrostatic forces on hydrophobic surfaces can be even stronger than gravitational forces, allowing to estimate the drop charge by energy conservation even in the absence of external electric fields.

The experimental method presented in this thesis is advantageous compared with other methods that require additional electronic devices for charge detection. More importantly, it is based on very fundamental physics. Furthermore, the findings could be useful for the control of drop charging in energy harvesting applications. From a fundamental viewpoint, the results of this thesis serve to describe drop impact not only in terms of surface energy, viscous dissipation energy, gravitational potential energy and kinetic energy, but also including the energy dissipated by electrostatic forces.

Contents

List of Figures

Chapter 1

Introduction

Drop impact on solid surfaces is a phenomenon present in nature and of great importance for different industrial applications. In nature, raindrops can impact stones and soil, which leads to aerosol generation in the environment [1]. Water drops can also spread pathogens upon the impact on leaves [2], as well as helps in the water storage of plants [3]. In industrial applications, examples are anti-icing [4], spray coating [5], erosion [6], ink jet printing [7], spray cooling [8] and self-cleaning [9]. The self-cleaning is a property observed in lotus leaves and refers to the ability to be cleaned by water drops [10, 11]. Special interest has attracted the replication of self-cleaning for different surfaces [12–16]. This is relevant for the removal of impurities on materials by drop impact in form of raindrops or spray drops.

Although drop impact has been studied for more than one hundred years, there is still some questions about the physical mechanisms of this phenomenon, specifically the electrification of drops. It is well known that drops impacting on solid surfaces may lead to charge separation. A rebounding drop usually leaves back a negatively the surface charged and charges positively itself [17–20]. When water drops impact on a surface, the moving three-phase contact line can induce charge separation at the solid-liquid interface. Most of the studies suggest the formation of an electrical double layer at the solid-liquid interface in electrical equilibrium. Therefore, if this double layer is disrupted, the electrical equilibrium is broken, which is actually what a moving contact line may gener-

ate. However, all charge separation processes that involves the movement of the three-phase contact line are not well understood. There are several reasons for this lack of understanding. First, charge separation processes caused by flowing liquids are all taking place far from equilibrium. As a result, finding a theory to describe them is difficult to base on equilibrium thermodynamics. Second, like contact electrification between solids, experiments are often not easy to reproduce. Usually only qualitative agreement is obtained from experiment to experiment and laboratory to laboratory. Quantifying the effects, however, turned out to be more difficult [21, 22]. Third, often different fundamental effects lead may contribute to a net charging and it is not obvious, which effect dominates.

In this thesis, I investigate the charge separation of drops impacting onto hydrophobic and superhydrophobic surfaces. To fully understand this phenomenon, it is required knowledge of (1) Wetting on different surfaces, (2) drop impact dynamics of bouncing drops, and (3) Fundamental basis of charge separation of sliding drops on hydrophobic surfaces. Here, I will focus mainly on these three aspects to describe the charging process of bouncing drops.

Since the charging may influence the dynamic wetting on surfaces [23–25] and allows the conversion of kinetic energy of flowing liquids in electric energy [26–36] the fundamental and applied motivation for the topic is well justified. Potential advantage over toher types of electric generators is that no moving parts are required. However, until now the efficiency of slide electrification is still much lower than other electric generators. Improvements in the efficiency strongly depends on the degree of control of charging. Thus, a better insight of the fundamental basis on charge separation becomes crucial for energy harvesting applications.

1.1 Historical Overview

Originally, the outcomes of drop impact like the splash and slide of water drops could only be observed by bare eye. Back then, little was known about the

wetting of drops on surfaces until 1805, when Thomas Young [37] explained the contact angle formed at the solid liquid-intephase in terms of the surface tensions at the solid-vapor, solid liquid, and liquid-vapor interphase. Years later, Worthington in 1876 appears with the earliest report of drop impact, which was focused on the study of the splash of water and mercury drops on horizontal plates [38]. He characterized the drop impact patterns by his own sketches from memory, as a result of the limitations of high speed-photography of the period. Then, in 1882 Worthington characterized the splashing produced by drops and solid spheres impacting on liquids with a more sophisticated setup, which showed the first well resolved-images of drop impact [39]. Few years later, the drop break up became an attractive topic due to the direct relation with electric charge separation in nature.

First studies of charge separation by drop impact started with Lenard in 1892 [17], who investigated one of the examples of charge separation present in nature: The waterfalls. Lenard observed a space of negative charge surrounding the waterfalls. In a similar way, Thomson (1894) measured the charge developed by impacting drops on surfaces coated with a thin film layer of the same liquid [18]. Both Lenard and Thomson noted that drops rebounding from a surface are usually positively charged while the surfaces tend to charge negatively. This observation was later confirmed for drops splashing on solid surfaces by Kähler in 1903 [40] and even almost 100 years later by Levin [19] and Chate [20]. Further studies of charge separation were performed in 1906, when, Simpsons studied the generation of electricity by raindrops [41]. He suggested that a mass of water may be broken into smaller drops positively charged by air currents before falling, which would explain the positive charge of rain. Later, based on experiments by Simpson [41], in 1914 Nolan allowed water drops to fall into a very strong horizontal air-current. Each drop as it entered the air-stream was immediately shattered [42]. He collected the drops in an electrometer and measured the charge per volume of received water. Since the drops were uncharged when leaving the dropper, charge was generated when splashing the drops with the air-blast. The more violent the air-blast and the smaller the daughter drops,

the more charge was collected. The generated charge increased with the total surface of the daughter droplets. Distilled water gave a larger charge than tap water with salt. From these and later experiments he concluded that positive charge is created when drops are split. This means that breaking up of drops leads to charge separation. In 1915, Lenard continued the study of splashing drops [43], which can be even more complex: Tiny secondary droplets tend to be negatively charged and the large fragments carry positive charges. To explain the process, Lenard in 1915 suggested that negative and positive layers of charge are present near the water-air interface These layers forms what is called the electrical double layer (EDL). When an impacting mass of water on a surface breaks up, this layer is disrupted leading to charge separation. Thus, the accumulation of charge can be explained with the ions naturally present in water.

Thanks to the advances in high-speed video imaging, the drop impact phenomenon started to be extensively studied with more detail. Nowadays, it is known that the drop impact outcome strongly depends on the surface properties such as the roughness and wettability. Wenzel [44] and Cassie [45] developed a model to describe the wetting behaviour as a function of the roughness. They pointed out that micro and nano scale roughness can substantially increase or decrease, depending whether the contact angle is smaller or larger than 90°. Water interacting with super water-repellent surfaces, so called superhydrophobic surfaces, has been studied intensively since the 1990s, mainly because of their water repellency and self-cleaning properties [10]. Many researchers have replicated the super water-repellent properties of the lotus leaf (superhydrophobicity) by combining new hydrophobic surface chemistry with a substantial roughness [46, 47]. Drops deposited on these surfaces can remain in the known Cassie-Baxter state [45], where the liquid does not penetrate into the grooves of the surface due to the entrapment of air pockets. However, most studies on superhydrophobicity are focused on their self-cleaning properties, but only few studies have described the phenomenon of charge separation by drop impact from a fundamental viewpoint. In fact, charging of drops on re-

pellent surfaces is certainly a quite new field. First studies involved the work of Miljkovic in 2013 [48]. He proved that water drops that condense and coalescence on a superhydrophobic surface, can jump off with a positive charge . Again, the existence of an EDL at the solid-liquid interface and a moving contact line was proposed as the main reason of charge separation. When the double layer is formed, hydroxyl ions from the drop would tend to be absorbed by fluoropolymer surfaces, leaving positive charge in the drop. This preference of hydrophobic surfaces to absorb negative charge (OH^-) from liquid water was also previously systematically studied [49–52]. Sun et. al. (2019) were the first to describe the charging of bouncing drops and a direct application of the phenomenon. They showed that drops can rebound positively charged from superamphiphobic surfaces, i.e, surfaces that repel water and other liquids [25]. More importantly, he showed the possibility to create surface charge gradients by drop impact on these surfaces to transport drops. Drops can negatively charge the surface at the region of the contact area. Therefore, as the surface is left negatively charged, drop impact at different impact speeds can create negative surface charge gradients.

Nowadays, many examples of drop charging that involve the contact line movement are found in literature. Drops sliding down a hydrophobic tilted plane usually acquire a positive charge and deposit a surface charge of opposite sign on the solid surface [53–59]. Therefore, a receding contact line tends to leave a charged surface behind. The term "slide electrification" was introduced in 1993 for the process by Yatsuzuka [53]. Recently, Stetten et. al proposed a quantitative model to describe slide electrification of drops on hydrophobic surfaces [57]. This model considers that a fraction of the total charge in the EDL is left on a surface as a drop slides. Slide electrification has been mainly explained as a result of absorption of hydroxyl ions naturally present in water to the hydrophobic surface, as suggested by Miljkovic for jumping droplets. This indicates a common cause of charge separation when a hydrophobic surface, specifically a fluoropolymer, interacts with water. However, Lin et. al in 2020 suggested that not only ion transfer occurs during charge separation,

but also electron transfer [60]. This new possible way of charge transfer would depend on the functional groups of the solid surface and becomes dominant for organic liquids. The charge separation in water drops has been also explained due to the dissociation of CO_2 from air in water, leading to the formation of bicarbonate ions. Negative ions concentrate in the water-air interface, whereas the positive ones in the bulk. Despite the contribution of the proposed models, the fundamental mechanism of charge separation by moving drops is still under debate.

Charge separation by moving drops has inspired the design of new energy harvesting methods to generate electric energy. However, the improvement of the efficiency of these applications requires a better understanding of the underlying physics behind the charge separation, specially for bouncing drops. In fact, only few examples of energy harvesting by bouncing drops on superhydrophobic surfaces can be found. There is no certainty about the main parameters controlling the charge separation by drop impact, nor a quantitative model to describe it. Furthermore, the reproducible quantification of drop charge has been difficult to achieve. In this thesis, I addressed all these issues. I reproducibly quantify the charge of bouncing drops by two different methods and propose a theoretical model based on the drop contact area as the controlling parameter of the charging process. I additionally identify the influence of self-induced electrostatic forces on the drop impact dynamics and the possibility to predict drop charging.

1.2 Overview of thesis

In the first chapter, I will introduce the gap of knowledge of charge separation by drop impact with its respective state of art. In addition, I will explain the fundamental theory and concepts of this thesis.

In chapter 2, I will describe an experimental method based on electric fields generation that I developed, for charge detection of drops rebounding from superhydrophobic and hydrophobic surfaces. Afterwards, I will describe the-

oretical simulations to probe homogeneity of the applied electric field. The method and the corresponding results on superhydrophobic surfaces have been published in *Soft Matter* [61].

In chapter 3, I will show and analyze the results of charge measurements of bouncing drops on superhydrophobic surfaces. I will provide evidence of the contact area as main parameter controlling the charge separation. Then, I will derive a theoretical model to explain charging of bouncing drops.

In chapter 4, I will investigate charging of drops rebounding from hydrophobic surfaces. I will describe two effects of self-generated electrostatic forces in the drop motion: (1) retardation of the retraction motion and (2) reduction of the maximum rebound height. Subsequently, I will calculate the electrostatic forces for each situation by an energy balance approach, which will serve to even predict the drop charge. Finally, I will provide further evidence of the contact area as crucial parameter in drop charging by using micropillar-array surfaces as impact targets. All these results have been published in *Physics of Fluids Journal* [62].

1.2.1 Publications associated with this thesis

- **Diego Díaz**, Diana Garcia Gonzalez, Pravash Bista, Stefan AL Weber, Hans-Jürgen Butt, Amy Stetten, and Michael Kappl. "Charging of drops impacting onto superhydrophobic surfaces." Soft Matter 18, 1628–1635 (2022).

- **Diego Díaz**, Xiaomei Li, Pravash Bista, Fahimeh Darvish, Hans-Jürgen Butt and Michael Kappl. "Self generated electrostatic forces of drops rebounding from hydrophobic surfaces". Physics of Fluids 35, 017111 (2023).

1.3 Wetting

1.3.1 Static Contact angle

The static contact angle or Young´s contact angle, Θ, is the equilibrium angle formed at three phase contact line a solid surface and a liquid surface (Fig. 1.1). The contact angle is a result of the interaction of the surface tensional forces of three interfaces: solid-liquid γ_{SL}, solid-vapor γ_{SA} and liquid-vapor γ_L interface. The line where the three phases are in contact is called the three-phase contact line. As the system is in equilibrium, on a smooth and flat surface the sum of the forces per unit length at the interfaces in the parallel direction to surface must be zero:

$$\gamma_{SA} - \gamma_{SL} - \gamma_L \cos\Theta = 0, \tag{1.1}$$

which leads to the well known Young´s equation [37]:

$$\cos\Theta = \frac{\gamma_{SA} - \gamma_{SL}}{\gamma_L} \tag{1.2}$$

If $\Theta = 0$, the liquid spreads completely on the surface. This means that γ_L equals the force contribution of γ_{SL} and γ_{SA}, so there is a complete wetting. For $\gamma_{SL} > \gamma_{SA}$, $\cos\Theta$ is positive and then Θ must be less than 90°. A surface is called hydrophilic when the angle formed with a water drop is $0° < \Theta < 90°$. On the other hand, if $\gamma_{SL} < \gamma_{SA}$, $\cos\Theta$ is negative and then Θ must be higher than 90°. Such surfaces are called hydrophobic. In practice, contact angles of flat, smooth hydrophobic surfaces can reach values of $\Theta = 120°$.

1.3.2 Surface roughness and heterogeneity

1.3.3 Wenzel state

If the surface has nano- or microstructures, then the surface has a degree of roughness. Wenzel described the effect of roughness on the wetting properties of a surface by adding a roughness ratio factor $r = A_{rough}/A_{flat}$ to the Young's

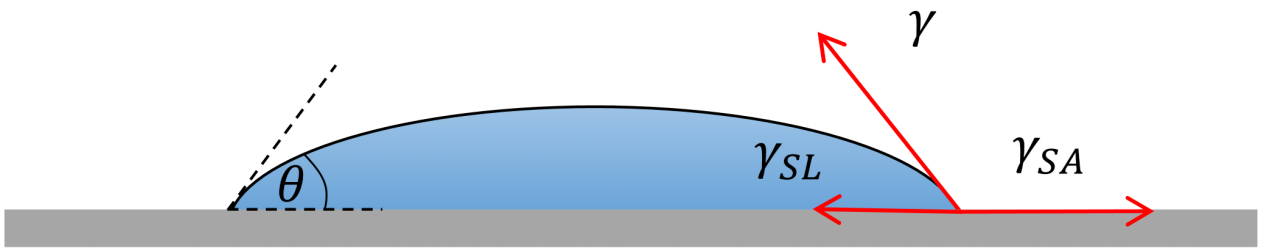

Figure 1.1: Drop on a flat surface. The static contact angle is represented by Θ and the interfacial forces by the red arrows.

equation [44]. Here, A_{rough} is the true surface area covered by a drop, while A_{flat} is the projected area. An increment in r means that A_{rough} increases, which leads to a higher surface energy. Hence, the surface energies (surface tension) γ_{SL} and γ_{SA} change by a factor r to $r\gamma_{SL}$ and $r\gamma_{SL}$, respectively. Assuming that the equilibrium remains even when the three-phase contact line moves an infinitesimal distance δx on the surface, then the variation of the surface energy will be zero (δE=0) when:

$$r(\gamma_{SA} - \gamma_{SL}) - \gamma_L \cos(\Theta_{app}) = 0, \tag{1.3}$$

where $\cos(\Theta_{app})$ is the apparent contact angle that we can see by eye or by optical microscopy. Using the definition of Young's contact angle into eqn. 3, we obtain the Wenzel equation:

$$\cos(\Theta_{app}) = r\cos(\Theta), \tag{1.4}$$

The roughness factor is equal or higher than 1 ($r \geq 1$). This means that for hydrophilic surfaces ($\Theta < 90°$), adding roughness will decrease the contact angle and the surface will be more hydrophilic. For hydrophobic surfaces ($\Theta > 90°$), Θ is in the range where $\cos(\Theta)$ is negative. Consequently, an increase in roughness implies that a hydrophobic surface becomes more hydrophobic.

1.3.4 Cassie state

When a homogeneous surface is formed by two components of different surface chemistry, the resulting contact angle of a drop will on the contact area fraction of each component an each respective intrinsic contact angles:

$$\cos(\Theta_{app}) = f_1 \cos(\Theta_1) + f_2 \cos(\Theta_2), \tag{1.5}$$

where Θ_1 and Θ_2 are the static contact angle for a smooth and homogeneous surfaces of components 1 and 2, respectively. f_1 and f_2 represent the area fraction of the components. To achieve superhydrophobicity, with contact angles above 150°, roughness and chemical heterogeneity must be added to the surface. In this case, air pockets can be entrapped between the structures, inducing the water-repellency (Fig. 1.2, left), which is called the Cassie-Baxter state [45]. Assuming the component 2 as air, then $\Theta_2 = 180°$. Since $f_1 + f_2 = 1$, eqn. 1.5 leads to:

$$\cos(\Theta_{app}) = f_1(1 + \cos(\Theta_1)) - 1, \tag{1.6}$$

One example of superhydrophobicity in nature would be the lotus leaf, which is a highly rough surface with structures in form of microprotrusions and nanohairs. A transition from Cassie-Baxter to Wenzel can be reached, for instance, with impacting drops that apply enough pressure to penetrate into the air gaps of a superhydrophobic surface (Fig. 1.2, right). Another way is by heating the surface, which allows the drop evaporation and subsequent condensation into the air gaps due to the increase of the water-air gaps pressure. This leads to the impalement of the liquid into the region of air pockets and the transition from Cassie-Baxter to Wenzel state takes place. [44].

1.3.5 Contact angle hysteresis

Surfaces in reality are not perfectly smooth and flat as considered in Young's equation. Heterogeneity due to chemical or structural differences in regions on

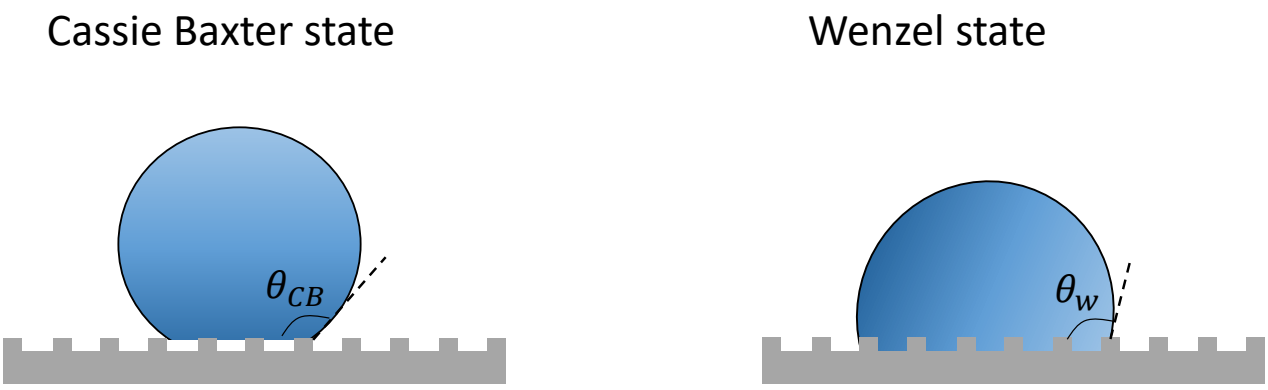

Figure 1.2: Left: Cassie-Baxter state of a drop deposited on a solid surface. The liquid contacts the solid only on top of protrusions, leaving air pockets in the other areas. The decrease in the effective contact area leads to an increase in contact angle. This state is characteristic of super water-repellent micro-structured surfaces. Right: Wenzel state of a drop deposited on a solid surface. the liquid penetrates into the grooves of the surface, increasing the effective contact area. This state is characteristic for hydrophilic or hydrophobic surfaces or even superhydrophobic surfaces, where the excess of pressure favours the penetration of liquid into the grooves of the surface.

the surface can cause that the contact angle θ can take any value between Θ_r and Θ_a. Here, Θ_r and Θ_a are the receding and advancing contact angles, respectively. The difference between these angles is the "Contact Angle Hysteresis", $\Delta\Theta = \Theta_a - \Theta_r$.

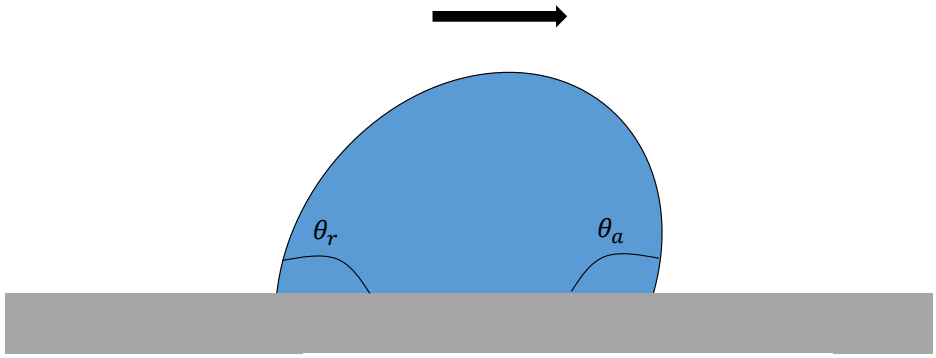

Figure 1.3: Drop moving laterally on a solid surface. The front angle is called the advancing contact angle Θ_a, while the angle in the rear side is the receding contact angle Θ_r.

Roughness [63, 64] or defects with different wettability than the surrounding surface can lead to the hysteresis [65]. The contact line can be pinned by these heterogeneities, which deforms the air-water interface and changes Θ_r or Θ_a

(Fig. 1.3).

Usually the hysteresis is measured by dispensing a drop from a syringe on a solid surface (Fig 1.4). The volume of the drop is increased until reaching a constant Θ_a. Afterwards, the liquid is withdrawn by the syringe and the contact angle decreases until a constant value is reached, the receding contact angle Θ_r.

It is important to distinguish between an static and dynamic receding or advancing contact angle. Basically, static refers the case when the hysteresis is measured changing the drop volume. Dynamic is the case of a single drop moving on a surface either for example, by sliding or bouncing. To measure dynamic contact angles is necessary to use high speed video imaging due to the fast motion of drops. Dynamic contact angles are directly related to the lateral friction force experienced by a drop moving on a solid surface, which will be further discussed in the next section.

Figure 1.4: Left: a syringe dispenses continuously liquid on a solid surface until the growing drop reaches a constant advancing contact angle Θ_a. Right: The syring withdraw liquid, which decreases the contact angle until a constant value called receding contact angle Θ_r.

1.3.6 Friction Force

When a drop moves on a surface, a friction force opposite to the direction of drop motion is experience at the contact line. This force is a result of the capillary force acting on the heterogeneities of the surface. As a consequence, friction force is dependent on the contact angle hysteresis.

To derive an expression for the friction force, it is necessary to consider a top

view of Fig. 1.3, where α represents the azimuthal angle between the drop radius $R(\alpha)$ (assuming a circular contact area) and the horizontal direction of the capillary force $\hat{\mathbf{x}}$ (Fig. 1.5). The friction force in this direction is therefore [66]:

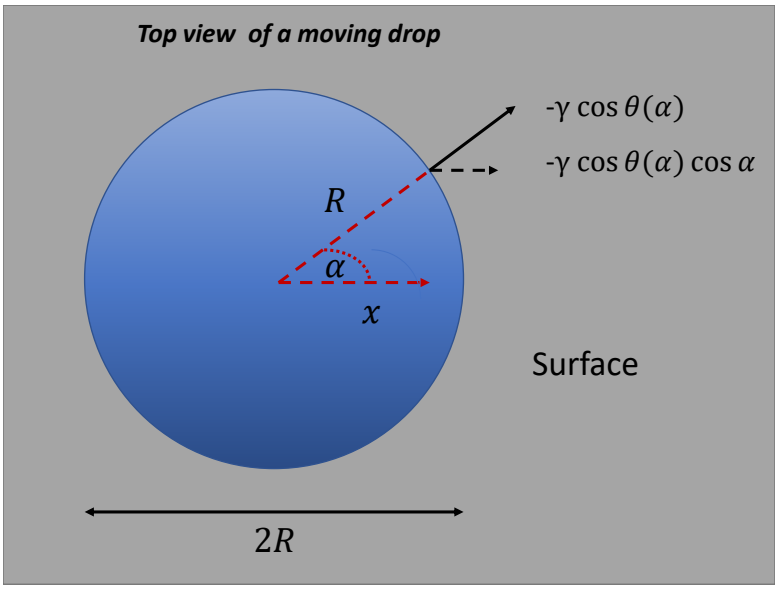

Figure 1.5: Top view of a drop moving laterally on a solid surface (from Fig. 1.3)

$$F_R = \int_0^{2\pi} \gamma \cos\Theta(\alpha) \cos\alpha \; R(\alpha) \; d\alpha \tag{1.7}$$

where $\hat{\mathbf{x}}$ is represented by $\cos\Theta(\alpha)\cos\alpha$. The drop radius is constant ($R(\alpha) = R$) due to the circular drop contact area. Considering a contact angle at the half rear equivalent to the receding contact angle ($\Theta(\alpha) = \Theta_R$, $\alpha = -\pi/2, \pi/2$), and a contact angle at the half front equivalent to the advancing contact angle ($\Theta(\alpha) = \Theta_R$, $\alpha = \pi/2, 3\pi/2$), the integral yields [67–69]:

$$\begin{aligned} F_R &= \int_{-\pi/2}^{\pi/2} \gamma \cos\Theta_R \cos\alpha \; R \; d\alpha \; + \int_{\pi/2}^{3\pi/2} \gamma \cos\Theta_A \cos\alpha \; R \; d\alpha \\ &= R\gamma \left(\cos\Theta_R \sin\alpha \Big|_{-\pi/2}^{\pi/2} + \cos\Theta_A \sin\alpha \Big|_{\pi/2}^{3\pi/2} \right) \\ &= 2R\gamma(\cos\Theta_R - \cos\Theta_A) \end{aligned} \tag{1.8}$$

The friction force will increase with size of the sliding drop. Moreover, the

contact angle hysteresis also influences the magnitude of the friction. Surfaces with low hysteresis like superhydrophobic surfaces ($\Delta\Theta < 10°$) exert a lower friction force compared to hydrophobic surfaces, which exhibit higher hysteresis.

When a a drop moves over a surface defect trying to overcome it, the deformation of the interface leads to a change in the hysteresis due to the pinning force. This means that the equilibrium contact angle must increase in the front part and decrease in the rear part. Thus, the friction force expressed in eqn 1.8 can be written in terms of the contribution in the advancing f_a and receding side f_r:

$$F_R = f_a + f_r = 2R\gamma(\cos\Theta_{eq} - \cos\Theta_A) + 2R\gamma(\cos\Theta_R - \cos\Theta_{eq}) \tag{1.9}$$

The previous equation is very useful to determine the energy dissipated by a drop due to the friction forces or in other words, the work done to overcome these forces of drops impacting on superhydrophobic surfaces [70]. In this thesis, I will calculate such dissipated energy by friction of impacting drops on hydrophobic surfaces resulting from an advancing and receding contact line prior rebound.

1.4 Drop impact outcomes

When a drop hits a surface, the possible outcome have been distinguished mainly as: Deposition, rebound and splashing [9, 71]. Deposition occurs for hydrophilic surfaces, where the drop after the impact spreads and wets the surface (Fig. 1.6a). When the surface is hydrophobic or superhydrophobic, a rebound takes place. Here, after the impact, while the drop is spreading on the surface, the kinetic energy is converted to surface energy until the drop reaches its maximum spreading diameter, i.e, the lateral length between the edge contact points with the surface (Fig. 1.6b). This stage is called the spreading phase. Afterwards, the drop starts to retract due to the surface tension forces, and now the surface energy is released in form of kinetic energy. If the kinetic energy is high enough to overcome the adhesion forces from the surface, the drop will

rebound. This means that a rebound is more probable as a solid surface has lower wettability, which decreases the adhesion forces. A higher wettability can lead to partial rebounds, with part of the drop remaining on the surface. Partial rebounds can also occur on microtextured superhydrophobic surfaces if the pressure of an impacting drop leads to a penetration of the liquid (impalement) into the surface structures, leading to a transition to a Cassie-Baxter to Wenzel transition once the magnitude of the impact speed is high enough [72].

As the impact speed increases on hydrophobic and superhydrophobic surfaces, the drop lamella spreads forming fingers, which then are ejected in form of secondary drops (Fig. 1.6c). These drops can be ejected either in the direction of the spreading or retraction movement depending on the wettability of the surface. The phenomenon is called splashing and depends on the viscosity, surface tension, impact speed and surface properties [9]. As the impact speed increases, more possibilities of splashing exists. In this thesis, I will focus on drops rebounding completely from hydrophobic and superhydrophobic surfaces without deposition or splashing.

1.5 Fundamental parameters of bouncing

1.5.1 Weber number

The drop impact is generally described by the so-called Weber number:

$$We = \frac{\rho v_0^2 R_0}{\gamma}, \tag{1.10}$$

, where ρ is the density of the liquid, v_0 the impact speed, γ the surface tension of the liquid, and R_0 the radius of the undeformed drop. This dimensionless parameter can be interpreted as the ratio between inertial to capillary forces. Assuming a spherical drop shape, the Weber number is directly related to the ratio between kinetic, E_k, and surface energy E_s:

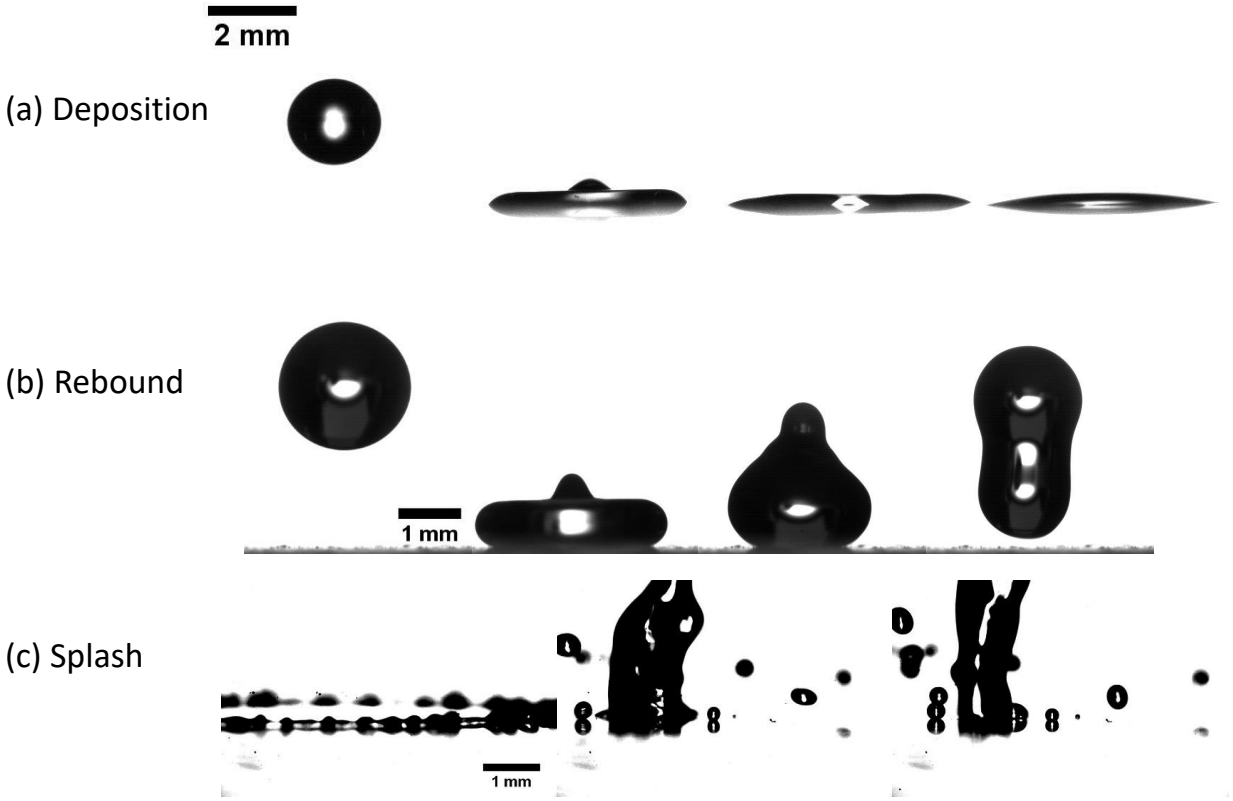

Figure 1.6: Different outcomes of drop impact: Deposition, rebound and splash.

$$\frac{E_k}{E_s} = \frac{\frac{1}{2}mv_0^2}{\pi R_0^2\gamma} = \frac{\frac{1}{2}\rho\frac{4}{3}\pi R_0^3 v_0^2}{\pi R_0^2\gamma} = \frac{2}{3}We \tag{1.11}$$

As higher is v_0, the kinetic energy and We increases. Accordingly, experiments of drops impacting at different v_0 and volumes are usually represented in terms of We as measure of their impact energy.

1.5.2 Reynolds number

The Reynolds number represents the ratio of inertial forces to viscous forces, and is defined as:

$$Re = \frac{\rho u L}{\mu}, \tag{1.12}$$

where v_0 is the speed of the drop (fluid), μ is the dynamic viscosity and L its characteristic length, which typically for a drop corresponds to its radius. The

Reynolds number is used to describe the type of flow pattern. For $Re < 1100$, a flow is laminar, with defined smooth laminar layers. When $Re > 2100$, the flow around is turbulent, i.e, the fluid layers disrupt each other, forming irregular changes in speed and therefore in pressure. Viscous effects become more important with increasing viscosity. In particular, viscous forces play an important role in drop impact dynamics when $Oh = \sqrt{We}/Re > 0.035$ [73]. Here, Oh is defined as the Ohnersorge number, which combines We Re to represent the ratio between inertial forces to viscous and surface tension forces.

1.5.3 Capillary length

The capillary length represents the ratio between gravitational and surface tension forces of a fluid. For a drop of radius a and height $2a$, the capillary length can be derived from the balance of the pressure acting on the drop due to gravity and surface tension. The pressure by gravity is :

$$P_g = 2\rho g a \tag{1.13}$$

The pressure due to surface tensions can be expressed as the Laplace pressure:

$$\Delta P = \gamma \frac{2}{a} \tag{1.14}$$

In the equilibrium of pressures, $P_g = \Delta P$. This yields:

$$a = \sqrt{\frac{\gamma}{\rho g}}, \tag{1.15}$$

which is the capillary lenght. For a water drop, $a = 2.7\ mm$. If $a > 2.7mm$, then the gravity dominates over surface tension.

During the impact, a drop can be flattened like a puddle or pancake ($We > 1$). Furthermore, at the moment of the impact, v_0 decreases to zero until the drop stops during the spreading phase. If the drop radius is R_0, the speed decreasing occurs at a characteristic time called the crashing time, $\tau^* \sim R_0/v_0$, which can be understood as the time taken by the drop to deform vertically

from 0 to R_0. This means that the acceleration experienced by the drop in this moment would be $a_c = v_0^2/R_0$. Now the Laplace pressure will be balanced by a pressure $P = 2\rho g R_0$. Thus, we can express the height/thickness of the flattened drop as $h = \sqrt{\gamma/\rho a_c}$.

1.5.4 Restitution coefficient

The restitution coefficient, e, is widely used to describe the energy loss of a rebounding drop during the impact. This parameter represents the change in the kinetic energy from the moment of the impact on a solid surface and the taking off:

$$e = \sqrt{\frac{\frac{1}{2}mv_1^2}{\frac{1}{2}mv_0^2}} = \frac{v_1}{v_0}, \tag{1.16}$$

where v_1 is the taking off speed of the drop. The change in the gravitational potential energy is negligible since the drop height remains relatively constant during the entire impact process. For large deformations induced by high impact speeds, the drop speed becomes difficult to measure. Therefore, a restitution coefficient based on the change in the gravitational potential energy from the falling height h_0 and the bouncing height h_1 is used:

$$e = \sqrt{\frac{mgh_1}{mgh_0}} = \sqrt{\frac{h_1}{h_0}}, \tag{1.17}$$

Superhydrophobic surfaces have shown values of e around 0.9, which means that only 10% of the initial kinetic energy is dissipated during the impact. For low Weber numbers ($We \leq 0.2$), the dissipation is limited by the friction of the surface, while for high Weber numbers ($We \geq 0.2$) the main dissipation source is the viscous dissipation.

1.5.5 Contact time

The contact time of a bouncing drop is defined as the duration of the impact process, from the moment when the drop impacts a surface until it bounces off the

surface. Typically, drops bouncing on superhydrophobic surfaces exhibit short contact times in the order of milliseconds. Due to the low adhesion of water on repellent surfaces, the contact time has been relevant in self-cleaning, anti-icing [74, 75] and heat transfer applications . Since contact time represents the duration of drop-surface interaction, it also conditions their exchange of mass, momentum and energy. For this reason, the design of new superhydrophobic surfaces to minimize the contact time has attracted a lot of interest. For example, the occurrence of pathogen transmission [76, 77] and freezing [78] can be decreased reducing the contact time. In general, microstructures added to the surface will reduce the surface-drop interaction and in some cases changing the drop impact dynamics. In this thesis, we will only focus on superhydrophobic and hydrophobic surfaces.

Richard et. al [79] showed that contact time of a drop impacting on a su-

Figure 1.7: Left: Falling drop hitting the surface before starting its deformation. Right: Deformation of the drop upon impact in form of a pancake. The lateral deformation is denoted by δx and the thickness of the film as h.

perhydrophobic surface is independent on the impact speed. This a result of a balance between inertia and capillary. The inertial forces are resulting from the drag force experienced by the drop, $F_D = \frac{1}{2} C_D \rho v_0^2 A \sim \rho v_0^2 R_0^2$, where A is the cross section area of the drop (πR_0^2), and C_D the drag coefficient. Capillary forces would be in the order of $\sim R_0 \gamma$. Assuming a lateral deformation δx (Fig. 1.7) much smaller than R_0, then $(R_0 + \delta x) \sim R_0$. As the contact time should scale with $\delta x / v_0$, it also scales with R_0 / v_0. In consequence, the balance

of both forces leads to following expression for contact time:

$$\tau = \sqrt{\frac{\rho R_0^3}{\gamma}} \tag{1.18}$$

Alternatively, we can write the energy conservation expression for a drop deformed by $\delta x >> R_0$:

$$E_k = E_s + Eg, \tag{1.19}$$

where, E_p is the gravitational potential energy. We can assume that capillarity dominates over gravity, then $E_p \sim 0$. Replacing by the terms of E_k and E_s already derived in eqn. 1.8 into eqn., we obtain:

$$\rho v_0^2 R_0^3 \sim \gamma \delta X^2, \tag{1.20}$$

Using again the relation $\tau \sim \delta x / v_0$ in eqn. 1.16, we obtain the same expression for the contact time as found in eqn. 1.18. According this equation, contact time is independent on the impact speed, but increases with increasing the drop size and decreasing surface tension, which has been experimentally proved.

1.5.6 Spreading parameter

During the spreading phase, a drop reach is deformed laterally and reaches maximum spreading radius, R_{max}, a half of the distance between the outer contact points with the surface. Logically, as the Weber number increases, R_{max} becomes larger. This relation is usually represented by the spreading parameter, β, which also serves to characterize the dissipation of energy of a drop. The spreading parameter is obtained from conservation of volume. The volume of a spherical falling drop is in the order of $V \sim R_0^3$, while the volume of the drop deformed laterally with thickness $h = \sqrt{\gamma / \rho a_c}$ is $V_p \sim R_{max}^2 h$, assuming a circular drop contact area. Accordingly:

$$R_0^3 = R_{max}^2 \sqrt{\gamma / \rho a_c} \tag{1.21}$$

Replacing $a_c = v_0^2/R_0$ in the previous equation, yields :

$$R_{max} \sim R_0 We^{1/4} \tag{1.22}$$

The relation in eqn. 1.5 has been experimentally demonstrated in several drop impact studies [80–82] for $We > 1$. However, this result is in contradiction with what is theoretically expected from a energy conservation approach. If we balance the kinetic energy with the surface energy, this yields a different result. The kinetic energy of the impacting drop is $\frac{1}{2}mv_0^2 = \rho V v_0^2 \sim \rho R_0^3 v_0^2$ and the surface energy is $\sim \gamma R_{max}^2$. This yields $R_{max} \sim R_0 We^{1/2}$. Such discrepancy in the scaling means that the energy is in fact not conserved during the impact. Also restitution coefficients of drops bouncing on superhydrophobic surfaces are not larger than 0.9, indicating an energy loss of at least 10%. The energy dissipation is due to internal viscous flow that will be enhanced as the Weber number increases [79].

1.6 Drop impact regimes

Depending on the viscosity of the fluid, drop impact will exhibit two different regimes, specifically in the retraction dynamics. These regimes are known as capillary-inertial and capillary-viscous regime. Both regimes were introduced by Bartolo [73]. He studied the retraction dynamics of low and high viscosity drops impacting hydrophobic surfaces.

Capillary-inertial regime The capillary-inertial regime is characteristic for drops of low viscosity like water. In this regime, impact dynamics is dominated by inertial and capillary forces. During the spreading phase, a rim-lamella structure is formed. Then, drops retract with a constant rim-height h and dynamic receding contact angle. The retraction is mainly due to capillary forces resulting from the surface tension. The capillary force F_C acting in a point mass located in the drop rim can be expressed as follows:

$$F_C = 2\pi\gamma R_{max}(1 - \cos\theta_R). \tag{1.23}$$

Here, F_C is a result of the surface tension at the contact line for the entire drop perimeter $2\pi R_{max}$. The retracting mass will move according the equation motion:

$$\frac{d}{dt}(m\frac{dR(t)}{dt}) = F_C, \tag{1.24}$$

where the stationary solution is

$$\frac{dm(t)}{dt} = 2\pi\rho R_0 v_{ret}. \tag{1.25}$$

Here V_{ret} is the retraction speed of the drop, which can be represented as $\frac{dR(t)}{dt}$. Therefore, replacing eqn. 1.25 into 1.24 leads to:

$$V_{ret} = \sqrt{\frac{\gamma(1 - \cos\theta_R)}{\rho h}} \tag{1.26}$$

Eqn. 1.26 shows that V_{ret} depends on θ_R and the thickness h of the lamella. According section 1.5.3, h decreases with increasing impact speed. In contrast, θ_R should decrease due to stronger capillary forces at the drop rim. As a result, V_{ret} should increase with increasing impact speed. Theoretical [83, 84] and experimental work [85] has confirmed that for water drops, the dynamics is within the inertial-capillary regime.

Capillary-viscous regime This regime is valid for viscous drops. The spreading and retraction dynamics is dominated by the competition between capillary and viscous forces. In fact, viscous drops spread and retract slower than drops with low viscosity [73, 86], so that R_{max} is smaller. Furthermore, drops retract with a decreasing θ_R over time due to the propagated capillary waves in the drop.

Bartolo derived an expression for F_C for the capillary-viscous regime as a function of the contact angle $\theta(t)$ in the onset of retraction [73]:

$$F_C = 2\pi R_{max}\gamma(\cos\theta(t) - \cos\theta_R) \tag{1.27}$$

In this thesis, I will focus mainly on spontaneous charging of impacting water drops. Liquids with other viscosities will be analyzed, but mostly as an example of other possibilities for charging.

1.7 Electrical double layer

The electrical double layer (EDL) forms when two conductive phases are in contact. One of the phases can be a fluid, particle, liquid droplet or bubbles, while the other a solid surface. Usually one of the phases is positively charged, while the other phase has the opposite charge, leading to an electrical equilibrium. This is because surface charges generate an electric field that attracts ions of opposite charge [87]. Therefore, two layers of opposite sign form near the solid-liquid interface.

1.7.1 Helmholtz model

The EDL theory has been developed through different approaches. A simple model developed by Helmholtz in 1853, considers that when a surface and a solution are in contact, two fixed layers of opposite sign are formed (Fig. 1.8, left). One layer is formed by the surface charges, which generate an electric field that attracts counterions in the fluid. The counterions layer and the surface charges layer compose the EDL like a capacitor plate configuration in parallel. From Gauss's Law, the flux ψ_A of a uniform electric field through two plates of area A is:

$$\psi_A = EA = \frac{Q}{\epsilon_0}, \tag{1.28}$$

where ϵ_0 is the vacuum permittivity. The capacitance is the capacity to store charge, given by $C_H = Q/V$, where V is the potential between the plates. Using the relation $E = V/d$, the capacitance of the Helmholtz double layer per unit

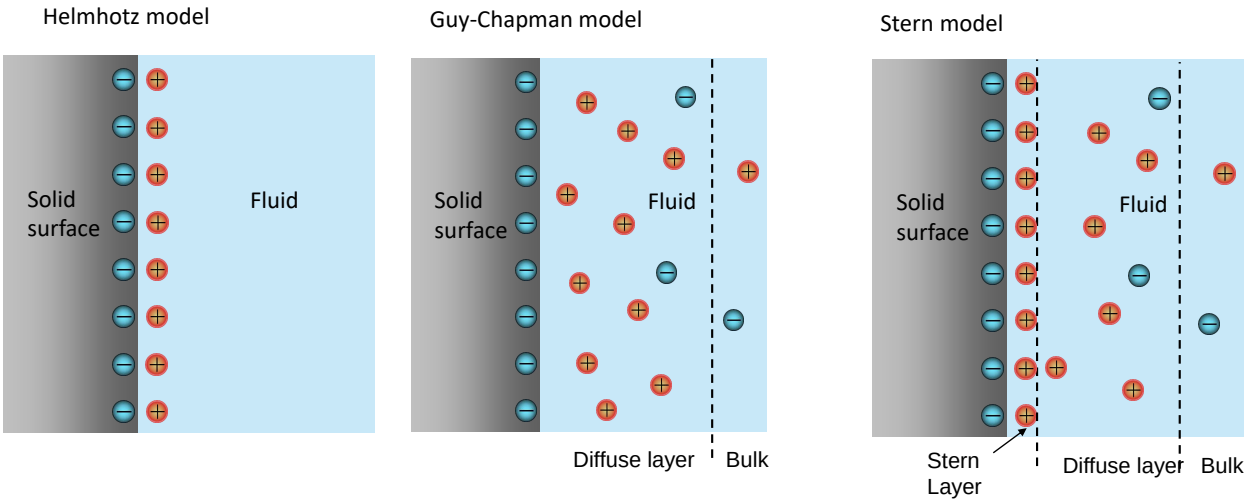

Figure 1.8: Models of the Electrical double layer

area is

$$C_H = \frac{\epsilon_r \epsilon_0}{d}, \tag{1.29}$$

Here, ϵ_0 is the permittivity of the free space, ϵ_r is relative permittivity of the substance between the plates, and d is the distance between the two layers, in the order of the ion radius, i.e., the nanometer scale. Such short distance means a high capacitance, which commonly gives the name of supercapacitor to the system of layers formed in the EDL.

The Helmholtz model can describe only simple aspects of the surface. However, considering a fixed layer in the solution seems unrealistic due to the thermal motion of molecules. More importantly, the Helmholtz model assumes a constant capacitance of the EDL, which experimentally is not true.

1.7.2 Guy-Chapman model

In the Guy-Chapman approach a fixed layer of ions at the surface and a diffuse layer of mobile ions in the solution is assumed (Fig. 1.8, center). This model considers in the fluid the thermal motion of ions, which can move far away from the surface forming the diffuse layer [87]. The main assumptions of the model include ion point charges (1), a constant dielectric permittivity of the solvent (2), flat surface in the molecular scale (4), and a distribution of ions as a result

of electrostatic interactions and statistical mechanics (5). Thus, the Boltzmann statistics allow us to describe the ion spatial distribution in the solution:

$$c_{\pm} = c_0 e^{\pm W/k_B T}, \tag{1.30}$$

where $c_{\pm}$ is the local ion concentration either cations (c_+) or anions (c_-) in the solution, c_0 is the equilibrium bulk density of ions, W is the work required to move an ion from infinite distance to a certain point point with potential Ψ such that ($W = \pm e\Psi$), k_B is the Boltzmann constant and T is the temperature. Here, we assumed a 1:1 salt concentration in the solution. The total charge density will be then:

$$\rho_0 = e(c_+ - c_-) = ec_0(e^{e\Psi/k_B T} - e^{-e\Psi/k_B T}), \tag{1.31}$$

with e as the elemental electron charge. The potential distribution of the solution is given by the Poisson equation:

$$\nabla^2\Psi(x, y, z) = \frac{\rho_0}{\epsilon\epsilon_0}. \tag{1.32}$$

Replacing eqn. 1.15 into 1.16, we obtain the Poisson-Boltzmann equation:

$$\nabla^2\Psi = \frac{ec_0}{\epsilon\epsilon_0}(e^{e\Psi/k_B T} - e^{-e\Psi/k_B T}). \tag{1.33}$$

The Poisson-Boltzmann equation can be solved for a simple model of a planar surface with a homogeneously distributed electric surface charge density. Here, the potential only changes with the distance x normal to the surface, since the contribution in y and z directions are zero by symmetry. Considering small potentials ($e|\Psi| << k_B T$) and expanding in series eqn 1.17 at its first term about zero, we obtain that $e^{e\Psi/k_B T}$ can be approximated to $1 - e\Psi/k_B T$:

$$\nabla^2\Psi(x, y, z) = \frac{ec_0}{\epsilon\epsilon_0}(1 + \frac{e\Psi}{k_B T} - 1 + \frac{e\Psi}{k_B T}) = \kappa^2\Psi, \tag{1.34}$$

with

$$\kappa = \sqrt{\frac{2e^2 c_0}{\epsilon\epsilon_0 k_B T}} \tag{1.35}$$

Eqn. 1.18 is the linear Poison-Boltzmann equation, where the reciprocal value of k is known as the Debye length: $\lambda_D = \kappa^{-1}$. It is important to mention that for ions of valence $Z_i > 1$ present in the solution, their charge concentration in the bulk will be $c_0 = \sum_n c_n Z_n$. The solution of the linear Poison-Boltzmann equation is in the form:

$$\Psi(x) = C_1 e^{\kappa x} + C_2 e^{-\kappa x} \tag{1.36}$$

The potential obeys to two boundary conditions: (1) the potential at the surface is the surface potential ($\Psi(x = 0) = \Psi_0$); (2) at infinite distance the potential is zero. Both conditions leads to $C_1 = 0$ and $C_2 = \Psi_0$. Thus, the potential as a function of the distance x to the surface is an exponential with decay lengthλ_D:

$$\Psi(x) = \Psi_0 e^{-x/\lambda_D} \tag{1.37}$$

λ_D characterizes the extent of the EDL containing the counterions that screen the surface charge. Consequently, increasing the salt concentration will lead to a more accumulation of ions close to the surface, leading to a more effective screening and a decrease of λ_D. In particular, a concentration of NaCl of 1 mM and 1 M have a Debye length of $\lambda_D = 9.6$ nm and $\lambda_D = 0.96$ nm, respectively.

Capacitance of the Diffuse Layer Grahame in 1947 derived an equation that relates the surface potential Ψ_0 with the the surface charge q [88]. This means that the equation also serves to calculate the capacitance of the diffuse layer in the Guy-Chapman model ($\frac{dq}{d\Psi_0}$). Assuming electroneutrality, i.e. the total amount of charge in the surface equals the charge in the EDL, $\int_0^\infty \rho_0 \, dx$:

$$q = \epsilon\epsilon_0 \int_0^\infty \frac{d^2\Psi}{dx^2} dx = \epsilon\epsilon_0 \left.\frac{\mathrm{d}\Psi}{\mathrm{d}x}\right|_{x=0} \tag{1.38}$$

Here, the boundary condition of zero potential at large distances from the surface was used. The eqn.(1.23) can be written as:

$$\frac{d^2\alpha}{dx^2} = \frac{c_0 e^2}{\epsilon\epsilon_0 k_B T}(e^{\alpha} - e^{-\alpha}) = \kappa^2 \sinh\alpha, \tag{1.39}$$

where α is the dimensionless potential $e\Psi_0/k_BT$. We can multiply by $\frac{d\alpha}{dx}$ both sides:

$$2\frac{d\alpha}{dx}\frac{d^2\alpha}{dx^2} = 2\frac{d\alpha}{dx}\kappa^2 \sinh\alpha, \tag{1.40}$$

by integrating both sides, we obtain:

$$(\frac{d\alpha}{dx})^2 = 2\kappa^2 \cosh\alpha + C_1 = 2\kappa^2(\cosh\alpha - 1) \tag{1.41}$$

Here, $C_1 = -2\kappa$ since at large distances, the potential and its derivative are zero. This yields:

$$\frac{d\alpha}{dx} = \kappa\sqrt{2(\cosh\ -1)} = -2\kappa \sinh\Big(\frac{\alpha}{2}\Big) \tag{1.42}$$

Note that $\frac{d\alpha}{dx} = \frac{e}{k_BT}\frac{d\Psi_0}{dx}$. Balancing with eqn 1.32 yields:

$$\frac{d\Psi_0}{dx} = -2\kappa\frac{k_BT}{e}\sinh\frac{\alpha}{2} \tag{1.43}$$

Replacing eqn.(1.33) into 1.28, we obtain the Grahame equation to calculate the surface charge:

$$q = \sqrt{8e^2 c_0 \epsilon\epsilon_0 k_B T}\sinh\frac{e\Psi_0}{2k_BT} \tag{1.44}$$

Finally, the capacitance can be calculated as follows:

$$C_G = \frac{dq}{d\Psi_0} = \epsilon\epsilon_0 \cosh\frac{e\Psi_0}{2k_BT} \tag{1.45}$$

The Guy Chapmann theory is limited by some of its assumptions. For example, a continuous dielectric permitivity of the solvent is not a realistic approach, since higher concentrations of the solvent close to the surface would lead to a

pronounced change in the permitivity. Secondly, the ions are considered as point charges, which actually is in good agreement for concentrations below 0.2 M between 50-80 mV. Of course, this only considers monovalent salts, and the model fails for higher concentrations with di/trivalent ions.

1.7.3 Stern model

Alternatively, Stern added one more layer to the Guy-Chapman model, combining it with the Helmholtz model. The Stern model considers an EDL formed by three layers. One layer of ions is fixed at the surface. The other two layers are a result of the reorganization of ions of opposite charge, called counterions, in the fluid [87]. These layers are called the Stern layer and the diffuse or Guy-Chapman layer (Fig 1.8, right). The Stern layer is formed by counterions bounded to the surface due to electrostatic forces, while the diffuse layer is composed by free movable ions that suffers the effect of electrostatic interaction and thermal agitation. All the ions are assumed with a finite size (1 nm radius), while in the diffuse layer are considered as point charges. Furthermore, the total charge at the interface is zero, with the net charge at the solid phase, Q_S, equivalent to the charge in the solution, Q_l. The charge in the solution is equal to the charge attached to the solid surface and in the diffuse layer $Q_S = Q_d + Q_s$.

The Stern model can be understood by two capacitors put in series. One capacitor is formed by the called Helmholtz region, i.e., the surface charge and the Stern layer. The second capacitor is the Guy-Chapman region, that is, the diffuse layer. Therefore, the total capacitance of the EDL, C_{EDL}, is given by

$$\frac{1}{C_{EDL}} = \frac{1}{C_H} + \frac{1}{C_G}, \tag{1.46}$$

where C_H and C_G are the capacitance of the Helmholtz and Guy-Chapman region, respectively. For saturated solutions, the total capacitance is approximately C_G since the double layer is mainly diffuse (Guy-Chapman model). On the other hand, for low concentrations of salts (dilute solutions), the EDL is formed mostly by fixed ions to the surface. Accordingly, the total capacitance

is approximately C_H.

1.8 Slide electrification model

Charge separation of drops sliding on a titled hydrophobic surface has been extensively studied for more than 20 years. In general, drops sliding on hydrophobic surfaces acquire a positive charge and leave the surface negatively charged. In the beginning, the phenomenon was described mainly qualitatively and attributed to the formation of an EDL at the solid-liquid interface. It is known that water ions can be present in form of OH^-, H_3O^+ and H^+. In addition, hydrophobic surfaces like fluoropolymers tend to absorb negative ions from water (e.g sliding drops), most likely, hydroxyl ions, OH^- [50, 51, 89]. The movement of the three phase contact line could break the electrical equilibrium of the EDL. Hence, as the drop slides, the electrical neutrality is broken and the drop accumulates the remaining positive ions. A quantitative theory of the process was just recently developed by Stetten et. al. : The slide electrification model [57].

The slide electrification model assumes that a fraction α of the surface charge density, σ_L, of the EDL is deposited on the surface as the drop slides:

$$\sigma_S = \alpha\sigma_L \tag{1.47}$$

Here, α is called the transfer coefficient. As the slide length increases, the drop will gradually become more positively charged. All the ions deposited on the surface are considered as OH^-, so the surface charge density has negative sign. If the drop is considered as a capacitor, then its charge, Q, will be given by $Q = C_d\Psi_d$, where C_d is the constant drop capacitance and Ψ_d the drop potential. Assuming that Ψ_d determines the limit of the accumulated charge in the drop, then the transfer coefficient can be written into a series of expansion at its first term:

$$\alpha(\Psi_d) = \alpha_0 + \alpha_1 \frac{q\Psi_d}{k_B T} = \alpha_0 + \alpha_1 \frac{qQ}{C_d k_B T} \tag{1.48}$$

where α_0 is the transfer coefficient at zero potential, q is the surface charge, k_B the Boltzmann constant and T is the temperature. Note that the potential energy $q\Psi_d$ is scaled by the thermal energy to simply obtain a dimensionless transfer coefficient. Thus, the surface charge density can be written as follows:

$$\sigma_S = (\alpha_0 + \alpha_1 \frac{qQ}{C_d k_B T})\sigma_L \tag{1.49}$$

When a drop slides an infinitesimal distance dx (Fig. 1.4) on the surface, the change in area will be wdx, with w as the width of the drop. The infinitesimal charge deposited on the surface is

$$dQ = -\alpha w \sigma_L dx \tag{1.50}$$

Combining eq. 1.15 and 1.16 leads to a differential equation for the drop charge of a single sliding drop:

$$dQ = -(\alpha_0 + \alpha_1 \frac{qQ}{C_d k_B T}) w \sigma_L dx = \frac{dQ}{dx} + \frac{Q}{\lambda_r} = -\alpha_0 w \sigma_L, \tag{1.51}$$

where

$$\lambda_r = \frac{C_d k_B T}{\alpha_1 w \sigma_L}. \tag{1.52}$$

Our starting boundary condition will be the moment when the drop does not yet slide, at L = 0. This implies that $Q(L = 0) = 0$ and the following solution for eqn. 1.18:

$$Q(L) = -\sigma_0 \lambda_r w (1 - e^{L/\lambda_r}) \tag{1.53}$$

with $\sigma_0 = \alpha_0 \sigma_L$, and L as the sliding distance. Note that σ_0 is the surface charge density at the first expansion series of α, where q has negative sign. Besides, λ_r represents the extent of the EDL or Debye layer. If an EDL is formed at the liquid-solid interface, the fixed layer of negative ions in the surface will be screened by counterion ions up to a distance λ_r that includes the Stern and

diffuse layer. From eqn 1.21, it is possible to get an expression for the surface charge density $\sigma_s = \alpha\sigma_L$ with an exponential decay length λ_r:

$$\sigma_s(x) = \frac{1}{w}\frac{dQ}{dx} = \alpha_0\sigma_L e^{-x/\lambda_r} \tag{1.54}$$

Here, σ_s varies according a distance along a sliding distance L. The slide electrification model assumes an homogeneous distribution of the charge in the area covered by the drop on the surface. As the model involves the disruption of an EDL by a moving contact line, it could be extended for other similar cases. In this thesis, an adapted model will be derived for charging of single bouncing drops.

Chapter 2

Experimental Methods

In this chapter, I will describe the experimental setup for drop charge detection that I designed and implemented during my PhD. All the results obtained by this setup will be presented in the following chapters.

The presented method arises as an convenient alternative to the typical setups for drop charge detection, since it is based on very fundamental physics. In the later sections and chapters, it will be referred to the "Electric Field Method". This method is inspired by the Millikan's oil drop experiment to measure the electron charge [90]. It has also similarities with the Miljkovic's method to measure the charge of jumping droplets using electric fields [48], as mentioned in the previous section. Basically these setups are based on the idea that an object with a net charge will be moved in the presence of an electric field. Combining such electric field with high-speed video imaging, can be a powerful tool to correlate charge separation and drop impact dynamics. In chapter 3 and 4, I will apply the Electric field method to measure the charge of drops rebounding from superhydrophobic and hydrophobic surfaces, respectively.

2.1 The Electric Field Method

The method is based on applying of electric fields deflect bouncing drops on surfaces with different hydrophobic coatings. Among the advantages are the simplicity of the setup without the need of using high gain current / voltage

amplifiers, that are prone to pick up electrical noise from the surrounding

2.1.1 Experimental setup

Two copper plates of $50 \times 16 \times 4$ mm^3 with a gap of 18 mm were placed vertically inside of groves of 1 mm of a Teflon plate of 40×50 mm^2, which acted as an insulator (Fig. 2.1). The Teflon plate was assembled to a aluminum plate movable in the x-y direction to change the position of the sample. The copper plates were connected to a high voltage DC power supply (Analogic, AN-3200, 25 kV maximum voltage) to generate an homogeneous electric field between the electrodes. For the experiments, the electric field was calculated by $E = V/d$, where V is the applied voltage and d the separation between the copper plates. Drops were released from a grounded motorized syringe pump. The grounding was used to avoid initial charging of drops before the impact. This means that only neutral water drops were dispensed for the experiments. Calibration measurements described in Appendix 1, verified the electrical neutrality of drops. An aluminum tube of 20 mm height, 15 mm outside diameter and 2mm inner diameter, was used to shield the drop and needle to avoid polarization effects on drops before falling. This aluminum tube prevents that drops would get polarized by possible field gradients in the region close to the edges of the copper plates, where the electric field may be not homogeneous close to the edges.

2.1.1.1 High speed-video imaging and tracking of drop mass centre

Drop impact videos were recorded using a high-speed camera (Photron Fast-Cam Mini UX100) at 5000 fps, which was placed adjacent to the copper plates. Two types of objective lenses were used: (1) Mitutoyo 2x; and (2) Computar MLH-10x Macro. The high-speed videos were analyzed by a MATLAB® algorithm. Assuming that the projected drop centroid coincides with its center of mass (Fig. 2.2a, red dot), the algorithm allows us to track the position of the drop mass centre (x_{cm},y_{cm}) at each frame of the videos (Fig. 2.2a, red dot and Fig. 2.2b). Other positions at the drop surface can be tracked as well, e.g. the

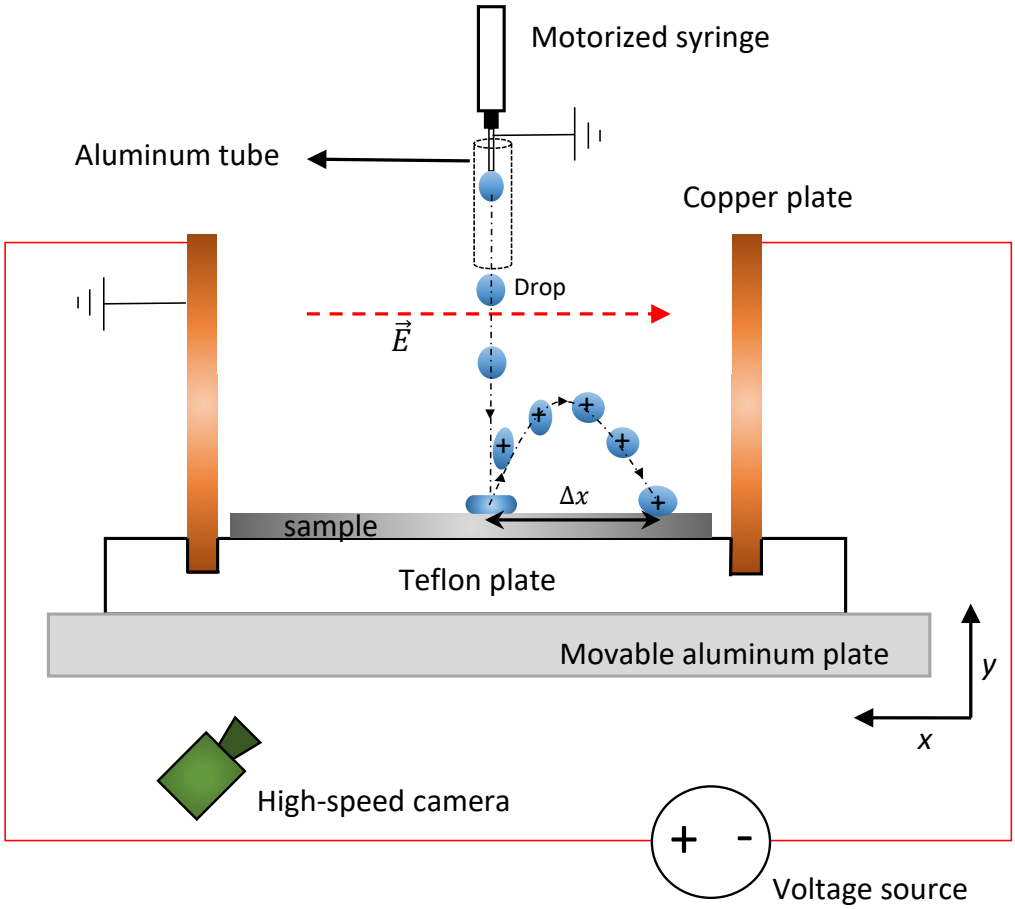

Figure 2.1: Experimental setup of the electric field method for drop charge detection. The high speed camera is placed adjacent to the copper plates (side view).

bottom position. In addition, assuming a spheroidal shape for a falling drop, the volume of drops was calculated as $V = \frac{1}{6}\pi D_0^3, with R_0 = \sqrt[3]{D_x^2 D_y}$, with D_x and D_y as the lateral and vertical diameter respectively.

2.1.2 Basic Principle

The electric field method assumes that drops will charge after rebounding from a super/hydrophobic surface as reported previously by Sun [25]. Consequently, bouncing drops should be deflected by an electric field. Tracking the motion of the drop mass centre allows us to calculate the drop charge.

The magnitude of an homogeneous electric field will be the same at each point between the copper plates. Therefore, if the drop is charged, it will be

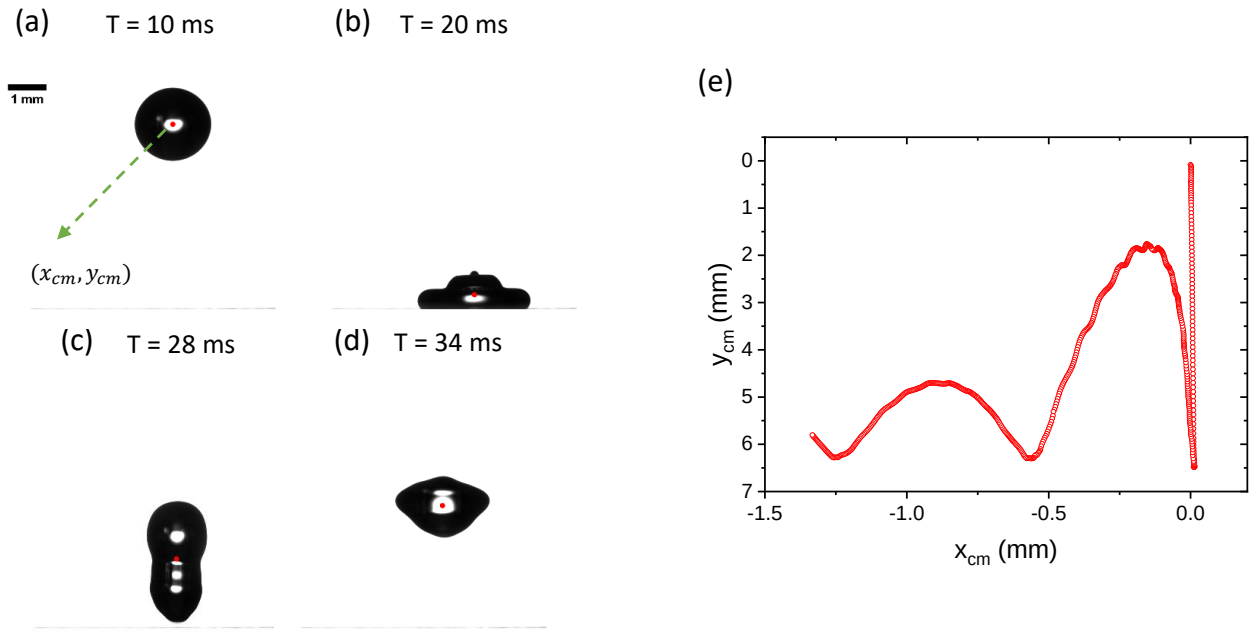

Figure 2.2: (a) Tracking of the drop mass center (red dot) for a 4 μL droplet rebounding from a superhydrophobic surface. The surface is tilted 1°. (b) Position of the drop mass center in the y-axis as a function of time.

deflected laterally by a constant electrostatic force:

$$F_E = QE = ma_x, \tag{2.1}$$

which leads to:

$$a_x = \frac{QE}{m}. \tag{2.2}$$

Here, Q is the drop charge, m the drop mass and a_x is the lateral acceleration due to the electrostatic force. Q is considered as a point charge located in the drop mass centre.

From the drop impact videos, one can determine the lateral displacement of the drop mass center, Δx, during the entire impact process from the moment of bouncing off until the drop is in contact again with the surface. As drops move laterally with a constant acceleration, the displacement in the x-direction is:

$$\Delta x = v_{ox}t + \frac{1}{2}a_x t^2 \sim \frac{1}{2}a_x t^2, \tag{2.3}$$

with t time taken by the drop to cover a lateral distance Δx after rebound, and $v_0 x$ the initial lateral speed for that motion. We considered $v_{0x} \sim 0$, which will be shown in Results section in chapter 3. Replacing eqn. 2.1 into 2.2, an expression for Q is obtained:

$$Q = \frac{2\rho V \Delta x}{E t^2}. \tag{2.4}$$

It is important to mention that the electric field method considers that no induced electrostatic effects take place on the drop, only the charge separation at the solid-liquid interface during the impact. In chapter 3, an example of a deflected drop will be shown with the corresponding proof of the independence of drop charge with the magnitude of the electric field.

2.1.3 Calibration of drop charge measurements

In general, drop charge measurements should be compared in magnitude with calibration experiments to test their precision and reliability. The obvious calibration method would be the Faraday cup method. This method serves to measure the charge of particles [91] or drops [92] collected with a metal cup connected to an electrometer, which detects a current signal. Integrating the current signal gives amount of charge. However, in this thesis I report drop impact on flat surfaces, which complicates the collection of drops. Alternatively, I implemented a similar experiment, changing the way of catching drops.

Instead of a Faraday cup, I used a wire probe made of Tungsten (0.025 mm diameter, Asfa Ascar, Germany). The probe was placed close to surface in such a way that, when a drop rebounds, it touches the probe and then discharges (Fig. 2.3a). In addition, the drop touches the probe already during the free fall, which in addition allows verifying its electrical neutrality. A current signal was measured (Fig. 2.3b,c) with a current amplifier (DDPCA-300 and

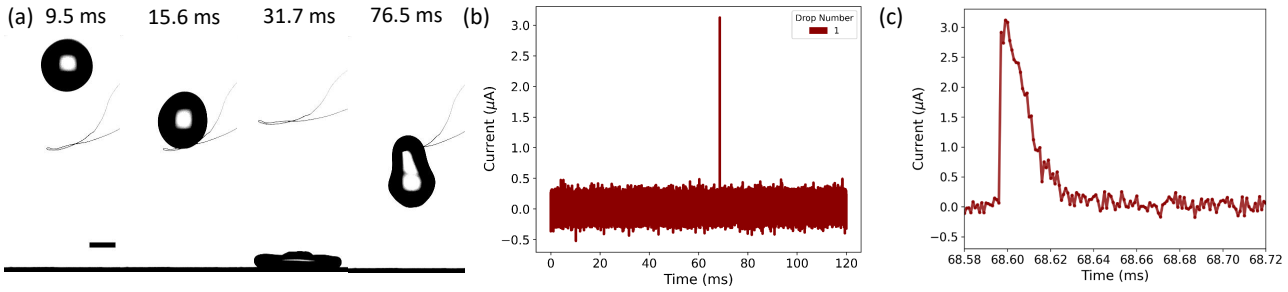

Figure 2.3: Calibration setup to measure the charge of bouncing drops. (a) High-speed images of a 4 μ L drop rebounding from a superhydrophobic surface with a fluoropolymer coating (silicone nanofilaments). From left to right, the process is as follows: A drop falls towards the surface (9.5 ms). During free fall the drop touches the wire (15.6ms) and then it hits the surface (31.7 ms). Afterwards it rebounds and touches the wire again (76.5 ms). (b) Current signal detected by the current amplifier. (c) Zoom-in of the region where the current peak in (a) was detected. Scale bar represents 1 mm.

DLPCA-200, FEMTO Messtechnik GmbH, Germany) connected to the ground. Simultaneously, the impact process was recorded by high-speed video imaging to verify a complete discharging of the drops. The high speed camera was operated under the same conditions mentioned in section 2.1.1.

From Fig. 2.3(b), one can note that neutral drops are generated from a grounded needle, since no peaks are detected before a time lapse of 68.6 ms, when the drop touches the wire. Furthermore, drops touch the wire for $\sim$ 30 ms, while the discharging time occurs in $\sim$ 1ms. This means that drops can be discharged completely after rebound by the wire probe. Using the calibration setup, the charge measurement of 17 μL and 4 μL drops released from 3cm height reveals that values of charge are in the order of picocoulomb. In particular, 17 μL drops exhibited a charge of 50 ± 3 pC (3 measurements), whereas a 4μL drop a charge of 26 pC (1 measurement). This suggests that increasing the drop volume will lead to a higher charge. In the next chapter, I will show the agreement between the calibration measurements and the electric field method to determine the drop charge.

Chapter 3

Drop charging on superhydrophobic surfaces

In this chapter, I will present and discuss the results regarding the charging of drops rebounding from superhydrophobic surfaces, which were obtained by the Electric field method. The results presented in this chapter are mainly obtained using water drops unless stated otherwise.

Surfaces based on silicon nanofilaments and candle soot template surfaces were used. These surfaces were selected due to their high hydrophobicity, which allows water drops rebound fully off of them at a wide range of impact speeds. Furthermore, their surface chemistry is similar to hydrophobic surfaces used in slide electrification experiments. Candle soot template surface have been used by others for the creation of surface charge gradients by drop impact [25].

The charging of bouncing drops has never been systematically quantified and studied from a fundamental viewpoint. As the bouncing process involves a moving contact line during the spreading and receding phase, the charge separation may be similar to the slide electrification. Although it has been suggested that charge separation by drop impact may depend on parameters such as Weber number [25] and contact area [36], there is still uncertainty about which parameter controls the process. Here, parameters like the impact speed, the speed of the retracting contact line, contact area among others will be explored. I additionally proposed a quantitative model to explain the charge separation of bouncing drops

3.1 Materials and sample preparation

Superhydrophobic surfaces were prepared by using glass microscope slides ($26 \times 76\ mm^2$, 1 mm thick) as substrates. First, the slides were sinicated in toluene, ethanol and acetone for 5 minutes each one. Second, plasma activation was applied to the glass slides (details below). Afterwards, five different types of superhydrophobic surfaces were prepared. The first type of surface was the candle soot-templated fluorinated superhydrophobic surfaces. The other four types were based on silicone nanofilaments (SN): pure SN, fluorinated SN with perfluorodecyltrichlorosilane (SN-FDTS), octadecyltrichlorosilane (OTS) modified SN (SN-OTS) and polydimethylsiloxane (PDMS) brush-coated SN (SN-PDMS brush).

3.1.1 Silicone Nanofilaments

Silicone nanofilaments were prepared modifying the method of Zhang and Seeger [93]. After the sonication, the glass slides were dried at 60°C for 1 hour. Then, oxygen plasma activation was applied to the slides at 40 W power for 2 min (Diener Electronic Plasma Surface Technology: Femto BLS, Ebhausen, Germany). Finally, the glass slides were immersed in 100 mL toluene containing trichloromethylsilane (TCMS, 33.85 mM) for 3 hours.

3.1.2 Fluorination of samples

The first step for fluorination is plasma treatment on the SN samples (100 W, 5 min). Afterwards, the samples were immersed in a solution of 100 mL of n-hexane with perfluorodecyltrichlorosilane (FDTS) (2.92 mM) for 1 hour. After finishing the fluorination, the samples were rinsed with hexane and dried by evaporation of the hexane in air.

3.2 OTS modification

Oxygen plasma treatment was performed on the nanofilament samples (100 W, 5 min). Then, the surfaces were rinsed in a solution of 40 μL of trichloro(octadecyl)silane in toluene (1.01 mM). The samples were rinsed with hexane after 6 hours .

3.2.1 PDMS Brushes

The preparation of PDMS Brushes is based on the method of Liu et al. [94]. Dichlorodimethylsilane (DCDMS, Sigma Aldrich) was dissolved in 40 mL of toluene. The toluene was saturated with water (0.024 mM). The molar ratios were controlled to be 10 : 1 for DCDMS to water. The final step was to immerse the oxygen plasma treated (100 W, 5 min) nanofilament surfaces in the solution for 30 minutes to obtain PDMS brush coated surfaces. Afterwards, the surfaces are removed to be dried due to the evaporation of the solution in air.

3.2.2 Candle soot template surfaces

The preparation of the surfaces is based on the method described by Deng et al. [12]. Glass slides were moved above a candle flame until they were covered by a black layer of soot. The soot-coated surfaces were put then in a desiccator with two beakers, containing 3 mL of tetraethoxysilane (TES) and 3 mL of ammonia. A silica shell ($\sim$ 20 nm) by chemical vapor deposition (CVD) of TES catalyzed by ammonia within 24 hours is formed around the soot and on the substrates. The substrates were heated at 550°C for 5 hours to remove the soot templates, leaving behind the silica shells. Finally, the substrates were coated with a monolayer of trichloroperflouroctylsilane by CVD for 1 hour in a desiccator. This step provides to the surfaces superhydrophobicity.

3.3 Drop impact experiments

Five sets of experiments were performed using the Electric field method. This means that all the experiments quantify the charge of drops bouncing on super-

hydrophobic surfaces while an uniform electric field of $E = 55\ kV/m$ is applied. The experiments are numbered as follows:

- 4 μL water drops were released from 0.5-3 cm height ($We = 1, ..., 26$) on different superhydrophobic surfaces.
- Water drops of different volumes (3-13 μL) were released on SN-FDTS from 3 cm height.
- 4 μL water drops with different types of salts at different concentrations were released from 3 cm height on SN-FDTS.
- 6 μL drops released onto SN-PDMS brush and candle soot surfaces from 1.5 cm height
- Different types of liquids were released on candle soot templated surfaces

The four first experiments play an important role in the determination of the main parameter responsible of drop charging and the derivation of a theoretical model for bouncing drops. The last experiment is relevant to understand at what extent properties such as viscosity and surface tension can affect the charge separation process.

3.4 Observation of deflection of drops by the Electric field method

Water drops impacting on different superhydrophobic surfaces rebound vertically in the absence of an electric field (Fig. 3.1a). If an electric field parallel to the surface is generated (electric field method), drops deflect laterally as expected. The deflection occurs in the direction of the electric field (Fig. 3.1b,c). This demonstrates that drops charge positively upon rebound. The vertical trajectory of falling drops before the impact shows no deflection and thus neutral net charge after detachment from the needle.

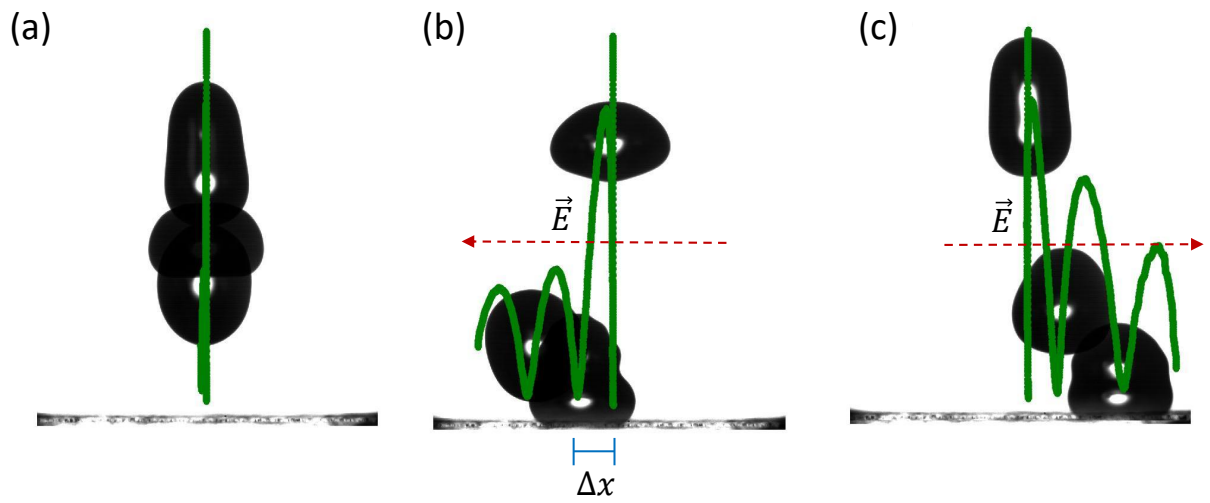

Figure 3.1: Drop rebounding from SN-FDTS surface with : (a) no applied electric field, (b) Electric field applied from right to left, and (c) from left to right. Green dots represent the trajectory of the drop mass center. Δx is the distance between the first and second impact with the surface.

For the experiments with $We < 13$, drops can exhibit complete rebounds with conservation of volume. However, for $We > 13$, drop break up takes place and the volume does not remain constant. In this range, the drop ejects a jet from the top of its surface (Fig. 3.2a). With increasing impact energy further, the break up can lead to the ejection of more drops smaller than the jet ejected from the top of the drop (Fig. 3.2b). These smaller drops were also laterally deflected in the direction of the electric field. Therefore, ejected drops carry out a positive charge. Considering the amount of volume ejected (0.02-0.3 μL), the charge of the ejected drops would be negligible compared to charge of the primary drop. This is due to the assumption that charge is correlated to the drop volume, so that as larger the drop, the charge should increase. The results of drop charge for the break up regime and the influence of drop volume will be shown in the next section.

For the calculation of charge for the primary deflected drop in the drop break up regime, it is necessary to know the volume of the ejected drops. This volume was calculated assuming an spheroidal drop shape for Weber numbers where the loss in volume is small compared to the original 4 μL volume. The strong

deformation of the primary drop makes difficult to calculate directly the drop volume in the break up regime. Volumes were no below 3.7 μL, which is actually a good approximation of the charge for the initial drop volume.

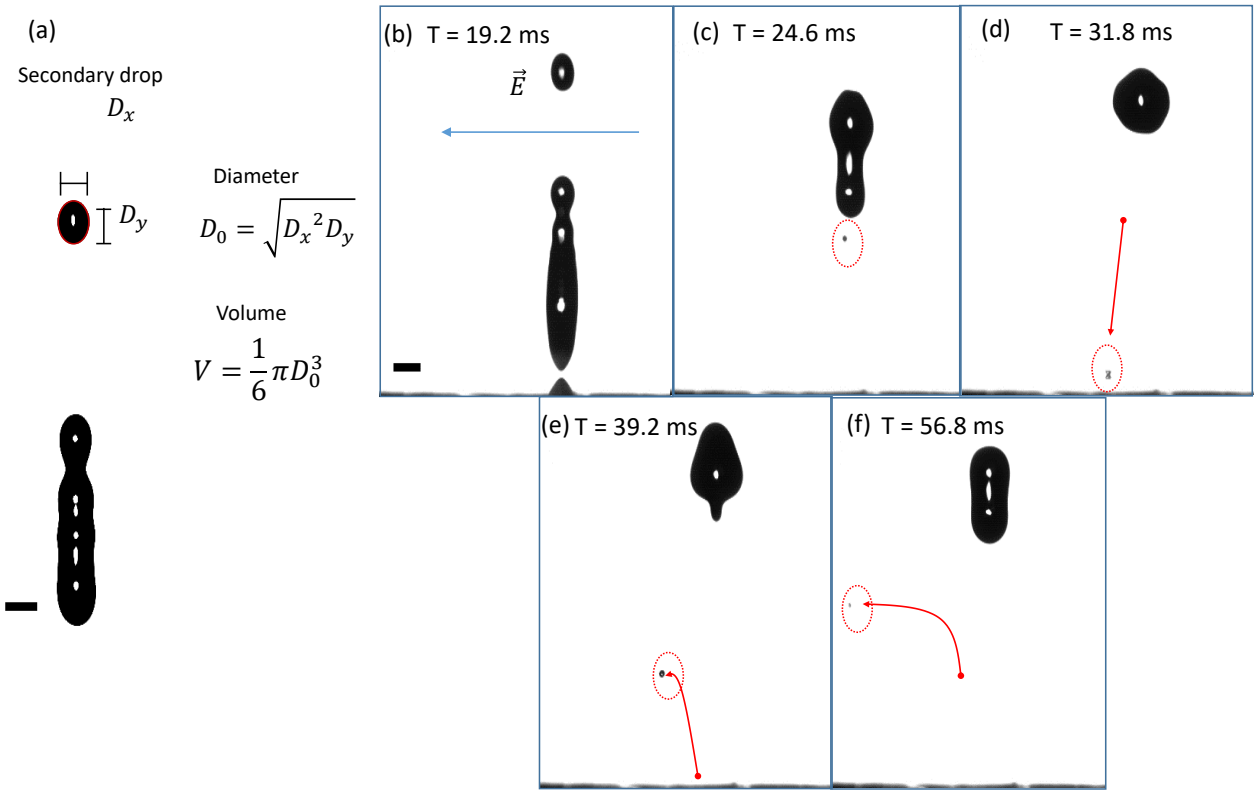

Figure 3.2: (a) Example of the volume calculation for an ejected drop. (b-f) Time sequence of a drop impacting on SN-FDTS at $We = 13$. The circle dotted line encloses a secondary drop ejected from the bottom of the drop. The red arrows represents the motion of the ejected drop. The begin of the arrow is represented by a red dot, which indicates a previous position of the drop.

3.5 Homogeneity of the electric field

Before the drop charge calculations, it is instructive to verify the homogeneity of the electric field. If the magnitude of the electric field is the same at any point between the plates, then the charge distribution in the drop would not influence our calculations. In other words, a point charge located at the center of the drop will experience the same total force than the one resulting for any different charge distribution within the drop in the presence of a homogeneous

electric field. The software Comsol Multiphysics 5.5 was used to calculate the

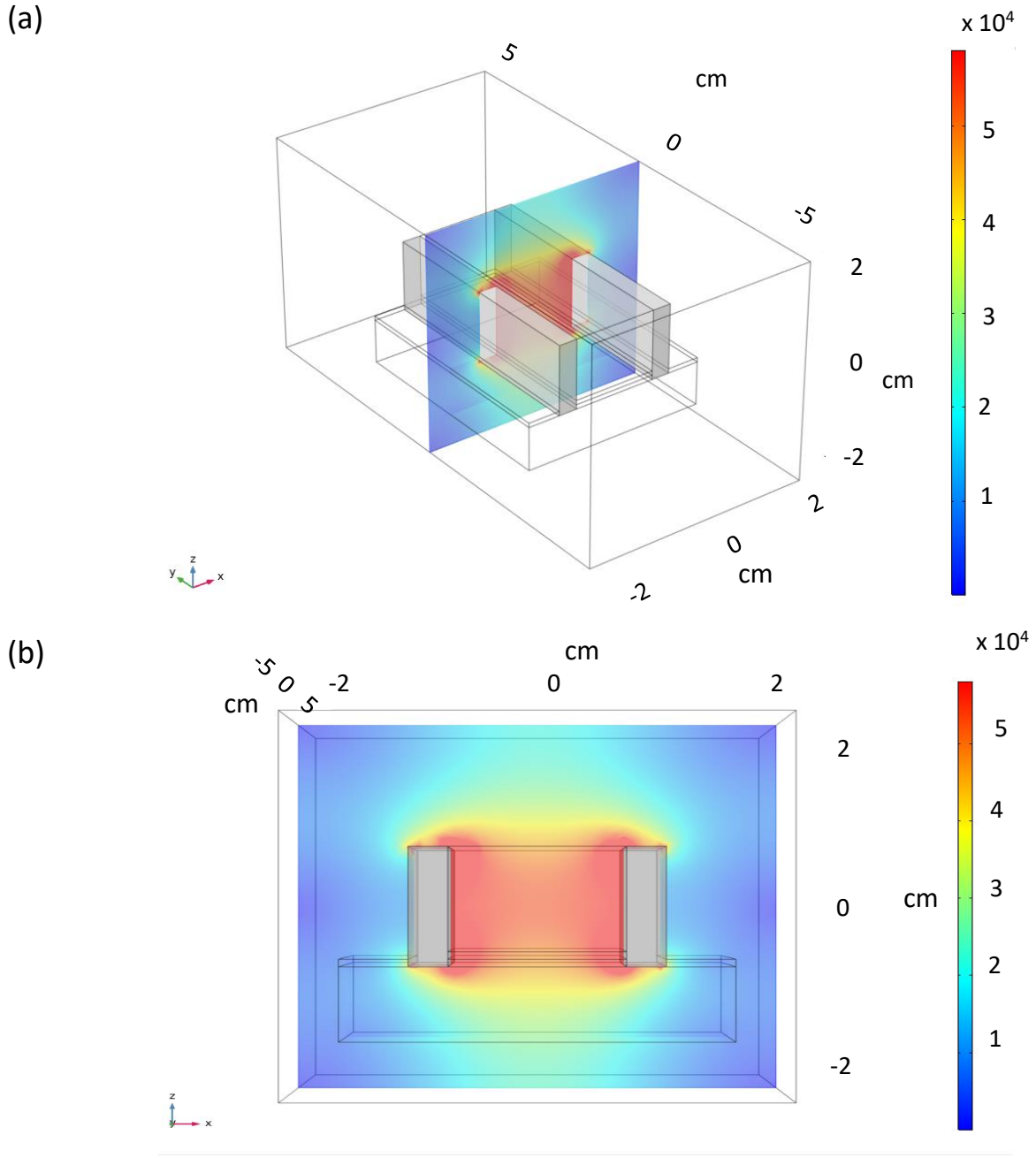

Figure 3.3: (a) Configuration for the simulation with the two metal electrodes, the Teflon block and a glass slide of 1 mm thickness. The colored plane indicates the distribution of the electric field in the xz-plane (b) xz-plane view from (a).

3-D field distribution for the Electric field method. The same conditions of the experiments were set up, i.e., two metal electrodes separated by 18 mm, one Teflon block below and as a sample, one glass slide of 1 mm thickness on

top of the Teflon block. Furthermore, a voltage of 1 kV was applied to one of the electrodes, while the other was grounded (Fig. 3.3). The simulation was done as full 3 D simulations. From the 3D data set obtained, the corresponding cross-sections were extracted and plotted.

Ideally, according to the distance and voltage that I have used, the electric field should be 55 kV/m in all directions. From a realistic viewpoint, the electric field cannot be homogeneous in the whole region between the plates. The variation of the electric field was simulated along the following directions:

- Variation with height: This was simulated in the center of the capacitor from the sample up to the upper part of the plates (Fig. 3.3a). The values of the electric field ranges from 48.8 kV at the sample surface up to 53.6 kV at a height of 7 mm. Then, at the upper end of the capacitor, at 14 mm height, the electric field is 53.6 kV. Moreover, the maximum We in the experiments was $We = 26$, at which the maximum rebounding height is below 14 mm. Accordingly, in the range of the experimental rebounding heights, the electric field fluctuations are less than % 5 around the average value. Hence, the electric field homogeneity can be reasonably assumed in the vertical direction under our experimental conditions.

- Variation with the lateral position: The simulation was done in the x-direction at half height of the electrodes and at the height of the sample. At half height, the electric field ranges from 52.7 kV/m to 58.6 kV/m, leading to a variation of $\sim$10% for the whole range (Fig. 3.3b). At the height of the sample, the electric field varies from 48.8 kV/m in the middle between the plates up to 66.8 kV/m at the edges (Fig. 3.3c). Here, the fluctuation is stronger than the other simulated directions. Nevertheless, the experiments were performed with drops falling in the center position between the plates. These drops were deflected no more than 2 mm of lateral distance from the first and second contact with the surface. This displacement implies a variation of less than 1 kV/m, i.e., an error of %2. Thus, the electric field can be considered homogeneous in the lateral range

used for the experiments.

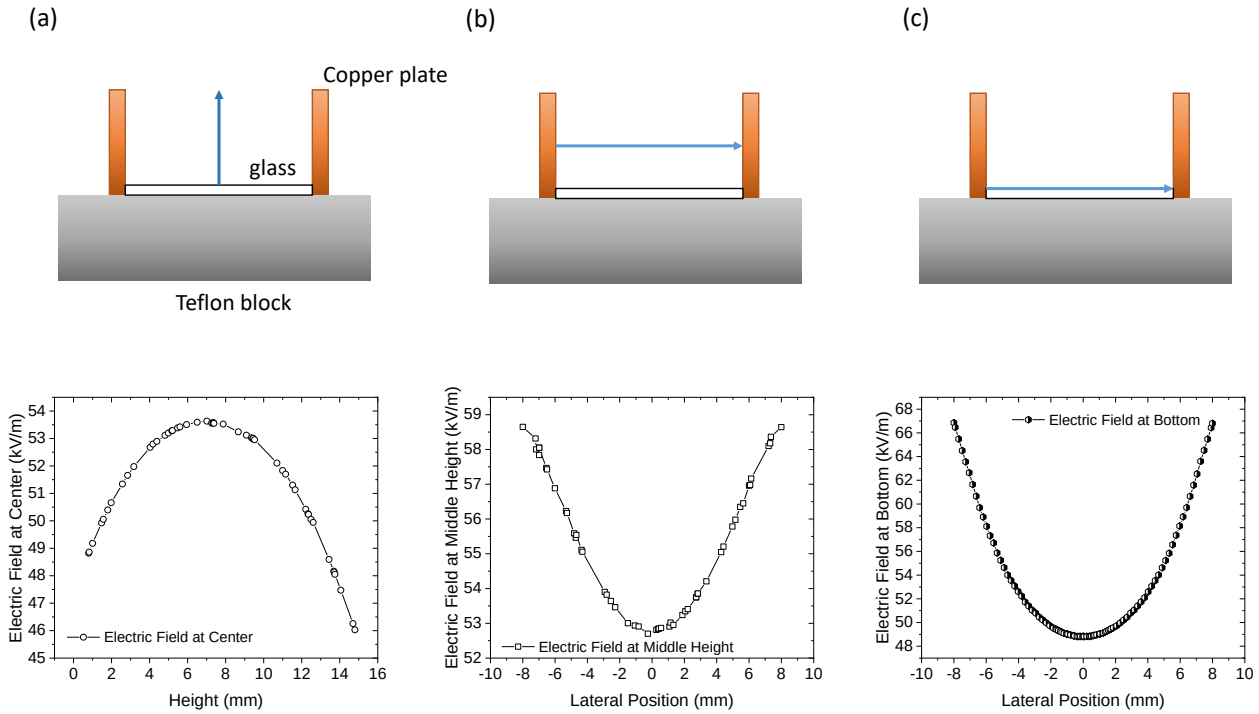

Figure 3.4: Top (a-c): Schematics indicating the line along which the electric field was calculated by a blue arrow. Bottom (a): Electric field as a function of the height. Bottom (b): Electric field as a function of the lateral position at half height. Bottom (c): Electric field as a function of the lateral position at sample surface. Blue arrows represent the simulated direction of the electric field.

Lateral acceleration Since the electric field is constant in all directions, drops should move laterally with a constant acceleration. The speed in x-direction as a function of time for a drop deflected by the electric field from right to left is shown in Fig. 3.5. Here, the lateral speed v_x starts from values close to zero at the moment of taking off, up to speeds above 80 cm/s. A straight line can be clearly fitted in the data points, which means that drops move with a constant acceleration from right to left.

As the initial lateral speed, v_{0x} is around 0, it justifies eqn. 2.1.2. The fluctuations of the speed are generated by the oscillations of the drop upon impact. As higher is We, these deformations are more pronounced. Moreover,

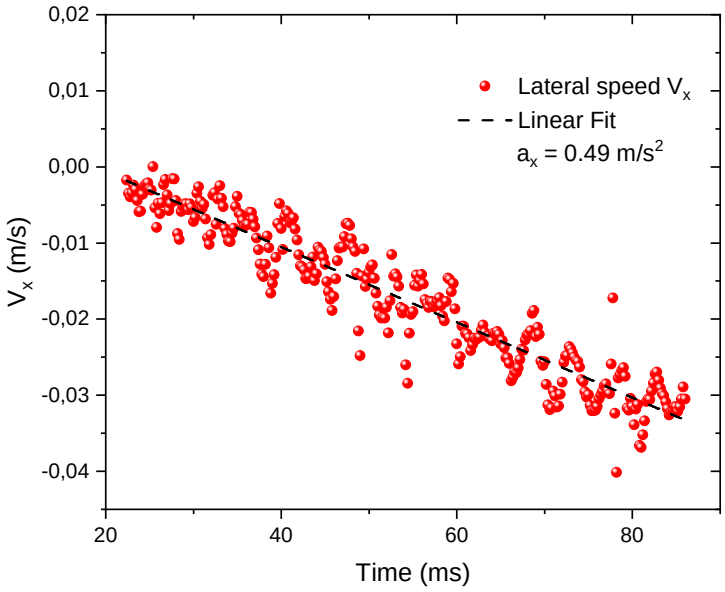

Figure 3.5: Lateral speed versus time of a rebounding drop deflected by an electric field of 55 kV/m. The slope represented by the black dashed line equals the lateral acceleration of 0.49 ± 0.009.

stronger impacts also lead to higher rebounding heights, which allows the drop to be more time in the air covering a longer horizontal distance.

3.5.1 Independence of charge and electric field

To rule out drop charging by polarization before impact, drop charge measurements were performed at different electric fields. The drop charge remains constant under different applied electric fields, ranging from 40 to 53 kV/m (Fig. 3.6). This means that the observed charging phenomenon is independent on the electric field in our experiments, and a consequence of the interaction between the drop and surface.

It is important to mention that, a drop can be deflected or even deformed due to the electric field gradients, which are more pronounced with higher fields. For instance, values above 100 kV can deflect water drops pending from the needle in the same direction of the electric field. This occurs especially at a height close to the upper part of the plates, at which the electric field is less homogeneous.

At this point, the addition of an aluminum tube to shield the drop and needle from field gradients is critical.

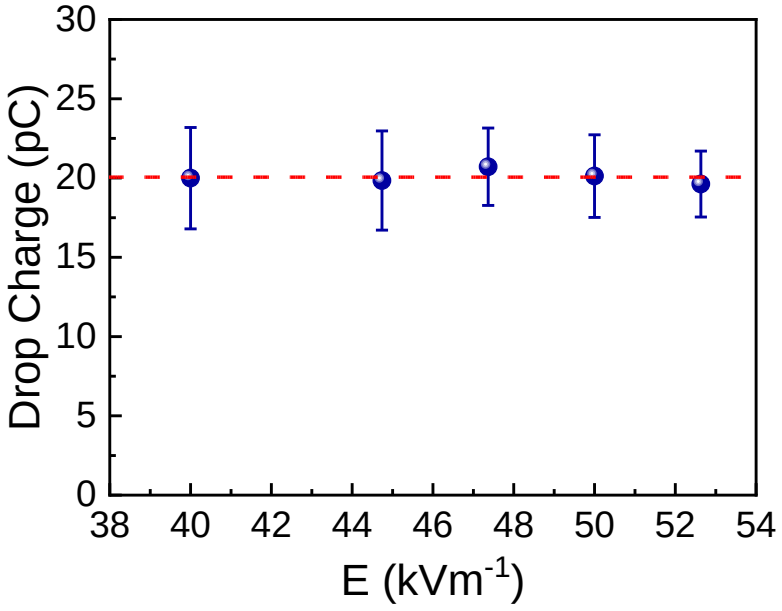

Figure 3.6: Lateral speed versus time of a rebounding drop versus deflected by an electric field of 55 kV/m. The slope represented by the Black dashed line lateral acceleration 0.49±0.009.

3.6 Drop impact dynamics

3.6.1 Spreading and retraction curves

From the drop impact videos, the evolution in time of the contact radius, $R(t)$ can be determined for the different surfaces (Fig. 3.7). Plotting $R(t)$ scaled by the maximum spreading radius, R_{max}, at different We, reveals that for surfaces based on SN, all the curves collapse onto a single curve. Therefore, in this case, the contact time remains constant when We changes. Here, the contact time is given by $\tau = t_s + t_r$, where t_s is the spreading time and t_r the retraction time. t_s covers the time from the impact until the drop reaches R_{max}, while t_r is the time between the maximum spreading until the drop takes off. In the same way than the contact time, both t_s and t_r are constant at different We for all the surfaces based on SN.

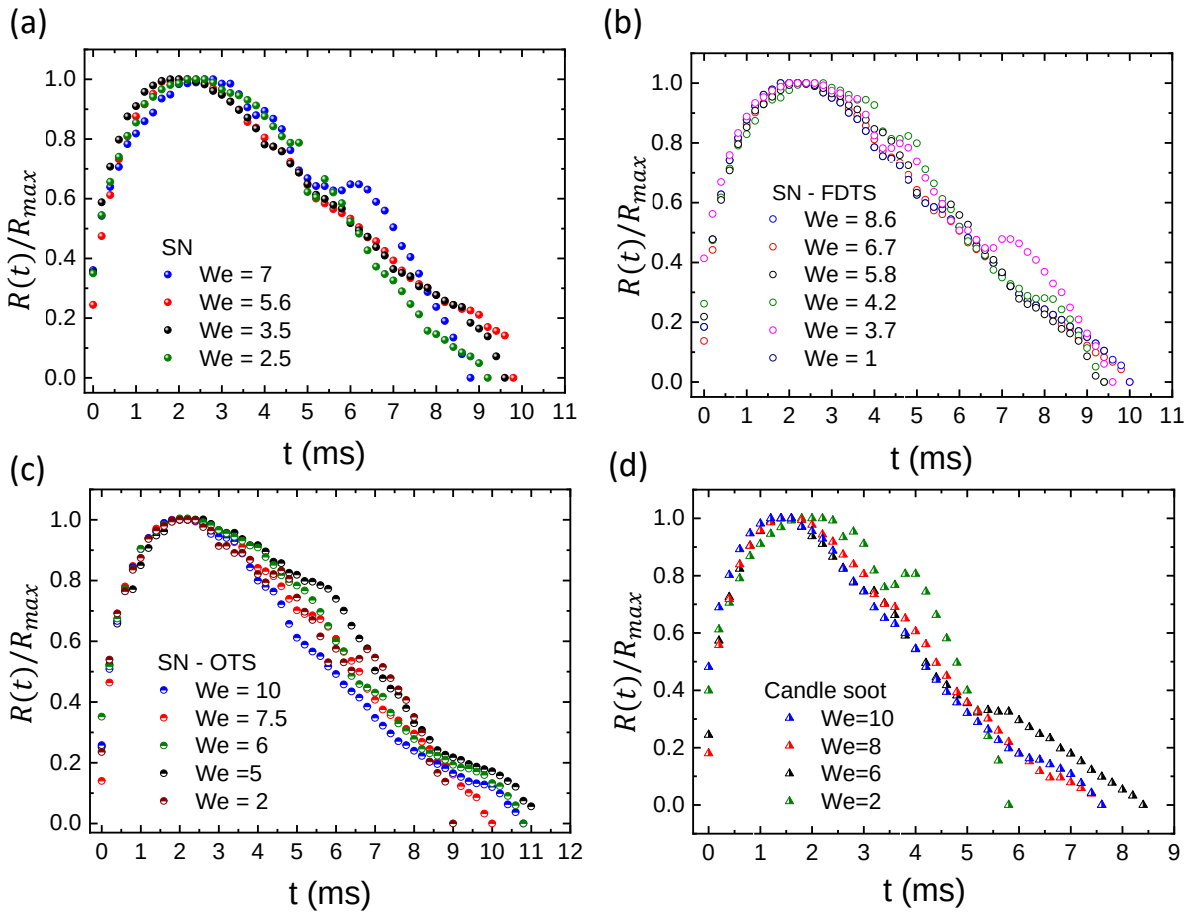

Figure 3.7: Spreading radius scaled by the maximum spreading radius as a function of time for (a) SN, (b) SN-FDTS, SN-OTS and (d) Candle soot surfaces

The contact time for candle soot surfaces clearly varies with We. The reason comes from the higher friction given by the protrusions on its structure.

3.6.2 Spreading parameter and restitution coefficient

The spreading parameter, $\beta = R_{max}/R_0$, as a function of We in logarithmic scale indicates a power law dependency (Fig. 3.8). As shown in section 1.5.6, β should scale as $\sim We^{1/4}$. This power law is fulfilled by the data above $We = 2$ (Fig.3.8, black dotted line). However, for $We < 1$, the power law slightly changes to $\beta \sim We^{0.21}$, as predicted and proved by Bartolo [73].

The 1/4 power law implies that a rebound is a dissipative process. It is quite difficult to estimate the amount of energy loss during the drop impact using

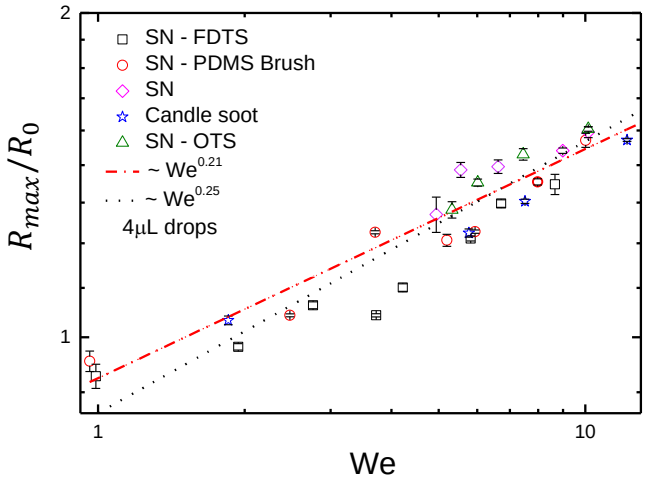

Figure 3.8: Spreading parameter as a function of Weber number. Dashed line represents the slope 0.21 and the dotted line 0.25.

the spreading parameter. Better insight of the energy dissipated is given by the restitution coefficient, e. For the different coatings presented in this thesis, e tends to decrease as We grows for $We > 2$. Hence, increasing the We, the initial kinetic energy of the drop will dissipate more. In particular, SN-FDTS can dissipate a minimum of 10% of the initial kinetic energy of the drop. Below $We = 2$, e decreases because the adhesion forces decrease the take off speed as the kinetic energy is too low.

3.7 Parameters influencing charge

In this section, I will present and discuss the results of drop charging under different impact conditions. Furthermore, I will analyze the dependency of charging with the Weber number, retraction speed of the contact line, type of coating, contact area and drop size, elucidating the main parameter controlling the charging of rebounding drops.

3.7.1 Speed of the moving contact line, and contact time

Why the speed of the contact line may be important? According to all the studies of charge separation by moving contact lines, there is an agreement that

this should be a non-equilibrium process. This is due to the disruption of the electrical neutrality at the solid-liquid interface, assuming the existence of an EDL. As longer is the interaction between drop and surface, more time for the system to return to the electrical equilibrium. Therefore, time scale of a process that involves the contact line movement should be fundamental in the diffusion of ions between interfaces, and then the speed of the moving contact line may affect the total amount of charge.

Average retraction speed In order to know the speed of the retracting contact line over time, $\dot{R}(t)$, the derivative of $R(t)$ was taken (Fig. 3.9). The maximum speed of the retracting movement is achieved at the spreading phase, after the moment of the impact. Then, $\dot{R}(t)$ decreases to zero when $R_(t) = R_{max}$. Subsequently, the drop retracts with a variable speed around an average value until it bounces off.

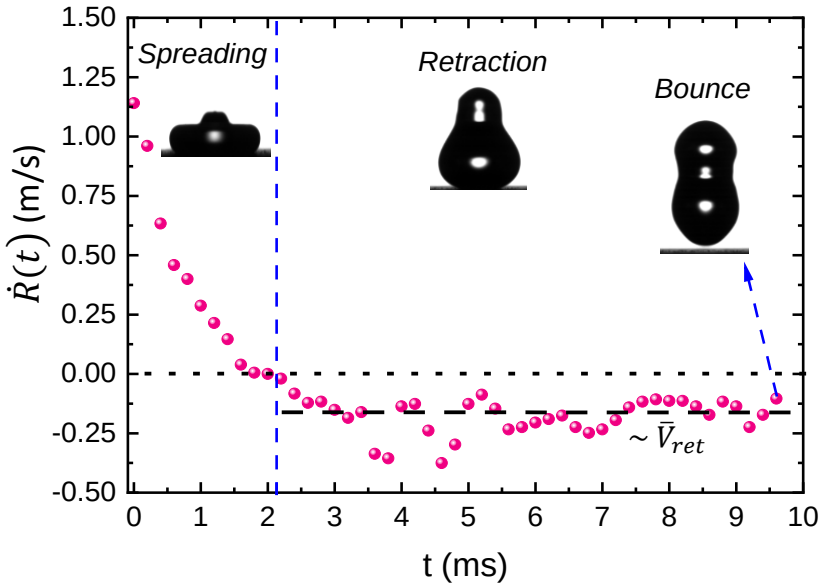

Figure 3.9: The derivative of the spreading radius $R(t)$ as a function of time. Dashed black line represents the average retraction speed $\overline{V}_{ret}$.

In order to characterize the retraction movement of the contact line, it is instructive to define the average value of $\dot{R}(t)$ as an average retraction speed:

$$\overline{V}_{ret} = \frac{R_{max}}{t_r}. \tag{3.1}$$

Using this definition, $\overline{V}_{ret}$ was calculated for 4 μL drops rebounding at different We for all the types of surfaces. The results suggest that, as faster the retraction movement is, drops acquire more positive charge. However, for the charge measurements of drops of different volumes released from the same height, the opposite trend is observed. This means that drop charge increases with drop size, while $\overline{V}_{ret}$ decreases. Such behavior excludes $\overline{V}_{ret}$ as a dominant parameter in the charging process. Thus, charge of bouncing drops is independent of $\overline{V}_{ret}$. The influence of volume in the drop charging will be further discuss in the next section with the rest of parameters (We, contact area)

Average spreading speed In a similar way as $\overline{V}_{ret}$, the speed of the contact line when a drop spreads on the surface may influence the charge separation. Ions may be absorbed by the surface, so the speed of the spreading can affect the amount of ions deposited on the surface. In the following chapters, I will further discuss about the drop impact phase where the charge separation should occur.

The speed of the spreading contact line will be characterized by an average spreading speed:

$$\overline{V}_s = \frac{R_{max}}{t_s} \tag{3.2}$$

Drop charge as a function of $\overline{V}_s$ shows the same trend compared to $\overline{V}_{ret}$, for the same experiments with 4 μL drops and different volumes (Fig. 3.10). Thus, $\overline{V}_s$ does not influence the drop charge and it is also excluded as a controlling parameter in charge separation. Note that the values of $\overline{V}_s$ can be even 4 times greater than the values of $\overline{V}_{ret}$ for $4\mu L$. As these drops spreads in $t_s \sim 2s$, four times less than t_r, there is an obvious difference in the speeds.

Contact time The time scale of charge separation processes with moving contact lines seems to be crucial. In fact, both sliding and bouncing drops show

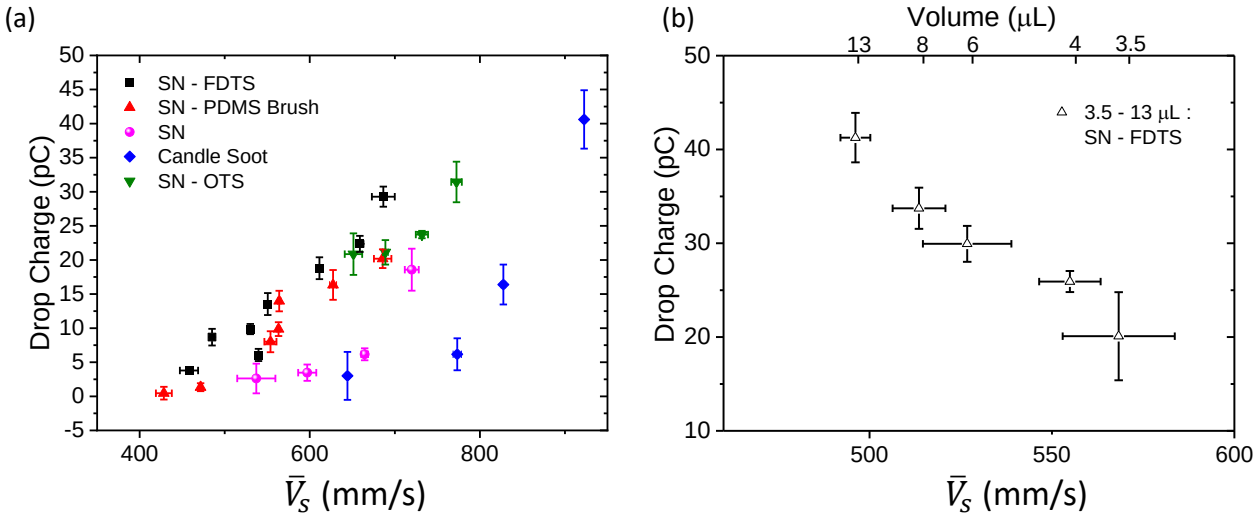

Figure 3.10: (a) Drop charge vs. the average spreading speed $\overline{V}_s$ for 4 μL drops impacting on superhydrophobic surfaces at different Weber numbers. (b) Drop charge vs. $\overline{V}_s$ for drops of different volumes impacting the same superhydrophobic surfaces, but at the same impact speed. The opposite trends for both cases suggest that $\overline{V}_s$ does not influence charge separation of bouncing drops.

the same order of magnitude in the contact line speed (sliding speed, $\overline{V}_{ret}$ and $\overline{V}_s$). The change in the speed can be affected by the area covered by the drop on the surface and, of course, the contact time.

For the case of 4 μL drops impacting at different impact speeds, the drop spreads further on the surface when We is greater, which increases R_{max}. In addition, as the contact times and t_r remains unaltered at different We. Accordingly, t_s and t_s are also constant. As a result, both parameters do not affect the change in $\overline{V}_s$ and$\overline{V}_{ret}$. In fact, the change in the speed of the moving contact line is given by the increase in R_{max}. This suggests that the surface area contacted by the drop is the crucial parameter controlling drop charge.

3.7.2 Contact area as the dominant parameter in the charging process

Our experiments reveal that an increment in Weber number, drop volume and contact area leads to and increase in drop charge. All these parameters can be changed by varying the impact speed and drop radius, so that it is instructive

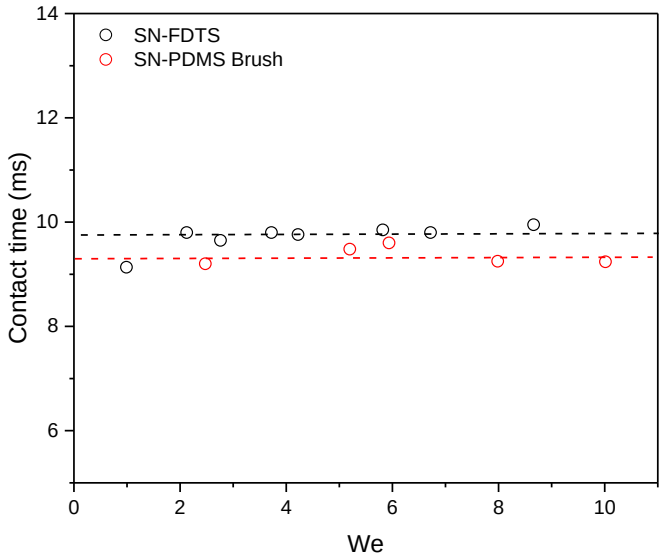

Figure 3.11: Contact time as a function of Weber number for SN-PDMS brush and SN-FDTS.

to analyze all together.

Either for experiments using a constant drop volume released at different heights or varying the drop volume released from the same height, the drop charge increases as higher is We for all the coatings (Fig. 3.12a), in the range where no secondary drops form ($1< We <7.5$). This linear increase can be represented by the following relation:

$$Q = \beta(We - We_0), \tag{3.3}$$

where $We_0 = 1$ is the lowest value of We where a rebound occurs. β is a constant depending on the surface coating, with values ranging between 2 and 5. In addition, it was observed that in the regime where break up takes place, the drop charge tends to remain (Fig. 3.12a, shaded region) . The break up implies the loss of the initial drop volume, which certainly would affect the charge calculation according eqn. 2.4. For this reason, drop impacts at $We < 26$ were performed to avoid a significant amount of volume loss. The remaining amount of volume after the ejection of secondary drops was $\sim$ 3.7-3.8 μL. This

amount is a reasonably good estimate of the charge for a 4 μL drop. Note that, the value of charge saturation varies accordingly with the surface coating. This suggests that, although the surface chemistry does not affect significantly the amount of charge as We, it definitely determines the limit of the maximum drop charge. Increasing We leads to an increase in contact area $A_{max} = \pi R_{max}^2$,

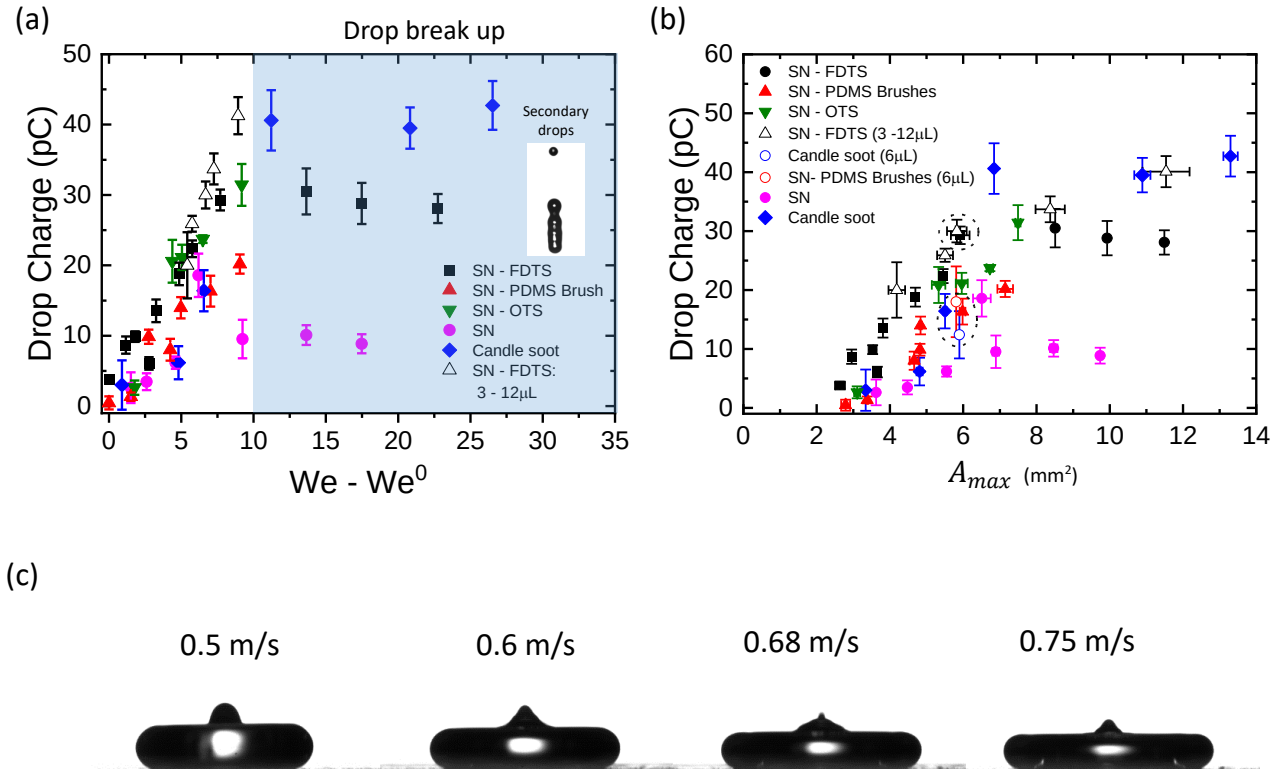

Figure 3.12: (a) Drop charge as a function of Weber number. We^0 represents the minimum Weber number at which a rebound is possible. The shade region remarks the range where ejection of secondary drops take place. (b) Drop charge as a function of the maximum contact area A_{max}. Both plots show an initial linear increase of charge, followed by a charge saturation regime. This suggests that drops cannot acquire more charge after reaching certain A_{max}.

covered by the drop during the spreading phase. Here, a circular spreading area is assumed. As a result, the drop charge also increases with increasing the contact area (Fig. 3.12b,c). This trend is the same compared to the dependency with We, where a saturation charge is reached. So far, it is clear that contact area can be controlled by the parameters of impact speed and drop size (volume) included in the definition of We.

To elucidate the governing parameter of drop charging, the experiments of

6μL drops released from the same height on candle soot and SN-PDMS brush are crucial. These experiments indicate that drops impacting at different We and volumes, but with similar A_{max} values, exhibit quite similar values of charge. Thus, charging is mainly depending on the maximum contact area of impacting drops.

3.7.3 Theoretical model for charge separation of bouncing drops

In this section, I will derive a theoretical model to explain charging of bouncing drops based on the slide electrification model proposed by Stetten et. al. [57]. Since both sliding and bouncing involve charge separation by contact line motion, the mechanism should be similar. Therefore, I consider that an (1) EDL is form near the liquid solid interface, (2) hydroxyl ions dissociated in the drop are absorbed by the hydrophobic coating of the surface, and (3) a fraction α of the surface charge density σ_L of the debye layer is deposited on the surface at the rear of the drop, as expressed in eqn. 1.47 for sliding drops. Therefore, I also consider (4) the retraction motion as the phase where the charged is deposited on the surface.

The EDL is estimated to form in ~ 6 μs [57]. This means that for bouncing drops, the EDL should forms in the spreading phase, which is actually comparable to the wetting state of a drop deposited on a surface before sliding. Similarly, the motion of the contact line during the sliding process should be equivalent to the retraction phase of an impacting drop. Consequently, I assume that the charge separation occurs as the drop starts to retract. It is also possible that charges can be absorbed by the surface during spreading. However, the presence of counter ions should maintain the electrical neutrality of the EDL. Thus, the real charge separation most likely takes place when the drop retracts, which would disrupt the EDL in such a way that the electrical equilibrium breaks.

The infinitesimal change in the contact area as the drop retracts can be written as:

$$dA = 2\pi r dr, \tag{3.4}$$

,

where r is the retracted radius. Therefore, the infinitesimal charge left on the surface can be expressed as follows:

$$dQ(r') = \sigma_L \alpha (2\pi r') dr'. \tag{3.5}$$

Here, α is the same transfer coefficient defined previously for the model of sliding drops (section 1.6.3). Note here that we use r, which is a coordinate behind a drop that has retracted to radius r': Replacing the definition of α stated in eqn. 1.48 into eqn. 3.5 leads to:

$$dQ = -2\pi\sigma_L \left(\alpha_0 + \frac{\alpha_1 q}{C_d k_B T} Q \right) r' dr', \tag{3.6}$$

which can be expressed as a differential equation:

$$\frac{1}{r'} \frac{dQ}{dr'} - \frac{Q}{\lambda_r^2} - 2\pi\sigma_S^0 = 0, \tag{3.7}$$

with

$$\lambda_r^2 = \frac{C_d k_B T}{2\pi\alpha_1 q \sigma_L}. \tag{3.8}$$

and

$$\sigma_S^0 = \sigma_L \alpha_0. \tag{3.9}$$

Since it is assumed that the spreading does not involve charge separation, the drop charge will zero at the moment of maximum spreading. This means that $Q(r' = R_{max}) = 0$. With this condition, eqn 3.7 can be solved to obtain the drop charge as a function of r'.

$$Q(r') = -2\pi\sigma_S^0 \lambda_r^2 \left(1 - \exp\left(\frac{r'^2 - R_{max}^2}{2\lambda_r^2} \right) \right). \tag{3.10}$$

This equation implies that a drop is progressively gaining positive charge

as it retracts, depositing negative charge on the surface until reaching $r' = 0$ (Fig. 3.13a). At this point, the drop bounces off of the surface. Hence, the charge that I measure experimentally is :

$$Q(R_{max}) = -2\pi\sigma_S^0\lambda_r^2\left(1 - \exp\left(\frac{-R_{max}^2}{2\lambda_r^2}\right)\right) \tag{3.11}$$

Note that now, the drop charge is represented in terms of R_{max}, so that it can also be in terms of A_{max}:

$$Q(A_{max}) = -2\pi\sigma_S^0\lambda_r^2\left(1 - \exp\left(\frac{-(A_{max} - A_0)}{2\pi\lambda_r^2}\right)\right), \tag{3.12}$$

where $A_0 = 0.57$ mm^2 is the minimum contact area at which charge is detectable. As a example, the drop charge as a function of radius r' scaled by the Max. radius R_{max} is shown in Fig. 3.13b), with the parameters $\sigma_S^0 = 12$ μC/m^2 and $\lambda_r = 2.7$ mm. These parameters were obtained from [57] for a perfluorodecyltrichlorosilane (PFOTS) surface, which a hydrophobic surface typically used for slide electrification experiments. Although the characteristic parameters for a PFOTS surface will likely be different for the surfaces discussed in this thesis, the trends should be the same. The parameters for our surfaces will be obtained in the next section, where I will compare the experimental results with the model. It is important to note that, if the maximum radius is large enough, the drop reach a saturation point even before rebounding off of the surface (Fig. 3.13b). To better understand this behaviour, it is instructive to derive an equation for the distribution of surface charge. Combining Eqs. 3.4 and 3.9, the surface charge can be represented in terms of the derivative of the total charge with respect of radius:

$$\sigma_S = \alpha\sigma_L = \frac{1}{2\pi r}\frac{dQ}{dr}, \tag{3.13}$$

which leads to :

$$\sigma_S(r') = \sigma_S^0\left(\exp\left(\frac{r'^2 - R_{max}^2}{2\lambda_r^2}\right)\right). \tag{3.14}$$

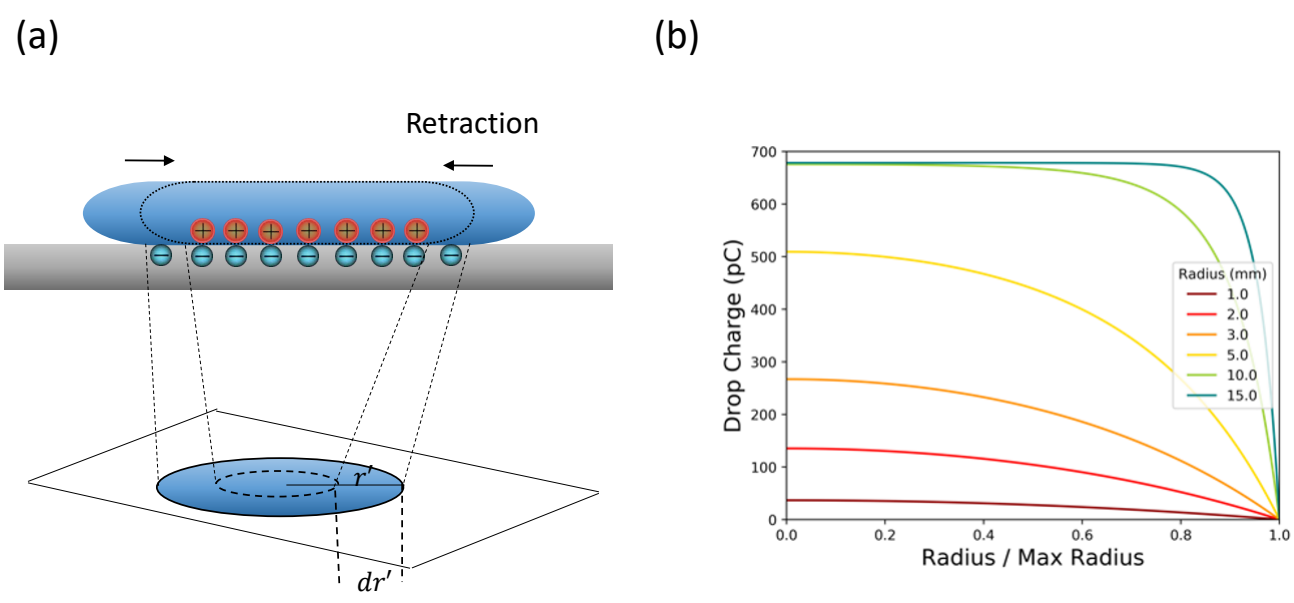

Figure 3.13: (a) Schematic of the retraction process of an impacting drop. Drop covers an area $2\pi r' dr'$ depositing negative charge on the surface. (b) Drop charge as a function of the normalized retracting radius $R(t)/R_{max}$. The maximum value of charge during retraction is reached at the moment of rebound, since no more charge is deposited on the surface.

Plotting σ_S^0 as a function of r'/R_{max} with the parameters of a PFOTS surface, reveals that the surface charge density left behind starts at its highest value and decreases with radius due to the increasing potential between drop and surface (Fig. 3.14a). If the starting radius is large enough ($R_{max} = 10$ mm), the surface charge saturates to zero because the drop capacitor becomes full and no further charge is deposited. This leaves an outer ring saturated with negative charge on the surface and a depletion zone where the drop cannot deposit more charge (Fig. 3.14b). For smaller drops ($R_{max} = 1$ mm, $R_{max} = 5$ mm), drops do no saturate, so that the deposited charge is distributed over the whole drop impact area. It is important to note that these predictions hold true only if there is a constant drop capacitance. This is likely true for water drops of the same volume, however it is not necessarily true if the volume is changed.

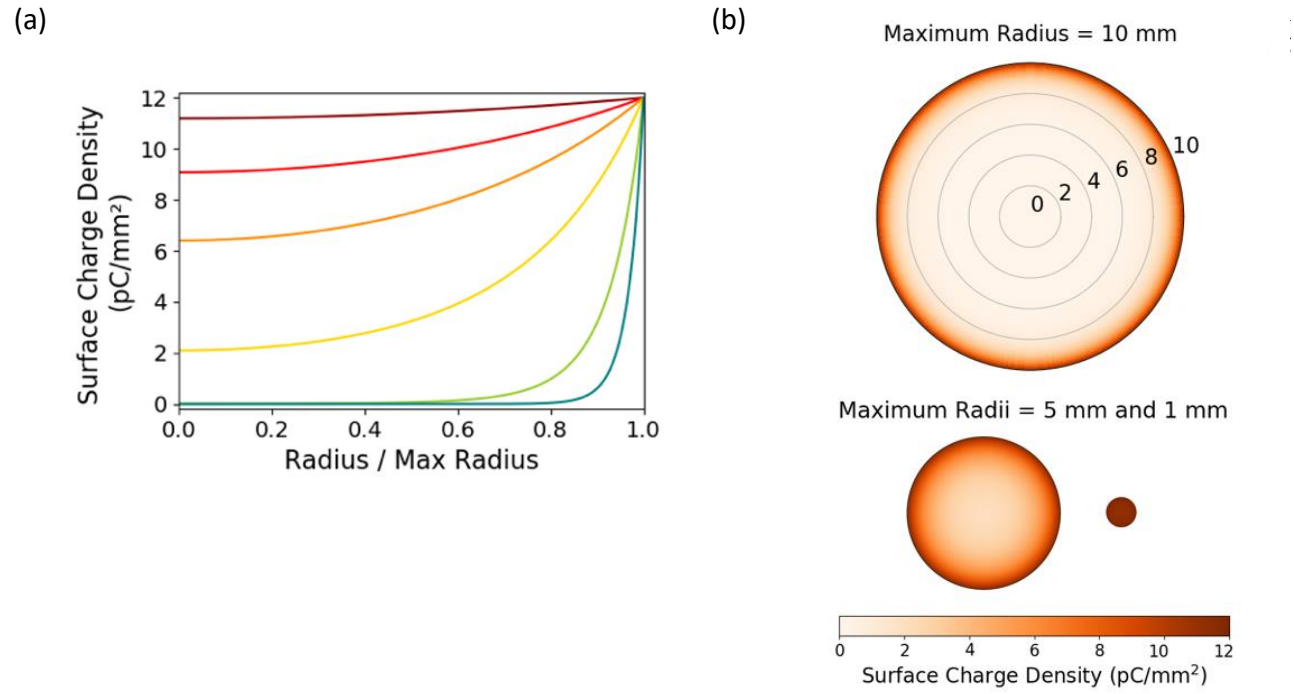

Figure 3.14: (a) Surface charge density vs. the retracting radius normalized by the maximum spreading radius $R(t)/R_{max}$. Colors represent the same radius shown in Fig. 3.13b). (b) Sketch of the surface impact area. For large drops ($R = 10$ mm), the charge is concentrated in the outer ring of the impact area, because drops are already saturated. For smaller drops ($R = 1$ mm, 5 mm) the charge is distributed more homogeneously across the entire deposition area.

3.7.4 Comparison between experiments and theoretical model

The compatibility of our proposed model and the experimental results was checked by fitting eqn. 3.12 in the data of drop charge vs. A_{max} shown in Fig. 3.12. From the fitting it was observed a good quantitative agreement between theory and experiments (Fig. 3.15b). Furthermore, the characteristic parameters σ_S^0 and λ_r for our surfaces can be obtained from the fitting. In particular, $\sigma_S^0 = 14$ μC/m^2 and $\lambda_r = 0.6$ mm for SN-FDTS, $\sigma_S^0 = 5$ μC/m^2 and $\lambda_r = 0.52$ mm for SN, and $\sigma_S^0 = 17$ μC/m^2 and $\lambda_r = 0.63$ mm for candle soot. The lowest value of σ_S^0 corresponds to SN, as expected because it exhibit less charging compared to the surfaces with fluorinated coatings. This supports the fact that fluoropolymers tend to absorb negative ions from water, becoming the surfaces with more pronounced charging.

Both σ_S^0 and λ_r are naturally dependent on the surface chemistry and the

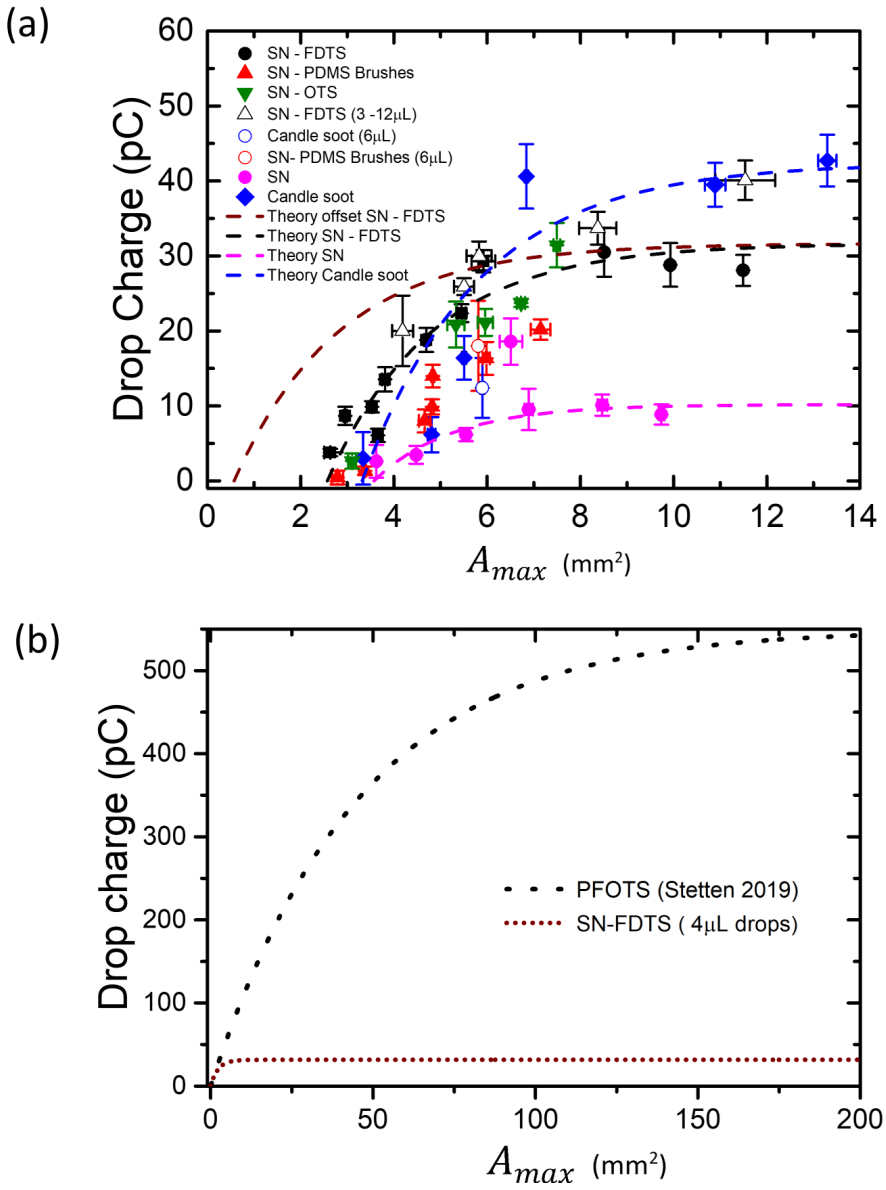

Figure 3.15: (a) Experimental data and theoretical prediction of drop charge versus maximum spreading area A_{max} for SN-FDTS (shown in (b), brown dashed line), SN and candle soot is plotted on the same axes. The parameters used for the fitting were: $\sigma_S^0 = 5$ μC/m^2 and $\lambda_r = 0.52$ mm for SN; $\sigma_S^0 = 17$ μC/m^2 and $\lambda_r = 0.63$ mm for candle soot. All the surface coatings have the fits starting from A_0 as the minimum measured area. SN-FDTS data is fitted with an additional curve using $A_0 = 0.57$mm for a resting drop, as predicted by the model (brown dashed line). (b) Drop charge as a function of an extended range of $Amax$ for SN-FDTS and a PFOTS surface(taken from [57].

drop capacitance. In fact, σ_S^0 represents the slope of the first data points of Q vs. A_{max}. Taking the derivative of eqn. 3.12 with respect to A_{max} leads to :

$$\frac{dQ}{dA_{max}} = -\sigma_S^0 \exp\left(-\frac{A_{max} - A_0}{2\pi\lambda_r^2}\right). \tag{3.15}$$

Therefore, at low A_{max}, $dQ/dA_{max} \sim \sigma_S^0$, so that the drop charge is proportional to A_{max} under this condition. Note that in Fig. 3.15a), the brown fitted curve for SN-FDTS starts from $A_0 = 0.57$ mm^2 as a comparison with the rest of the fittings. This minimum contact area corresponds to the area covered by a resting drop on SN-FDTS surface at $We = 0$, where there is no retraction, so that charging does not occur. The different A_0 leads to a clear offset between theory and experiments. Now, expanding the plotting range, the comparison between the theoretical predictions for PFOTS and the same brown fitted curve indicates that for a hydrophobic surface the charge of a rebounding drop can be even more than 10 times higher than the superhydrophobic one. However, as the surface chemistry of the compared surfaces is quite similar, no significant difference in charge is expected. Consequently, two important conclusions arise. Firstly, considering the difference in the values of λ_r for both type of surfaces, the charge saturation point is set by this parameter. Secondly, the difference in charge for hydrophobic and superhydrophobic surfaces should be a consequence of the different effective drop contact areas. Rebounding drops on superhydrophobic surfaces remain in the Cassie-Baxter state, which means that only a fraction of the apparent contact area represents the effective contact area covered by the drop. On a smooth hydrophobic surface, the apparent and real contact area will be essentially the same, as there will be no air gaps in the contact area. Such difference can be seen in Fig. 3.15b), where the theoretical prediction for SN-FDTS is plotted with the one for PFOTS hydrophobic surfaces from Stetten et al. [57]. Clearly, PFOTS charge more and saturates with a charge value 10 times higher than SN-FDTS. As both PFOTS and SN-FDTS have similar surface chemistry, the significant different in charging must be a result of the different effective contact area. Therefore, this also explains the offset seen in Fig. 3.15a), since our experimental values of A_{max} would be shifted to the right of the plot due to an overestimation of the real contact area. In

particular, data points for SN-FDTS (black dots, Fig. 3.15a) were shifted to the left, they should fit better with the brown curve plotted for $A_0 = 0.57$ mm.

3.7.5 Calculation of the effective contact area on a superhydrophobic surface

For a further insight of the influence of the contact area in the charge separation process, I calculate the area fraction of a drop when is in contact with a superhydrophobic surface.

Using eqn. 1.5 for the Cassie state, the area fraction of the surface f_1 can be written as:

$$f_1 = \frac{\cos\theta^* + 1}{\cos\theta_1 + 1} \tag{3.16}$$

Here, θ_1 is the equilibrium contact angle of a smooth SN surface. Such surface cannot be fabricated. As an alternative, it was considered $\theta_1 = 113°$, which is the static contact angle of a PFOTS surface. As PFOTS and SN coatings have similar surface chemistry, their equilibrium contact angles should be comparable. Taking also $\theta^* = 150°$ yields $f_1 = 0.22$. This means that 22% of A_{max} is in contact with a impacting drop. Therefore, as larger the surface contact area, the higher the charge deposition, because more hydroxyl ions can be absorbed by the hydrophobic coating.

3.7.6 Additional experiments

3.7.6.1 Experiments with salts

In this thesis, I assume that ions naturally present in water play a relevant role in the formation of the EDL. Therefore, adding salts in water will most likely influence the amount of charge, as reported in previous studies. The following salt solutions at different concentrations (0-10 mM) were tested with 4 μL drops impacting from 2.8 cm height:

- Calcium Chloride ($CaCl_2$)

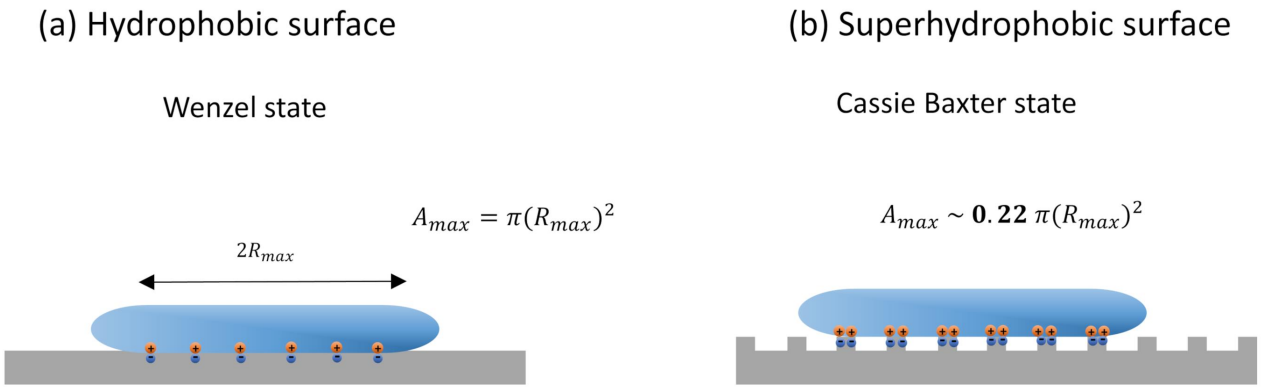

Figure 3.16: (a) Drop impacting a hydrophobic surface. The droplet is in contact only with the surface (Wenzel state). (b) Drop impacting a superhydrophobic surface. The drop is in contact with air pockets and the surface, in the so-called Cassie-Baxter state. The contact area in this state is a fraction of the area covered in the Wenzel state. The fraction "0.22" is characteristic for a SN-FDTS surface and it was calculated by eqn. 3.16

- Sodium Chloride (NaCl)
- Iron (III) Chloride ($FeCl_3$)
- Lantanium Chloride ($LaCl_3$)

As control sample, I consider a 4 μL pure water drop impacting from 2.8 cm height, with charge 30 pC. The experiments showed an increase of the drop charge for all the solutions, except for $FeCl_3$ when the salt concentration was below 0.5 mM (Fig. 3.17). For salt concentrations above 0.5 mM, the amount of charge starts to decrease.

The decrease in charge due to high salt concentrations may be understood by the degree of screening of the surface charge. As mentioned in section 1.7, an increment in salt concentration leads to more ions available to screen the surface charge, which at the same time decreases the Debye length λ_D. This may hinder the absorption of hydroxyl ions to the surface. However, the idea of the screening effectiveness cannot explain the initial increase of charge. So far, both the initial increase and subsequent decrement of charge is still not well understood. Our results suggest that the amount of charge can be maximized by small concentrations of salts, and that the type of salt affects how pronounced is the charge increase .

3.7.6.2 Charging of different liquid drops

Previous studies of drop charging showed that charge separation is also possible with such liquids, so that different ions species could play some role in the charging phenomenon. Based on this antecedent, I tested liquids with different viscosities and surface tensions compared to water. Since the surface tension and viscosity can affect the drop impact dynamics, the charging may also be influenced. The following liquids were tested:

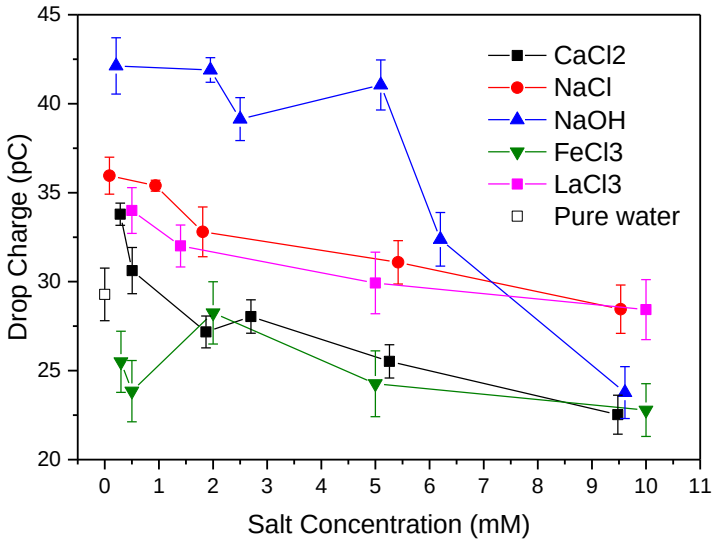

Figure 3.17: Drop charge vs. Salt concentration. Charge tends to increase at concentrations below 0.5 mM for most of the solutions. Increasing the concentration leads to a decrease in charge.

- Dimethylformamide (DMF): $\gamma = 37.1$ mN/m, $\sigma = 0.92$ mPa s, Dielectric constant: 37.51
- Dimethyl sulfoxide (DMSO), $\gamma = 43.5$ mN/m, $\sigma = 2$ mPa s, Dielectric constant: 36.71
- Hexadecane, $\gamma = 27.5$ mN/m, $\sigma = 3.45$ mPa s, Dielectric constant: 2

- Toluene, $\gamma = 28.58$ mN/m, $\sigma = 0.55$ mPa s, Dielectric constant: 2.35

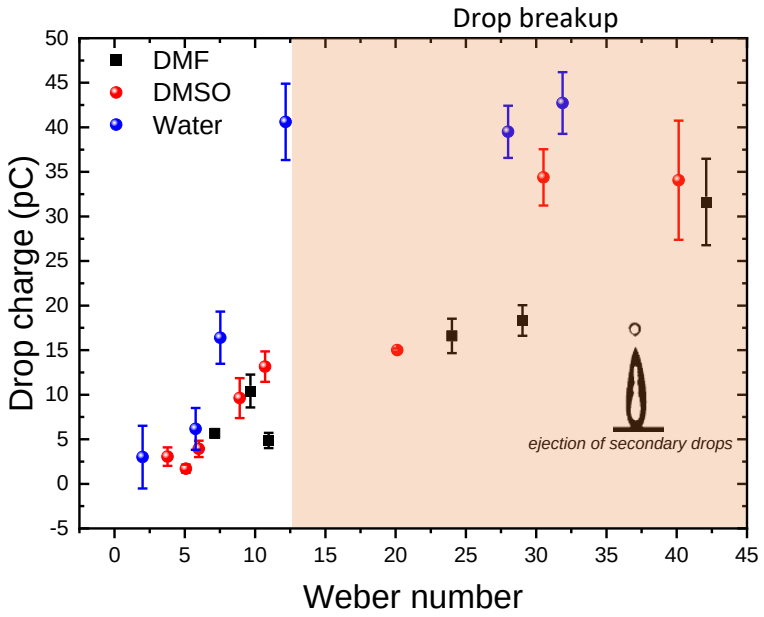

Figure 3.18: Drop charge as a function of Weber number for DMF, DMSO and water

From all the liquids tested, only DMF and DMSO drops can acquire charge. For these liquids, an increase of charge with We was also observed. (Fig. 3.18). In fact, both liquids exhibit charge values comparable to water drops impacting on candle soot (blue dots), which was added in the plot as a comparison from the results of chapter 2. For the case of Hexadecane and Toluene drops, no charging takes place, which is most likely due to their small dielectric constants. The dielectric constant represents the capacity to store charge under electric fields, so that charging should decrease significantly as the dielectric constant decreases.

The possibility of charging with different liquids than water suggests that not only hydroxyl ions can take part of the charging process, but other ions species such the ones in salt solutions. Further experiments are required to know in detail the specific ions, most likely, absorbed by the surface and allowing positively charged rebounding drops.

3.7.6.3 Splashing drops

When increasing impact energies, droplets start to splash during impact. The charging during splashing was tested. 10 μL water drops were dispensed from 70 cm height ($We = 344$), on a SN-FDTS surface. An electric field of $E = 33$ kV/m was applied to analyze the deflection of the primary and secondary drops. The experiment serves to further study charge separation at really high We and as another confirmation of charging of secondary drops due to break up.

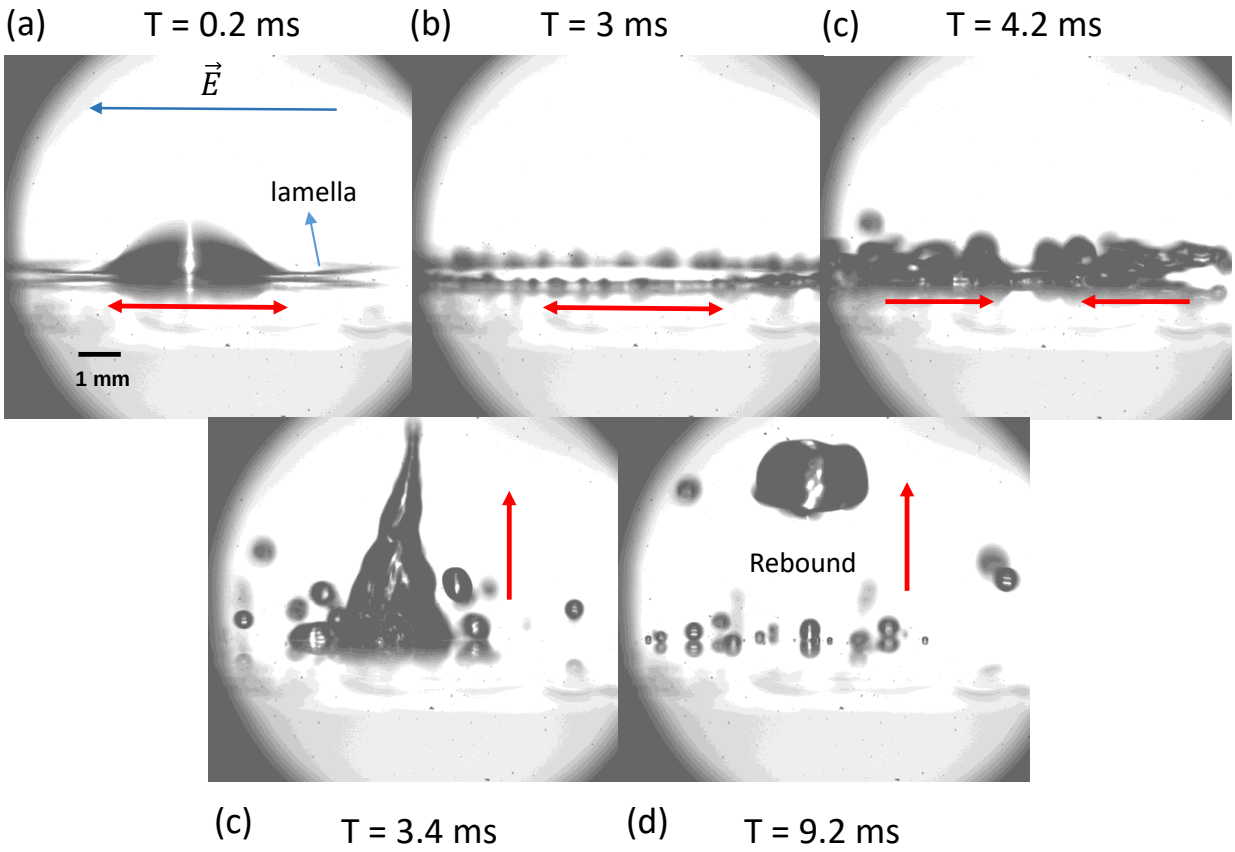

Figure 3.19: 10 μL drop impacting a Superhydrophobic surface made of fluorinated silicon nanofilaments (SN-FDTS). After impact, the drop spreads forming a thin lamella. From the the lamella, fingering leads to the ejection of secondary drops.

From the splashing experiments, it was observed what is called "receding breakup". After the impact, the drop forms quickly an spreading thin lamella that moves laterally at a certain separation angle with the surface (Fig. 3.19a). As a result, the edge of the expanding lamella is no in contact with the surface during the spreading, which has been reported previously [95]. When the liquid

reaches the maximum spreading, fingering at the edge of the lamella forms (Fig. 3.19b). From these "fingers" some satellite drops can be ejected. During the retraction phase, the liquid fingering not ejected during spreading is pulled back due to the retraction force. This leads to the ejection of drops in the retraction motion direction (Fig. 3.19c). Finally, the drop moves with an upward momentum (Fig. 3.19c) until it completely or partially rebounds (Fig. 3.19d). High impact velocities can lead to drop impalement, which affect the lateral direction of the rebound even in absence of the electric field. Consequently, it is not possible to even obtain the sign of the drop charge for the main drop.

Some secondary drops were slowed down and even changed completely their trajectory (Fig. 3.20), while others were accelerated in one direction. This is clearly an indication of spontaneous charging. However, it is difficult to distinguish between the contribution of the electrostatic force and the kinematic of drops by drop breakup. Calculating the charge based only on the acceleration of drops may lead to uncertainties. One solution may be to use a higher electric field. Changing the distance between the copper plates is another option, but the sample would be quite small and the secondary droplets would touch the plates almost immediately.

For a better analysis of charging during splashing, an hydrophobic surface is more suitable, since drops should acquire further charge and deflect easier. In conclusion, charging occurs for splashing on superhydrophobic surfaces, in such a way that positive and negative charged drops are ejected from the primary drop.

3.7.7 Summary

In the first part of the chapter, I showed that the charge of bouncing drops on superhydrophobic surfaces can be reproducibly measured by analysing their trajectory once they are deflected by a lateral homogeneous electric field. The independence of charging on the applied electric field demonstrates that the phenomenon is a result of the interaction between the drop and surface, most

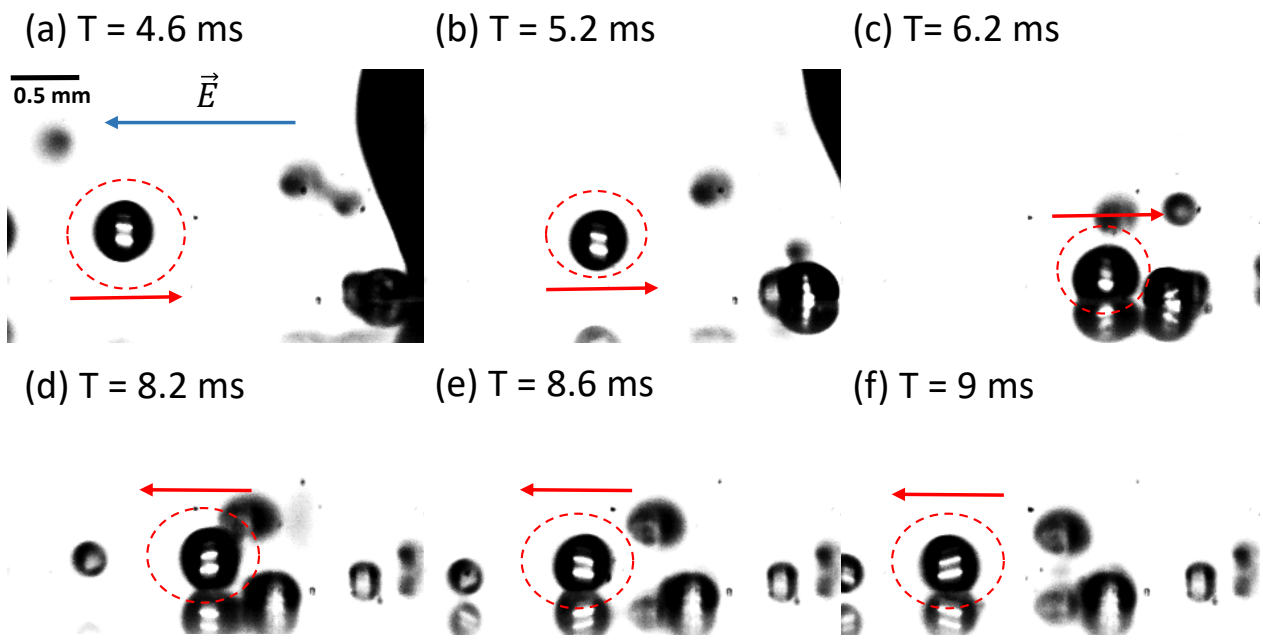

Figure 3.20: 10 μL drop impacting a Superhydrophobic surface made of fluorinated silicon nanofilaments (SN-FDTS). After impact, the drop spreads forming a thin lamella. From the the lamella, fingering leads to the ejection of secondary drops.

likely due to the absorption of hydroxyl ions from the drop. I tested the influence of Weber number, drop contact area, surface coating, drop volume and the speed of the retracting contact line in the charging process. The surface coating can clearly increase the amount of charge when involves a fluorination. However, the contact area generates a more significant effect in charging. This is due to a further spreading on the surface increases the charge transfer. The change in this parameter is a direct consequence of varying the rest of the tested parameters.

In the second part of the chapter, I derived a theoretical model to explain charging of bouncing drops based on the sliding drops electrification. The model considers that charge separation occurs during the retraction phase, where the drop deposits charge at the rear of the receding contact line. The good agreement and compatibility of theory and experiments suggest that both charging of bouncing and sliding drops are a result of the same mechanism of charge separation.

Chapter 4

Self-generated electrostatic forces on hydrophobic surfaces

In this chapter, I use the same experimental method described in Chapter 3, to measure the charge of rebounding drops, but now from hydrophobic surfaces. So far, the quantification of charging of bouncing drops on hydrophobic surfaces has not been studied consistently. This is mainly due to difficulties in the fabrication of surfaces with enough hydrophobicity to facilitate complete rebounds.

I used Teflon AF1600 (Teflon) and SU-8 micropillar arrays surfaces as a solution for reproducible charge measurements and sufficient water-repellency. Typically, drops rebound on hydrophobic surfaces either completely or leaving part of them sticking to the surface. When the rebound is complete, it is usually not vertical even in absence of an external electric field. The lateral component of the rebound arises from local pinning of the contact line by defects or chemical inhomogeneities. Therefore, to be able to apply our electric field method, we needed to prepare highly homogeneous hydrophobic surfaces. Fluorination of silicon wafers did not result in pure enough surfaces. Finally, Teflon and SU-8 micropillar arrays surfaces were found to be homogeneous enough to lead to vertical rebound in absence of electric fields. Here, I focus on addressing the following questions:

(1) Do the bouncing drops acquire more charge on hydrophobic surfaces as predicted by our model?

(2) Could the charge be suppressed using metal substrates as observed for

the slide electrification phenomenon?

(3) If self generated electrostatic forces exist, are they sufficient to influence the drop impact dynamics?

Addressing all these question will provide a more complete picture of charging by drop impact.

4.1 Materials and Methods

4.1.1 Teflon AF1600

4.1.1.1 Preparation

75 x 25 mm SiO_2 and sputter coated gold glass slides with 1 mm thick were coated with Teflon AF 1600 (Teflon) by dip-coating. The gold substrates were fabricated by sputtering a 30 nm gold layer on the glass slides, which were previously coated with 5nm chronoium to improve adhesion with gold. Afterwards, the SiO_2 slides and the gold-coated glass slides were both immersed at a speed of 90 mm/min in 1 wt% Teflon AF1600 (Sigma Aldrich) in FC-317 43 (Sigma Aldrich) for 10 seconds. The substrates were withdrawn from the solution at a constant speed of 10 mm/min. The films on the substrates were then annealed for 24 hours at 160°C in vacuum.

4.1.1.2 Characterization by AFM

With scanning force microscopy (Dimension Icon, Bruker) in tapping mode, all Teflon AF surfaces were examined (Fig. 4.1a) The SFM tips had a spring constant of 26 N/m and a nominal resonance frequency of 300 kHz (160AC-NA, OPUS). For each sample, the root mean square roughness (rms) was calculated over a 0.5 x 0.5 μm^2 area. Teflon AF1600 films were 60 nm thick with rms $\leq$ 1 nm. Variations on different samples and at different points on the samples were used to calculate errors. Error in roughness was roughly 0.1 nm.

4.1.1.3 Wetting properties

The resulting Teflon on SiO_2 and Teflon on gold surfaces were suitable to allow complete rebounds (Fig. 4.1b), with contact angle hysteresis of $12° \pm 2°$ and 13°, respectively, and a static contact angle of $120° \pm 3°$. It is important to mention that other hydrophobized surfaces like PFOTS and PDMS were tested, but they mostly lead to partial, non-vertical rebounds. This makes measuring the deflection of drops by external electric fields hard or impossible. Hence, Teflon was the best hydrophobic surface for charging of bouncing drops.

4.1.2 SU-8 micropillar arrays surfaces

4.1.2.1 Sample preparation

75 x 25 mm^2 rectangular glass slides of 1 mm thick were used as substrates. Acetone was used to perform two steps of sonication for 15 minutes to remove organic impurities. Next, 2-propanol was used to remove the acetone's contaminated residues for another 15 minutes. Afterwards, substrates were dry blown using a filtering nitrogen gun. 1 mL of SU-8 photoresist was then dropped onto the clean glass. The process involved a two-stage spin coating procedure (step 1: 5 s, 500 rpm, with 200 $rpms^{-1}$ acceleration, and step 2: 30 s, 3000 rpm, with 200 rpm^{-1} acceleration). In order to prevent the production of bubbles, the samples of SU-8 were put into vacuum for degassing. The samples were put then on a hotplate to carry out the soft baking process for 70 minutes at a temperature between 65° and 95°. After the sample was cooled down at room temperature, a photomask was placed on top of it, and it was then subjected to I-line UV light (290 J/cm^2 and 350-400 nm wavelength) for 8 seconds. The photomask had rectangular holes of 10×5 μm squared, spaced 20 μm. Post-exposure baking for up to 1-2 minutes at 95° was performed to thermally activate a cationic polymerization. Subsequently, samples were then rinsed with 2-propanol for 1 minute and developed with the SU-8 developer for 3 minutes. As a result, the non-illuminated part of the photoresist was removed and rectangular micropillars with a spacing of 20 μm (between the edges) and a height of 10 μm were

formed on the surface, as shown by scanning electron microscopy (Fig. 4.1c).

4.1.2.2 Wetting properties

Surfaces showed a static contact angle of θ_s =133° ± 3° and a contact angle hysteresis of 20° ± 2°. According to these contact angles values, micropillar surfaces behave almost like superhydrophobic surfaces, but as their static contact angle is below 150 deg and contact angle hysteresis is above 10 deg, they are not really superhydrophobic. In fact, for impact heights in the range of 0.5 to 3 cm, drops showed complete rebounds (Fig. 4.1d). Therefore, in this range of heights, drops exhibit Cassie-Baxter state when they hit a micropillar surface.

4.2 Drop impact dynamics of Teflon AF

In this section, I will present and describe some important aspects of the drop impact dynamics on Teflon surfaces. This will serve as a key point to analyze charging and evidence the presence of self-generated electrostatic forces.

4.2.0.1 Spreading Parameter and contact area

The spreading parameter R_{max}/R_0 was calculated for Teflon surfaces at different We. For these surfaces, when $We > 10$, the maximum spreading radius scales as $R_{max} \sim R_0 We^{0.3}$, which is slightly different in comparison with superhydrophobic surfaces, where a scaling of $R_{max} \sim R_0 We^{0.25}$ was found in chapter 2. For an ideal case with complete conservation of energy, one would expect a scaling of $R_{max} \sim R_0 We^{1/2}$ (Section 1.5.6). This means that during the impact on hydrophobic surfaces part of the initial impact energy is dissipated and the dissipation is different compared to superhydrophobic surfaces, which will be discussed in the following sections.

The scaling law found for the spreading parameter of Teflon AF can be also written in terms of A_{max}:

$$A_{max} = \pi R_0^2 We^{0.6} \tag{4.1}$$

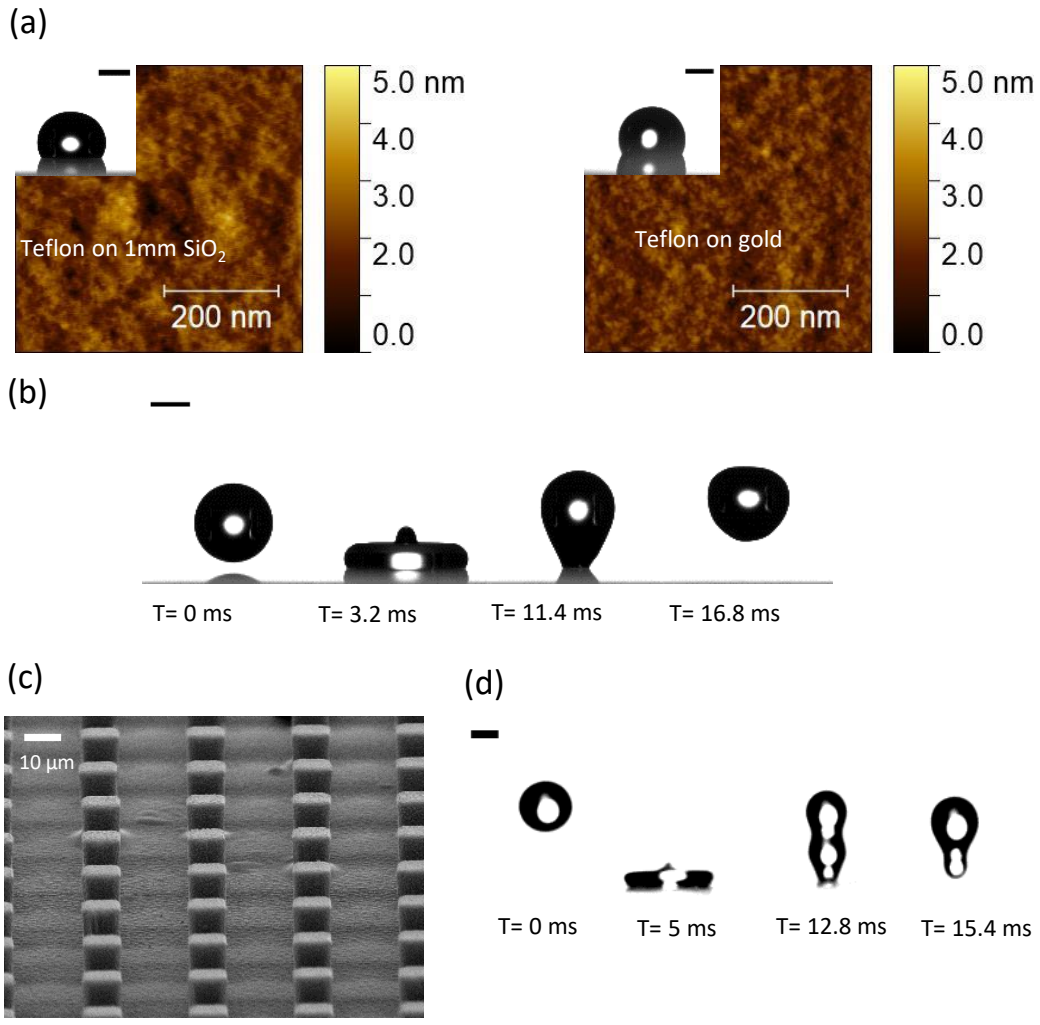

Figure 4.1: (a) Scanning force microscopy image of Teflon on SiO_2 (left) and on gold (right). Insets show water drops deposited on the surface. (b) Drop rebounding from Teflon-SiO_2. Error bars represents 1 mm. (c) Scanning electron microscopy image of SU-micropillar array surface. (d) Drop rebounding from a SU-8 micropillar array surface.

In this case, A_{max} really represents the effective contact area, since drops remain in the Wenzel state during the impact. Therefore, a more pronounced spontaneous charging is expected on these surfaces upon drop impact.

The setup configuration was the same as described in section 2.1. Note that the applied electric fields are up to 100 kV/m. Since the adhesion forces are stronger on hydrophobic surfaces, drops will rebound to a lower height, leaving less time for the electric field to accelerate drops. Increasing the electric field ensures a measurable deflection of charged drops.

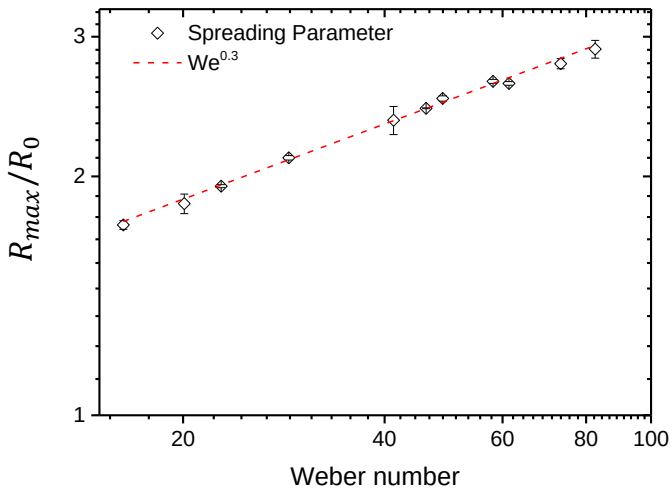

Figure 4.2: Spreading parameter R_{max}/R_0 vs. Weber number for a Teflon on SiO_2 surface

4.3 Charging on Teflon-SiO_2

4.3.1 Drop impact conditions

In the same way than the experiments for superhydrophobic surfaces, water drops were dispensed from different heights while a lateral electric field was applied. The following impact conditions were used:

- Drop Volume: 4μL
- Electric field: $E = U/d = 50 - 100$ kV/m
- Weber number: $We = 10 - 83$
- impact speed: $v_0 = 1 - 1.7$ m/s

4.3.1.1 Deflection of drops

When drops rebound off from Teflon-SiO_2, they eject a secondary drop or jet from the top when $We > 20$. This jet is called the Worthington jet [38], and generated due to the collapse of an air cavity in the center of the deformed drop (denoted primary drop). Below $We = 40$, rebound heights are too low to detect

a significant deflection of drops. This sets the limit of our electric field method for hydrophobic surfaces. For $We > 40$, both primary and secondary drops deflect laterally in the direction of the electric field (Fig. 4.3). Therefore, all drops charge spontaneously with positive charge upon impact on Teflon-SiO_2.

As We increases, the lateral deflection of drops is more pronounced. Furthermore, our higher range of We implies more pronounced deformation of drops compared to the experiments on superhydrophobic surfaces. Therefore, it is instructive to estimate the influence of the drag force on the drop motion in air. Taking a drag coefficient of $C_D = 1$, and a typical cross sectional area of $A \sim 28\ \mu m^2$, a drag force of $F_D = 0.042\ \mu N$ is obtained, which is completely negligible in comparison electrostatic forces acting on charged drops rebounding from superhydrophobic surfaces ($F_E > 2\mu N$). Thus, charge values can be safely calculated from the drop mass centre trajectory.

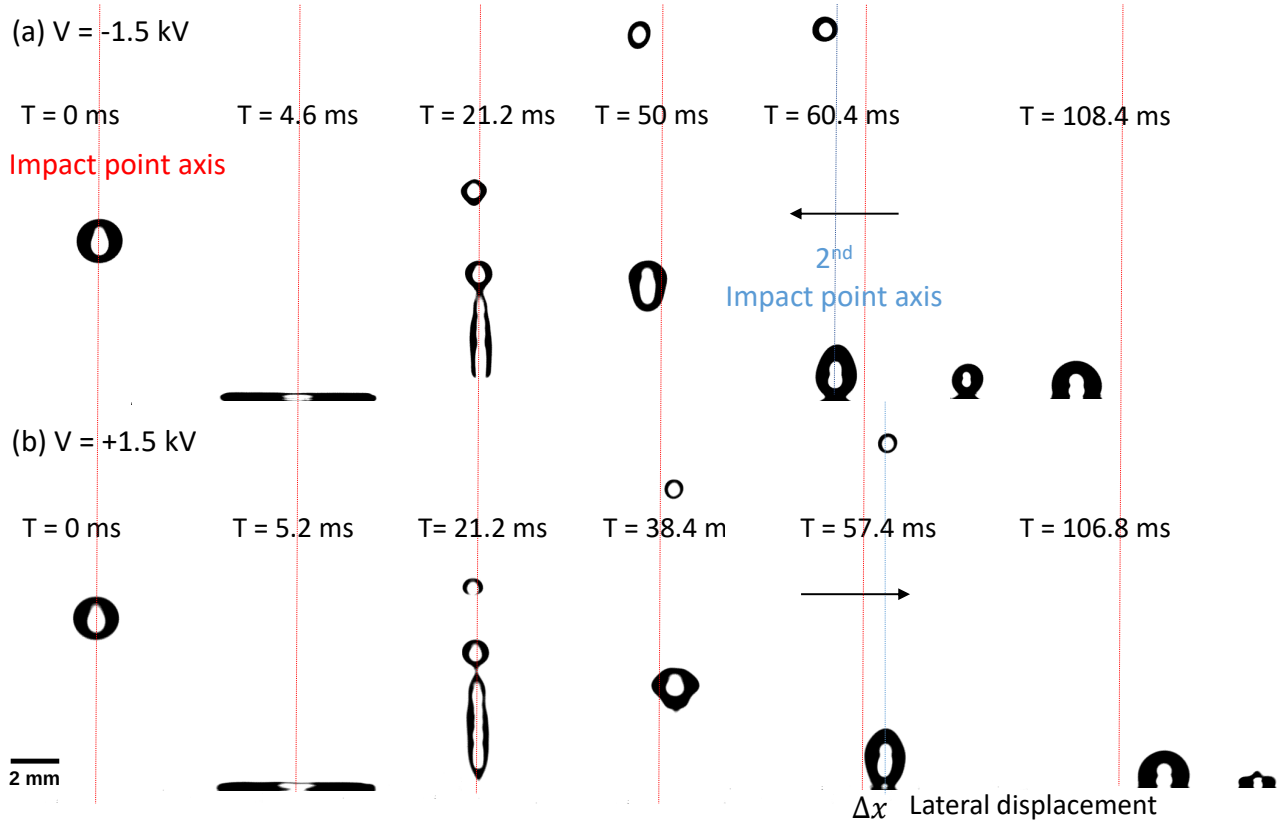

Figure 4.3: (a) 4 μL drop impacting a Teflon on SiO_2 surface while an electric field from right to left is applied. (b) Same drop impact experiment than (a), but with the electric field from left to right. Drops rebound in the direction of the electric field.

4.3.1.2 Characterization of secondary drops

The ejection of secondary drops definitely leads to a loss in drop volume. In addition, since both primary and secondary drops can acquire positive charge, it is necessary to know precisely the ejected amount of volume for the drop charge calculation (eq. 2.4).

As mentioned in section 3.4, volume of jets were calculated assuming a spheroidal shape (Fig 4.4). Our calculations indicate that the initial impacting drop can break up losing a volume between 0.35 and 1.55 μL (Fig 4.5a), which is actually up to $\sim 40\%$ of the initial drop volume. Increasing We not necessarily leads to an increase in the ejected drop volume. All the drops detach from the primary drop with speeds up to 1 m/s. Our range of We is not sufficient to allow splashing, which would not be convenient for the electric field method approach, given the high-speed and number of secondary drops in that case.

From the drop charge calculations, jets exhibited charge values up to 70 pC, even higher than 4 μL drop rebounding from a superhydrophobic surface. The amount of charge tends to increase with increasing jet volume (Fig 4.5b), since more capacitance is available to store charge.

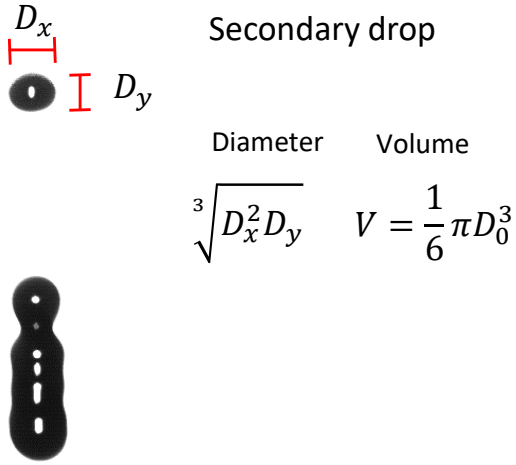

Figure 4.4: Calculation of the volume for a secondary drop ejected from a drop bouncing on Teflon-SiO_2.

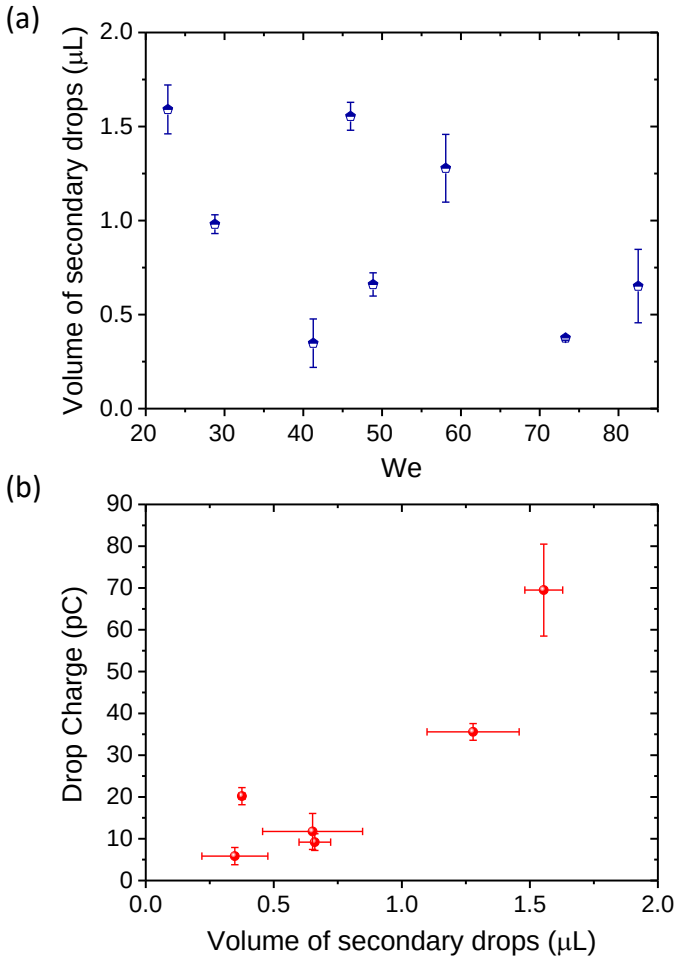

Figure 4.5: (a) Volume of secondary drops as a function of Weber number. (b) Drop charge vs. volume of secondary drops.

4.3.1.3 Charge as a function of Weber number

In the previous chapter, I demonstrated that A_{max} is the controlling parameter in drop charging. This means that drop charge can be also represented in terms of We. Replacing eqn. 4.1 into eqn. 3.12 leads to:

$$Q(We) = -2\pi\sigma_S^0\lambda_r^2\left[1 - \exp\left(\frac{-\pi R_0^2(We^{0.6} - We_0^{0.6})}{2\pi\lambda_r^2}\right)\right], \qquad (4.2)$$

where We_0 is the minimum Weber number at which a rebound is possible. The advantage of the expression is that only knowing the characteristic parameters of the surface and the release height, the charge can be estimated. In cases when the magnification and contrast of high-speed videos are not suffi-

cient to determine precisely R_{max}, eqn 4.2 would be an excellent approach for drop charge prediction. For our case, R_{max} can be well resolved and therefore A_{max} at different We (Fig. 4.6a).

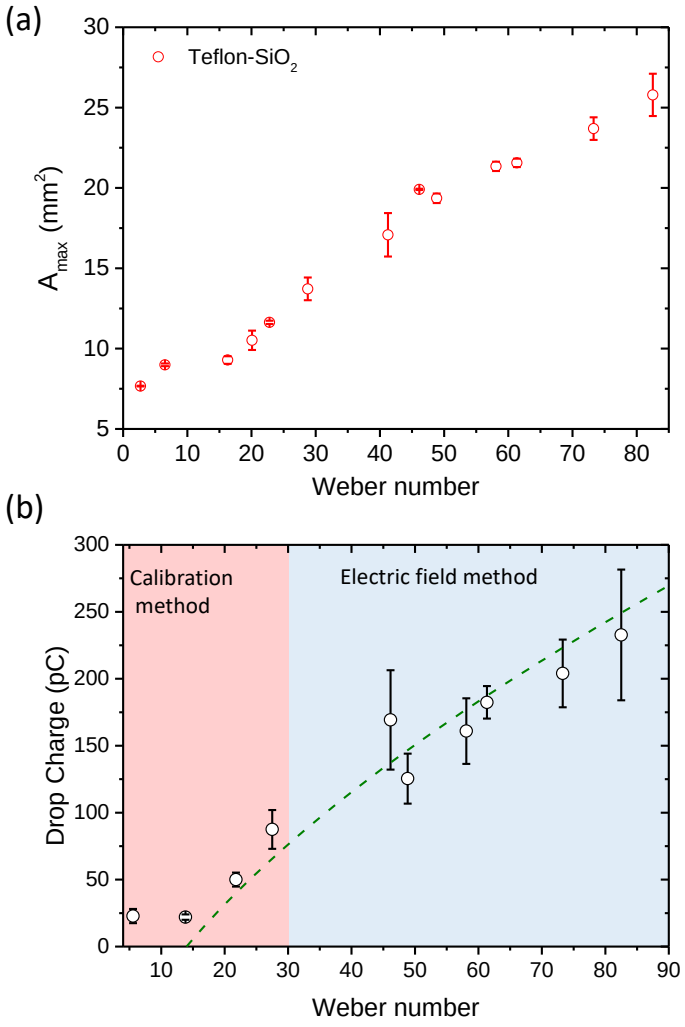

Figure 4.6: (a) Maximum contact area as a function of Weber number for drops impacting on Teflon on SiO_2. (b) Drop charge vs. Weber number of the same drops in (a). The red shaded region contains the data obtained by the calibration method, whereas the blue shaded region the data obtained from the electric field method. The green dashed line represents the theoretical prediction with the following fitting parameters: $\sigma_S^0 = 8.6\ \mu\text{C/m}^2$ and $\lambda_r = 32$ mm

To calculate the total charge using the electric field method, the primary drop charge plus the secondary drop charge were considered. Since our electric field method is limited when $We < 20$, the calibration method described previously in section 2.1.3 was used to determine the charge in that range. The results showed an increase of drop charge with increasing We (Fig. 4.6b), with values

more than five times the charge of drops rebounding from superhydrophobic surfaces. This clearly demonstrates the larger real solid-liquid contact area for hydrophobic surfaces compared to superhydrophobic surfaces.

The calibration method also serves to identify at which We the charge reaches its lowest value. The minimum charge is reached from $We = 14$. For $We < 5$, drops do not rebound and charging is undetectable by the wire. Accordingly, $We_0 = 14$ was selected as the moment of the minimum possible charge. Fitting eqn. 4.2 leads to the following independent parameters: $\sigma_S^0 = 8.6$ μC/m^2 and $\lambda_r = 32$ mm. These values are in quite good agreement with the values found for the same surfaces in the case of slide electrification [96]. This means that by using the electric field method, σ_S^0 and λ_r can be obtained with comparable accuracy. Note that λ_r on Teflon is higher than on SN, as the drops are able to deposit more charge on the surface due to the larger effective solid-liquid interface, which at the same time increases the charge saturation point.

4.3.1.4 Calibration method

To verify the reliability of our measurements with the electric field method, calibration experiments were performed above $We > 40$. Both, experimental and calibration values are in good agreement, which ratifies the electric field method as a precise tool for drop charge detection.

Although the calibration method arises as a precise method for drop charge detection, it is quite challenging to catch secondary drops with the tungsten wire when jetting takes place. Consequently, if some drops are not detected, part of the total charge is not measured, leading to uncertainties.

4.3.2 Charging for Teflon on Gold substrates

Surprisingly, drops rebounding from Teflon on gold did not show any significant deflection by the electric field. This means that charge separation does not occur or it is too weak to be be detected by our method. Li et al. [96] previously

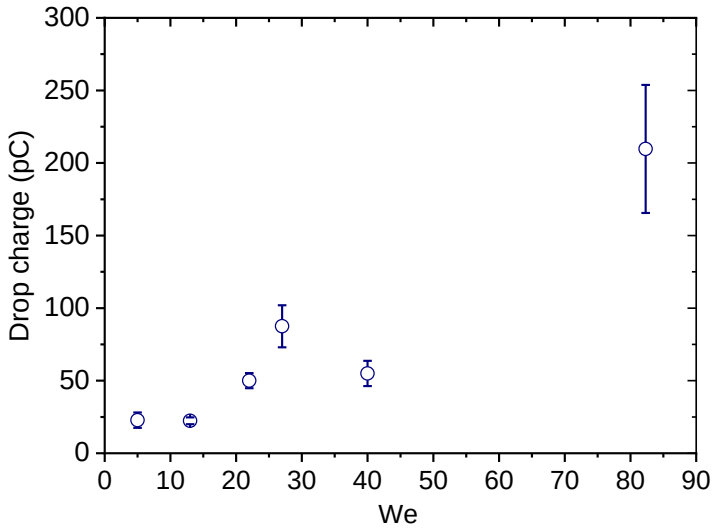

Figure 4.7: Charge calculated from the current signals detected by the wire probe in contact with rebounding drops.

reported for sliding drops a decrease in drop charge for Teflon on gold, with charges 10 times lower than for Teflon on SiO_2.

It is not yet understood why the presence of an highly conductive layer below that Teflon film suppresses substantially the charge separation. One possibility would be that gold can act as a conductor and discharges the drop through the thin (60 nm) Teflon layer. In other words, charge separation may still occur, but charges are not kept within the drop. Nevertheless, this has not been proved so far and requires further study. The consequences of the metallic sublayer for the drop impact dynamics will be discussed in the following sections.

4.3.3 Evidence of self-generated electrostatic forces

As charging can affect the drop motion of sliding drops for Teflon on SiO_2 for the case of slide electrification, it is plausible to expect a similar effect when drop impact occurs. In this section, I will show that the spontaneous charging of drops impacting on Teflon on SiO_2 induces the generation of electrostatic forces that influence the retraction dynamics and drop motion after rebound.

The phenomenon reported here serves as a new approach to describe the drop motion in terms of charging and other sources of energy.

4.3.3.1 1^{st} Indicator: Retardation of retraction motion

The first indicator of the existence of electrostatic force between the drop and surface is the retraction phase. Measuring the average spreading speed $\overline{V}_s$ at different We for Teflon surfaces reveals that, drops spread similarly on both SiO_2 and gold (Fig. 4.8a). However, the average retraction speed $\overline{V}_{ret}$ is higher on Teflon on gold, which is the surface where charging was not detected (Fig. 4.8b). As the Teflon surfaces have similar wetting properties and roughness, the charging should be the only explanation for the difference in the retraction motion. Hence, two important conclusions can be drawn from this fact. First, the average spreading speed $\overline{V}_s$ remains invariable for each type of substrate, which means that charge separation does not take place in the spreading phase, but in the retraction phase. Secondly, the retardation of the retraction motion suggests the existence of electrostatic forces that counteract the receding motion due to the charges left on the surface.

As the retraction dynamics confirm our assumption of a disrupted EDL during retraction, the process of charging and subsequent emerging of electrostatic forces is:

- After the impact, the drop spreads on the surface and a EDL is formed immediately (Fig. 4.8c), in a timescale of a few μs. According this time scale, the spreading phase is the only moment where the EDL should form.
- The process of formation of an EDL is as follows: The hydrophobic coating will tend to absorb hydroxyl ions from water to form a negative layer on the surface. Counterions in water, such as H_3O^+ or H^+ will be part of the Stern and diffuse layer to screen the surface charges. According the similarities in $\overline{V}_s$ for Teflon surfaces, charges at the solid-liquid interface do not affect the spreading dynamics.
- When the drop starts to retract, the electrical equilibrium of the EDL is broken and negative charges are left on the solid surface. These charges will generate attractive electrostatic forces to the positive retracting drop,

specifically, at the rim (Fig. 4.8d). Consequently, an electrostatic force is acting on the the drop rim in hte outward direction, oppositely to the direction of the retraction motion, which definitively slows down the drop recoil.

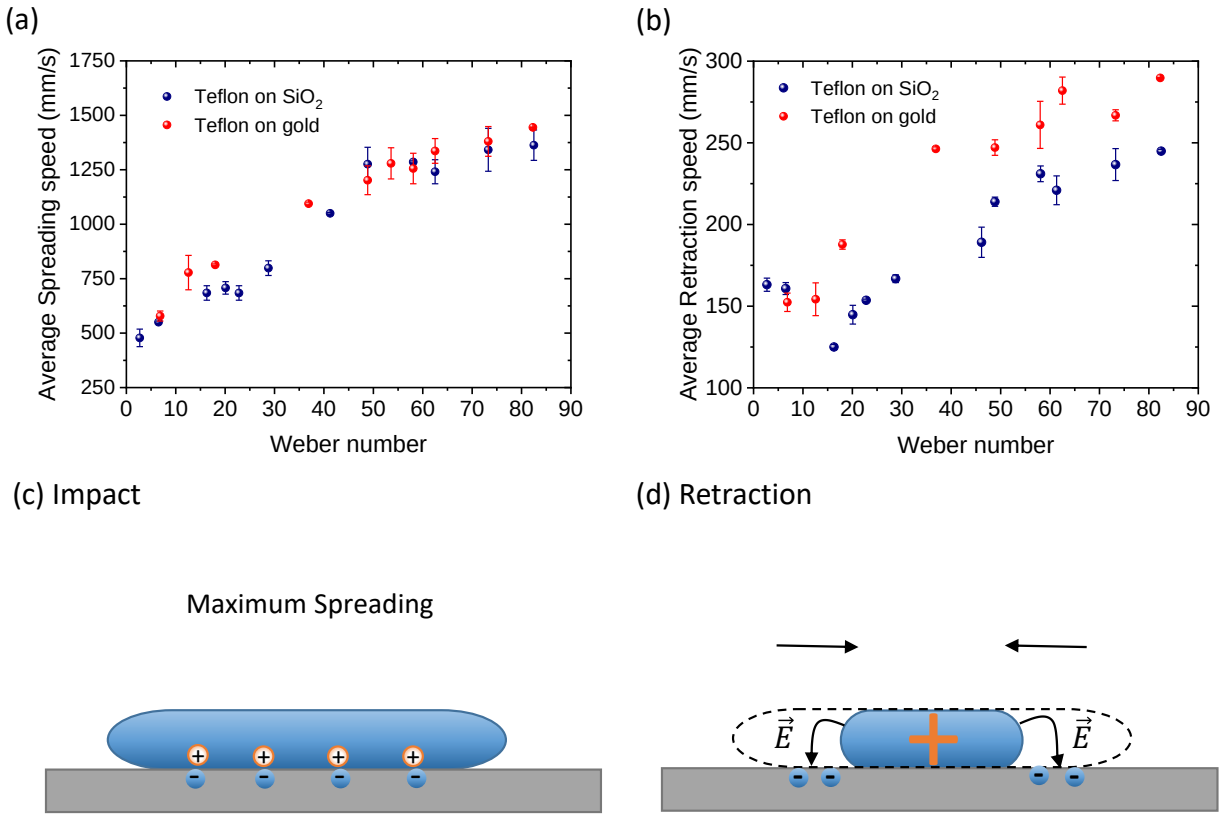

Figure 4.8: (a) Average retraction speed and (b) spreading speed vs. Weber number of drops rebounding from Teflon on SiO_2 and on gold. (c) Schematic of a drop reaching the maximum spreading radius. The EDL is formed at the solid-liquid interface. (d) Schematic of the retraction motion of a drop while the negative charges left on the surface exert an attractive electrostatic force at the drop rim.

4.3.3.2 Calculation of the average electrostatic force

In this section, I will calculate the average electrostatic force that delays the drop recoil, by using an energy balance approach. Firstly, I start with the case of Teflon on gold, where charging is negligible. At the moment of the impact, the total energy E_T of the drop is given by the kinetic energy:

$$E_k = \frac{1}{2} m v_0^2, \tag{4.3}$$

which is actually the same energy as the gravitational potential energy when the drop is coming out from the syringe:

$$E_p = mgh \tag{4.4}$$

After the impact, the kinetic energy is converted to surface energy as the drop spreads on the surface until reaching R_{max}. Afterwards, the drop retracts due to the surface tension forces and now the surface energy is converted back to kinetic energy until the take off. At this point, the energy can be expressed as follows:

$$E_R = \frac{1}{2} m_p v_p^2 + \frac{1}{2} m_s v_s^2 + m_p g h_p + m_s g h_s, \tag{4.5}$$

where the indexes "p" and "s" represent the primary and secondary drop, respectively. E_R is given basically by the kinetic and potential energies of all the drops observed after rebound. The total energy E_T does not conserve because is partially lost in form of viscous dissipation E_V and friction E_F, so that the loss in energy is simply given by

$$E_T - E_R = E_V + E_F \tag{4.6}$$

Now, this energy balance should be extended to the case of charging, that is, when drops rebound from Teflon on SiO_2. In this case, the electric energy should be added to eqn. 4.11. Thus, the energy after rebound for Teflon on SiO_2 is:

$$E_R = \frac{1}{2} m_p v_p^2 + \frac{1}{2} m_s v_s^2 + m_p g h_p + m_s g h_s + \frac{Q_p^2}{4\pi\epsilon_0 h_1 p} + \frac{Q_s^2}{4\pi\epsilon_0 h_1 s} + \frac{Q_p Q_s}{4\pi\epsilon_0 (h_1 p - h_1 s)}. \tag{4.7}$$

$$E_T - E_R = E_V + E_F + E_{ef}, \tag{4.8}$$

where E_{ef} represents the absolute value of the work done by the electrostatic force during retraction. In order to calculate E_F, it is necessary to integrate the friction force in the advancing (f_a) and receding phase (f_r) of the contact line (eqn. 1.9), from 0 to R_{max} [70]:

$$E_F = 2\pi\gamma \int_0^{R_{max}} f_a \; r dr + 2\pi\gamma \int_0^{R_{max}} f_r \; r dr = \pi\gamma R_{max}^2 (\cos\theta_r - \cos\theta_a). \tag{4.9}$$

All the parameters in eqn. 4.9 are available from our measurements to calculate E_F. Hence, E_V can be easily calculated by $E_T - E_R - E_F$. For the case of Teflon on SiO_2, viscous dissipation is more complicated to estimate, because the contribution of E_{ef} is not known. The viscous dissipation E_V of a impacting drop is a result of the shear stress in a thin boundary layer close to the solid-liquid interface [97, 98] and can be estimated by the expression [70]:

$$E_V = E_{V-S} + E_{V-R} \approx \frac{\mu B v_0^2 \tau_s R_{max}^2}{L_V} + \frac{\mu B v_0^2 \tau_r R_{max}^2}{L_V}. \tag{4.10}$$

Here, E_V results from the contribution of the viscous dissipation during spreading (E_{V-S}) and retraction drop motion (E_{V-R}). L_v is the characteristic length scale and B another constant. The impact speed v_0 represents the characteristic speed of the thin boundary layer. In the same way as for superhydrophobic surfaces, τ_s and τ_r are respectively, the spreading and retraction times of drops impacting on Teflon surfaces. Using the definition of the average spreading and retraction speed, eqn. 4.10 can be rewritten as follows:

$$E_V = E_{V-S} + E_{V-R} \approx \alpha(\tau_s^3 \overline{\mathrm{V}}_s^2 + \tau_r^3 \overline{\mathrm{V}}_r^2), \tag{4.11}$$

where $\alpha = \mu B v_0^2 / L_v$. At the spreading phase, $\overline{\mathrm{V}}_s$ and τ_s (Fig. 4.9a) are practically identical for both Teflon substrates when $We > 40$. Accordingly, these surfaces at the same v_0 (or We) should dissipate the same energy E_{V-S}. For

the case of the retraction motion, $\overline{V}_r$ changes with We due to the variation of t_r. In fact, R_{max} varies with We in the same manner for each substrate due to the same wetting properties. At the same We, t_r is up to 18% higher for Teflon on SiO_2 than for Teflon on gold (Fig. 4.9b), whereas $\overline{V}_r$ is up to 20% lower. As a result, there is a maximum difference of up to 5% in the values of E_{V-R} for the different Teflon surfaces, so that their values of E_V can be considered identical. This means that E_V can be directly estimated from the energy balance for Teflon on gold. Eqn. 4.11 is not suitable to estimate E_V because the parameters B and L_v are unknown in our range of We.

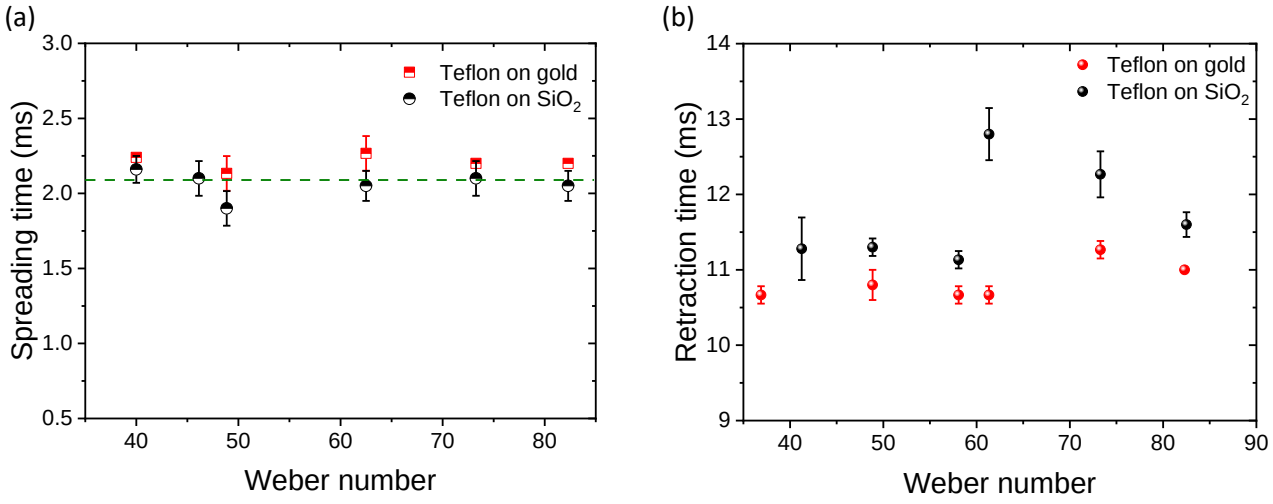

Figure 4.9: Spreading (a) and retraction time (b) as a function of Weber number for drops rebounding from Teflon on SiO_2 and on gold.

Our calculations indicate that E_V increases with increasing We (Fig. 4.10a). This occurs due to the dissipation of the total initial kinetic energy in form of internal flow [80, 99] and the shear within a boundary layer near the surface [100, 101]. E_F should also exhibit an increment as We increases, due to the increasing R_{max}. However, the variation of R_{max} (less than 0.9 mm) is not sufficient to evidence a significant change in E_F.

The values of E_{ef} are comparable with E_F, which implies that the influence of electrostatic forces in the drop motion exists. In fact, it is possible to determine the average electrostatic force acting during the entire retraction phase. Since E_ef is the work exerted by the electrostatic forces, the average electrostatic

force acting at the drop rim a distance $D_{max} = 2R_{max}$ is:

$$F_{ef} = \frac{E_{ef}}{D_{max}} \tag{4.12}$$

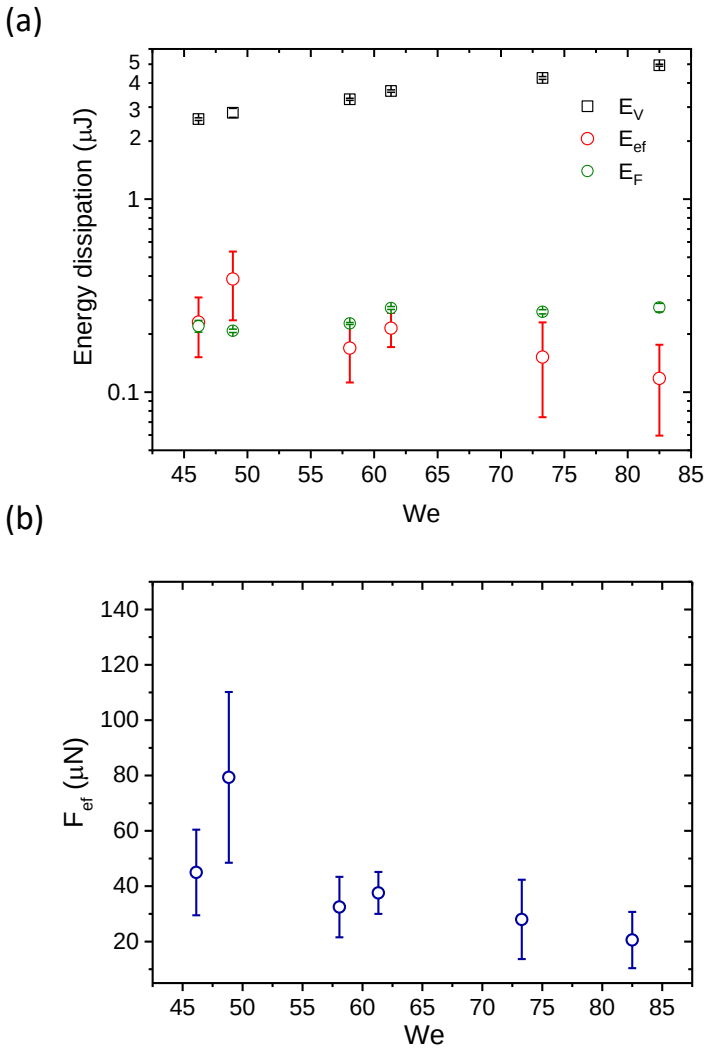

Figure 4.10: (a) Sources of energy dissipation as a function of Weber number.(b) Average electrostatic force during the retraction motion as a function of Weber number.

The order of magnitude of F_{ef} (Fig. 4.10b) coincides with the electrostatic forces reported by Li et. al, for the case of slide electrification on the same surfaces [96]. Furthermore, forces tend to remain constant when varying We, which is unexpected. Further spreading due to an increment of We would lead to more charge deposited on the surface, increasing the attractive electrostatic forces at the drop rim. However, the increase of the deposited charge is com-

pensated by the retracting radius that becomes larger the higher the impact energy is. Thus, F_{ef} is independent of We.

The retardation of the retraction motion by the electrostatic forces will definitely lead to more energy dissipation on Teflon on SiO_2. In fact, drops rebound off of Teflon on gold, with a takeoff speed higher than for Teflon on SiO_2. As a consequence, the energy after rebound can be up to $\pm 30\%$ higher on Teflon on gold as shown in Fig. 4.11.

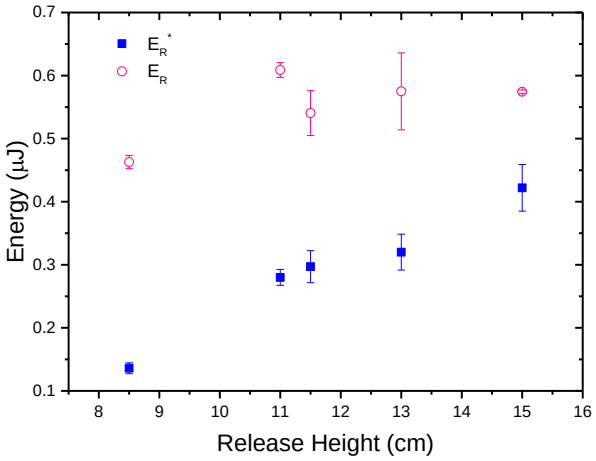

Figure 4.11: Energy of a rebounding drop at the moment of rebound, as a function of the release height.

4.3.3.3 2^{nd} Indicator: Reduction of the maximum rebound height

After rebounding from the surface, drops move vertically upwards until reaching a maximum height due to the opposition of gravity. Since electrostatic forces can affect the retraction dynamics of drops, could theses forces influence the rebounding motion as well? This is a logic question, considering that, if drops do not saturate during retraction, the maximum charge will be reached when drops rebound from the surface (eqn 3.11).

The high-speed videos showed that drops rebound higher on Teflon on gold than on Teflon on SiO_2 (Fig. 4.12a). In particular, drops can reduce the max-

imum rebound height up to more than 50% when charging effects take place. Definitively, the electrostatic forces will decrease the takeoff speed of drops rebounding from Teflon on SiO_2. Is this decrease sufficient to set the difference in the maximum rebound heights between Teflon surfaces? Based on the measured takeoff speeds, primary drops should rebound higher than the observed heights for Teflon on SiO_2. For instance, at $We = 82$, a primary drop rebounds with a vertical speed of $v_p = 0.42$ m/s, which leads to an expected height of $h = v_p^2/2g = 8.8$ mm. However, experimentally, $h \sim 6$ mm$\pm$1 mm. Thus, the gravity force is not the only force counteracting the upward drop motion after rebound, so that electrostatic forces should be taken into account.

How does the reduction of the rebound height occur? Negative charges are deposited progressively on the surface as the drop retracts. Subsequently, these charges after rebound will exert an average attractive electrostatic force on the drop that is acting downwards. This can be understood considering a positive net charge located in the drop mass center and a negative net charge on the surface (Fig. 4.12a). Hence, the deceleration of drops is more pronounced at the first moments after rebound, where the distance between the drop mass center and the surface is in the order of ~ 2 mm.

Does the viscous dissipation in air influence the drop motion? Our range of We involves a large deformation of drops after rebound, which could lead to an important viscous dissipation. This may also affect the maximum rebound height reached by drops. Nevertheless, there is one reason of why the viscous dissipation in air can be considered not significant. If viscous dissipation were the main source for the energy loss, then the drops would rebound reaching the same height for Teflon on gold and on SiO_2, which experimentally is not the case. This means that electrostatic forces are the dominant factor that decelerates the upward motion of drops.

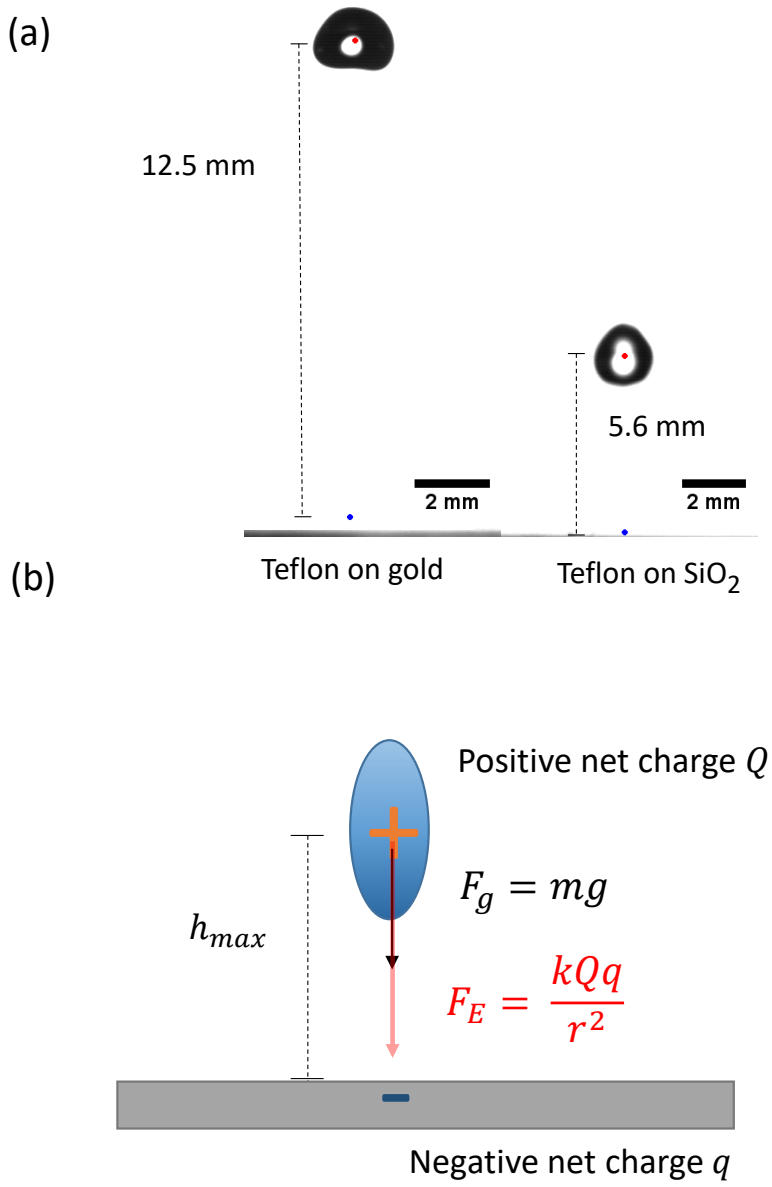

Figure 4.12: (a) Drops reaching the maximum rebound height for a Teflon on gold and on SiO_2. Red points represent the position of the drop mass center when the drop reaches the maximum rebounding height. Blue points the position of the surface (b) Drop charge vs. Volume of secondary drops. Schematic of the electrostatic force acting on a rebounding drop.

Restitution coefficient The low permittivity substrates like SiO_2 certainly dissipate more energy of an impacting drop due to the electrostatic forces. One way to characterize the energy dissipation is the restitution coefficient. Using eqn. 1.16, the restitution coefficient for Teflon surfaces were calculated. The calculations indicate that restitution coefficient values can be decreased up to

45% because of charging effects, when Teflon on SiO_2 is used (Fig. 4.13). This is an interesting result from a viewpoint of surface characterization. Self-cleaning properties of hydrophobic surfaces consider the capability of removing water drops. If drops spontaneously charge, then the electrostatic effects will hinder the self-cleaning of the surface, both by sliding or bouncing.

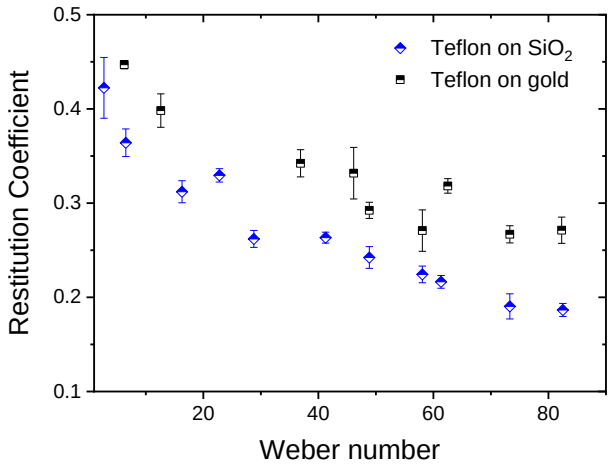

Figure 4.13: Restitution coefficient of Teflon on SiO_2 and on gold vs. Weber number.

4.3.4 Calculation of the average electrostatic force after rebound

In order to calculate the average electrostatic force that pulls down the primary drop after rebound, I used again an energy balance approach. The position of the drop mass center serves to determine the kinetic and gravitational potential energy in two situations: After rebound and when the maximum rebound height is reached.

At the moment when the drop detaches from the surface, the total energy of the primary drop is given by its kinetic energy E_k, the gravitational potential energy E_{p_1} and the electric energy of the drop E_{Q1p} due to the electrostatic interaction with the surface. This should be equivalent to the total energy at the maximum rebound height h_{max}, which is the sum of the gravitational potential energy E_{p_2}, the electric energy of the drop E_{Q2p} due to the interaction with the surface and the absolute value of the energy dissipated by the electrostatic forces E_{FE}:

$$E_T = E_k + E_{p_1} + E_{Q1p} = E_{p_2} + E_{Q2p} + |E_{F_E}| \tag{4.13}$$

$$<=> E_T = \frac{1}{2}mv_{1p}^2 + mgh_{1p} + \frac{Q_p^2}{4\pi\epsilon_0 h_{1p}} = mgh_{max} + \frac{Q_p^2}{4\pi\epsilon_0 h_{max}} + |E_{F_E}| \tag{4.14}$$

Therefore, E_{FE} can be expressed as follows:

$$|E_{F_E}| = \frac{1}{2}mv_{1p}^2 - mg(h_{max} - h_{p1}) + \frac{Q_p^2}{4\pi\epsilon_0}\frac{(h_{max} - h_{p1})}{h_{max}h_{p1}} \tag{4.15}$$

The average electrostatic force after rebound would be then:

$$F_E(h_{max} - h_{p1}) = |E_{F_E}| \tag{4.16}$$

where $(h_{max} - h_{p1})$ is the distance at which the work of the electrostatic force was done. This leads to the following expression for F_E:

$$F_E = \frac{mv_{1p}^2}{2(h_{max} - h_{1p})} - mg + \frac{Q_p^2}{4\pi\epsilon_0 h_{1p} h_{max}}, \tag{4.17}$$

From eqn. 4.17, electrostatic forces after rebound were calculated, with values even higher than the gravitational force (Fig. 4.14). This means that these forces are high enough to affect the drop motion considerably. Similarly with the retraction phase, the average electrostatic forces after rebound are weakly affected by varying We. This can be explained by the dependence of the electrostatic forces with distance (rebound height) and drop charge and the dependence of drop charge with We. The electrostatic force will be greater as larger the drop charge and shorter the distance to the surface. When a drop rebounds, the electrostatic force reaches its maximum value. Then, the force decreases with the distance to the surface until the drop is at its maximum height h_{max}. Now, increasing We will lead to an increment of the drop charge and h_{max}. Both increments compensate each other, which keeps F_E mostly unaltered.

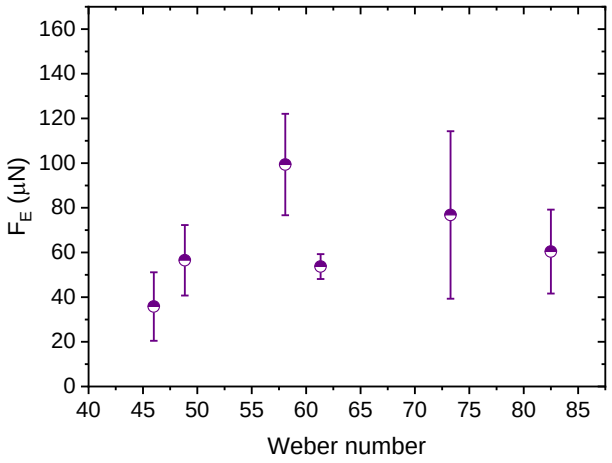

Figure 4.14: Average electrostatic force as a function of Weber number after a drop rebounds from Teflon on SiO_2.

4.3.5 Prediction of Drop charge

So far, I have derived a theoretical model compatible with experimental results to reasonably estimate the charge of bouncing drops at certain We or A_{max}. This is actually quite convenient when the parameters λ_r and σ_S^0 are known for a specific surface. However, these parameters can be determined mainly as fitting parameters resulting from measurements using current/voltage amplifiers or, in our case, electric fields. A simple alternative approach to estimate the drop charge would be the use of high-speed video processing. Since electrostatic forces affect the energy balance of a rebounding drop, the tracking of the position of the drop mass centre becomes crucial. Indeed, the position of the drop mass centre determines the gravitational energy and electric energy, whereas its time derivative allows calculation of the kinetic energy.

By Coulomb's Law, the average electrostatic force derived from our experiments can be represented as follows:

$$F_E = \frac{kQq}{r^2} = \frac{kQ^2}{(h_{max} - h_{p_1})^2}, \tag{4.18}$$

Here Q is the drop charge and q the surface charge. k is the Coulomb

constant. Assuming that drops gain an amount of positive charge equivalent to the total charge deposited on the surface, then $q = Q$. In addition, r represents the distance at which drops experience the work done by F_E, until reaching h_{max}. Hence, $|E_{F_E}|$ can also be understood as the average electric energy of a rebounding drop that moves vertically a distance r, and it can be expressed as $|E_{F_E}| = F_E\ r = kQ^2/r$. Eqn. 4.14 then yields:

$$\frac{1}{2}mv_{1p}^2 - (h_{max} - h_{1p})mg = \frac{Q^2}{4\pi\epsilon_0}\left[\frac{1}{r} + \frac{1}{h_{max}} - \frac{1}{h_{1p}}\right] \tag{4.19}$$

As a result, the charge can be estimated by:

$$Q = \sqrt{\beta^{-1}\left[\frac{1}{2}mv_{1p}^2 - mg(h_{max} - h_{1p})\right]}, \tag{4.20}$$

with

$$\beta = \frac{1}{4\pi\epsilon_0}\left[\frac{1}{(h_{max} - h_{1p})} + \frac{1}{h_{max}} - \frac{1}{h_{1p}}\right] \tag{4.21}$$

It is important to mention that, by definition r should be separation distance between two charged objects. However, in our case the average electrostatic forces were obtained based on an energy balance dependent on the vertical distance covered by the drop, from takeoff until the upward motion stops. The charge predicted by eqn. 4.20 is in good agreement with charges measured by the electric field method. Thus, drop charge can be predicted from an energy balance approach, by only knowing the position of the drop mass center over time.

The precision of the charge prediction is remarkable, because it implies that drop charge can be estimated simply from high-speed video imaging, without electric fields or other electronic devices for charge detection. However, this estimation of the charge will work for situations where electrostatic forces are significant. Drops rebounding from superhydrophobic surfaces acquire up to five times lower charge, which means that the influence of electrostatic forces on the drop motion would hardly be detectable from high-speed videos. Besides, analyzing the influence of electrostatic forces in the drop impact dynamics requires

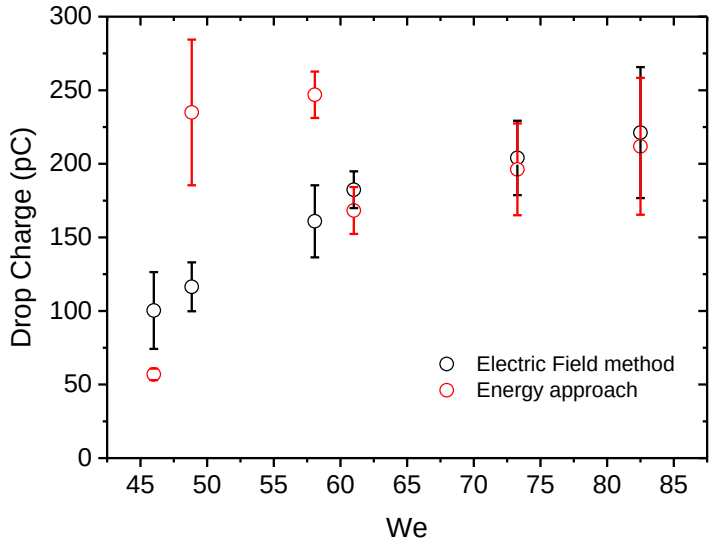

Figure 4.15: Charge calculated by energy balance of rebounding drops and by the electric field method, as a function of Weber number. Both methods are in good agreement.

the synthesis of nanofilaments on high permittivity substrates like aluminum or gold. Such type of coating cannot grow properly on these surfaces, as the resulting surfaces exhibit hydrophilic spots that suppress rebound of impacting drops.

4.4 SU-8 Micropillar arrays surfaces

I have already demonstrated in previous sections the relevant influence of the effective contact area, i.e. the real liquid-solid contact area between drop and substrate, in the charge separation process. For the case of Teflon on SiO_2, the surface is smooth and flat, which means the effective contact area can be directly extracted from the video images of drop spreading. Nonetheless, for a superhydrophobic surface is only possible to determine experimentally an apparent contact area due to the Cassie wetting state of drops. In this section, I will add further evidence about the contact area as controlling parameter in the drop charging, by performing drop impact experiments on SU-Micropillars sur-

faces. Water drops were released at different We, and the charge was calculated by using the electric field method.

Why micropillar surfaces? Micropillar surfaces are especially suitable as model surface whose effective contact area is well defined, due to the defined size and shape of the pillars. These surfaces were prepared in such a way that they have contact angles corresponding to hydrophobic surfaces, but they can behave like a superhydrophobic surface. As drops remain in the Cassie state during rebound, drops will only get in contact with the tops of the pillars, but not with the side walls or the bottom surface. This means that the effective solid-liquid contact area of the drops spreading over an area A_{max} will only contain the area fraction of pillar top surfaces within that area, but not the area fraction of the air for the grooves in between. As a result, this is a perfect surface to compare the drop charging on superhydrophobic surfaces made of nanofilaments or candle soot.

4.4.1 Drop impact conditions

Drop impact experiments were performed under the following conditions:

- Drop Volume: 4 μL
- Weber number: $We = 5 - 15$
- Impact speed: $0.43 - 0.74$ m/s
- Electric field: $E = U/V = 66$ kV/m
- Frame rate : 5000 fps

4.4.2 Drop impact dynamics on Micropillar surfaces

Drops remain in the Cassie state at the proper impact conditions. At certain We, the excess of drop pressure allows the liquid penetration in the space between the pillars, that is, the drop impalement (Cassie-Wenzel transition)

[102–104]. To avoid impalement and facilitate complete rebounds, our experiments were performed in the range $5 < We < 15$. Above $We = 15$ drops impale into the surface, leaving a small drop on it, leading to a partial rebound not suitable for the electric field method (Fig. 4.16a)

The spreading parameter as a function of We on micropillars reveals the same power law as for Teflon surfaces, $R_{max} \sim R_0 We^{0.6}$ (Fig. 4.16b). Accordingly, for both hydrophobic surfaces, drops dissipate in the same way the total initial kinetic energy at the moment of impact. Note that, the power law for micropillars will be valid for the limited range of We described before, where a complete rebound is possible.

Contact time Contact time appears mostly unaltered with changing the release height (Fig. 4.16c), as also reported for superhydrophobic surfaces. This is another confirmation that micropillar surfaces behaves as a superhydrophobic surface below $We = 15$. In consequence, this parameter can be certainly ruled out as an influencing parameter in the charging process. Despite drops remaining in the Cassie state, the contact time on micropillars is longer than on a superhydrophobic surface. The lower hydrophobicity of micropillars leads to more pronounced adhesion forces of drops, which slow down the contact line movement. As a result, contact times of drops impacting on micropillar surfaces are comparable to those for Teflon surfaces.

4.4.3 Drop charging on micropillar surfaces

In the same way that all the surfaces discussed in this thesis, drops charge positively on micropillar array surfaces. Indeed, drops rebound in the same direction of the electric field (Fig. 4.17a), with a horizontal displacement $\Delta x < 0.37\ mm$. This is equivalent to a drop impacting from 1.3 cm height on silicon nanofilaments. The smaller displacements of rebounding drops on micropillars is basically due to its lower rebound heights. This is compensated for a decrease in the flight time of drops ($\Delta t < 37\ ms$) in comparison with superhydrophobic surfaces. Thus, drops rebounding from Micropillar surfaces showed values of

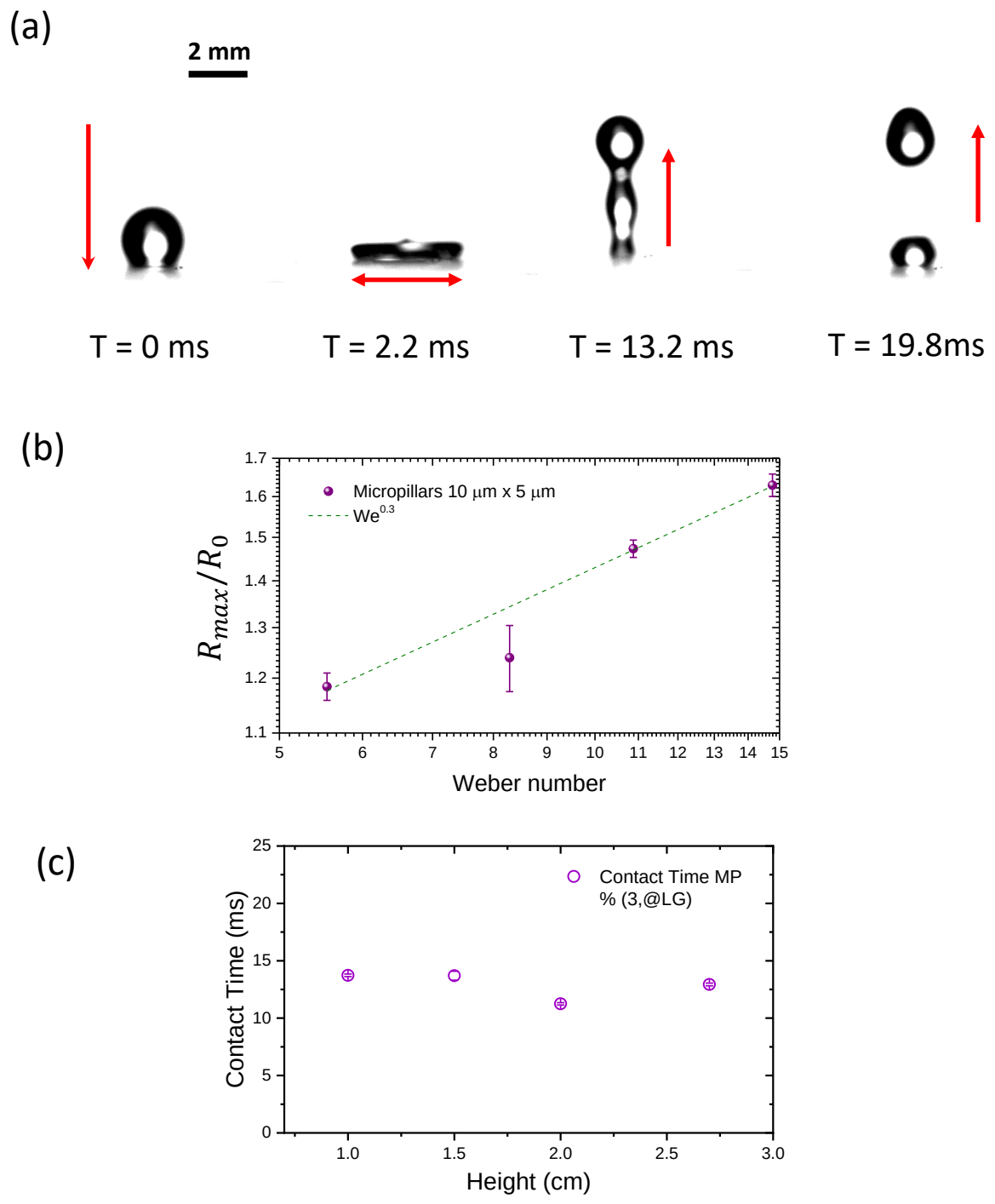

Figure 4.16: (a) Drop impalement on a micropillar array surface. Part of the initial drop volume is left on the surface. (b) Spreading parameter R_{max}/R_0 for micropillar array surfaces as a function of Weber number. The slope of the dashed line is 0.3. (c) Contact time as a function of height for drops impacting on a micropillar array surface.

charge comparable to the case of silicone nanofilaments and candle soot surfaces (Fig. 4.17b)

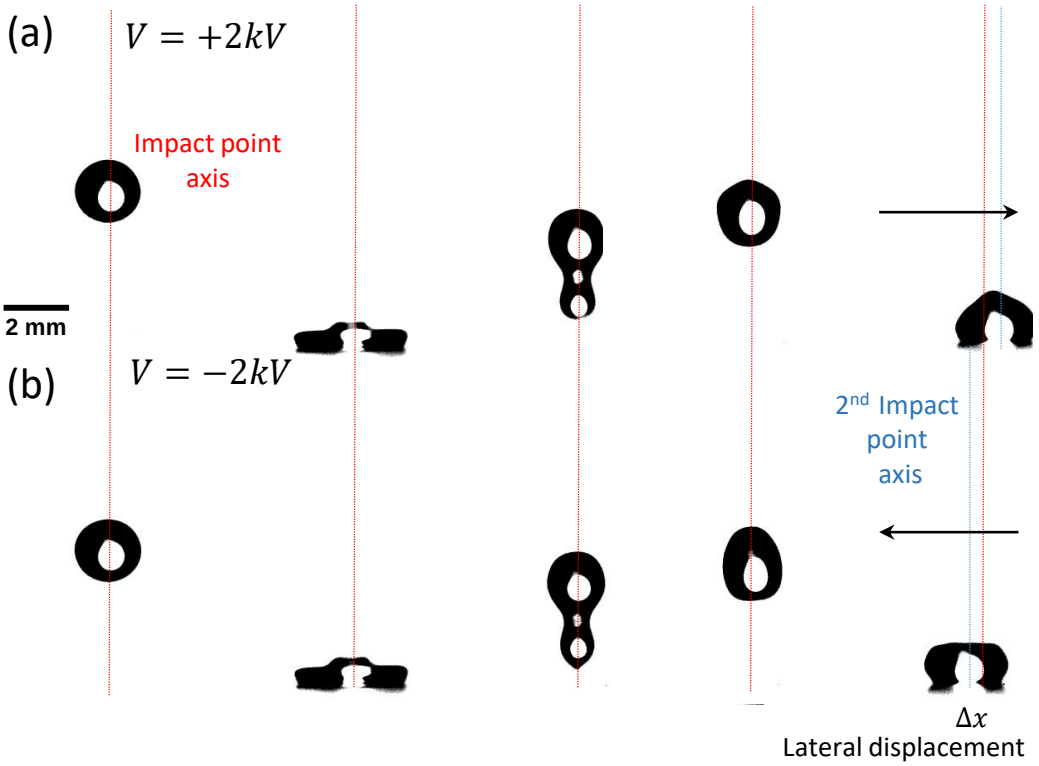

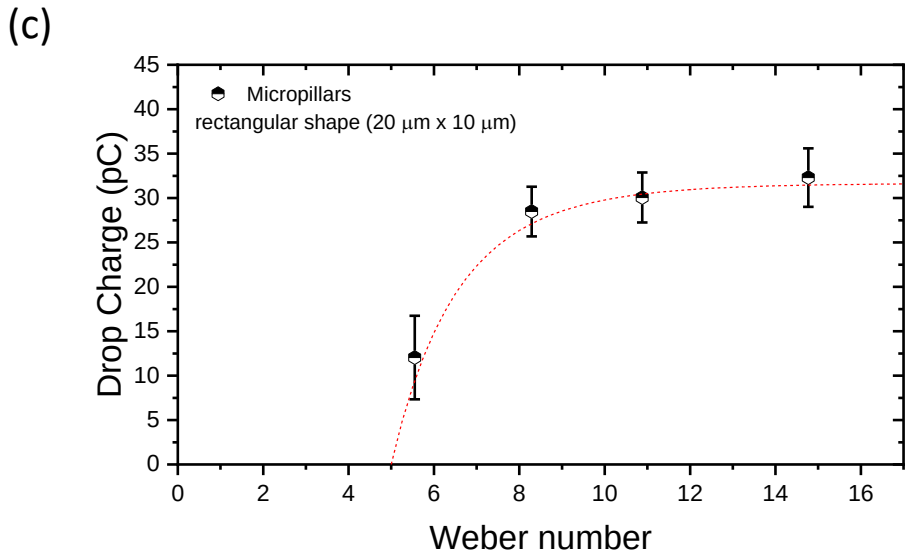

Figure 4.17: (a) 4 μL drop rebounding from micropillars array surfaces under an applied electric field of 66 kV/m. Drops rebound in the direction of the electric field, from left to right. (b) Applying the electric field from right to left (-66kV/m) changes in the same way the rebounding direction, from right to left. (c) Drop charge vs. Weber number for a SU-8 micropillar surface. the red dotted line represents the fit of the theoretical model, with $\sigma_S^0 = 21$ μC/m2 and $\lambda = 0.49$ mm.

Experiments showed that drops reach a charge saturation point of $Q \sim 30$ pC at $We = 8$ (Fig.4.17c), which is lower for the other surfaces studied in this thesis. Fitting eqn. 3.12 into Fig.4.17c leads to the parameters $\lambda_r = 0.49$ mm and $\sigma_S^0 = 21$ μC/m^2. For the case of λ_r, its magnitude is remarkably close to the fluorinated superhydrophobic surfaces ($\lambda_r = 0.57$ mm for SN-FDTS and $\lambda = 0.6$ mm for candle soot), which explains the similar saturation points. On the other hand, the estimated σ_S^0 is slightly higher than the ones found for SN-FDTS and candle soot. As a result, drops saturate faster at lower We on micropillar surfaces.

Since the geometry of pillars is known, the area fraction can be calculated. The area of a rectangular pillar of length l = 10 μm and width $w = 5$ μm is $A_p = l * a = 50$ μm^2. The area fraction covered by a drop will be then:

$$f = \frac{A_p}{A_{LS}} = \frac{l * a}{l + d}, \tag{4.22}$$

where l and w is the length and the width of a rectangular pillar. A_{LS} is the projected liquid-solid contact area, with d as the spacing distance between the pillars, from edge to edge. For our case $A_{LS} = 150$ μm^2, which leads to $f = 1/3$. In particular, drops rebounding at We =15 covers an area apparent area $A_{max} \sim 7$ mm^2. This yields an effective area of ~ 2.3 mm^2, which is actually quite similar to the areas predicted by Cassie-Baxter equation for superhydrophobic surfaces (chapter 3). As a result, samples with similar surface chemistry will charge similarly as drops covers comparable effective contact areas. These results again confirm the contact area as the key parameter to control charging and that charging can be enhanced by maximizing the contact area between the drop and surface.

4.4.4 Summary

In the first part of the chapter, I showed that drops can rebound positively charged from smooth hydrophobic Teflon surfaces. The amount of charge is up to five times higher than the found for superhydrophobic surfaces. This is due

to the difference in the effective drop contact area, as a result of the different wetting states.

Drop charge can be represented as a function of Weber number, based on the scaling law $R_{max} \sim R_0 We^{0.3}$ that correlates R_{max} with We and therefore A_{max}. In addition, I demonstrated that charging can be suppressed importantly when the substrate is a conductor or high permittivity surface. From this fact, I found that the spontaneous charging of drops generates electrostatic forces that affect the drop motion during retraction and after rebound. Forces can be even stronger than gravity and generates due to the negative charge deposited on the surface.

In the second part of the chapter, I studied charging on hydrophobic rectangular shaped micropillars surfaces where drops can rebound in the Cassie state, like superhydrophobic surfaces. I calculated the area fraction covered by a drop during the impact, with values comparable to the estimated effective area for a superhydrophobic surface. The similarities in charging for micropillars and superhydrophobic surfaces gives further support to the contact area as the dominant parameter in drop charging.

Chapter 5

Conclusions and Outlook

In this thesis, I devised one experimental method that enables us to determine the charge of drops rebounding from superhydrophobic and hydrophobic surfaces. The method is based in the deflection of drops by lateral electric fields, combined simultaneously with high-speed video imaging. Furthermore, I derived a theoretical model to explain charge separation of bouncing drops. I showed that drop charge can be maximized by increasing the contact area between the drop and surface. I demonstrated that due to drop charging, self generated electrostatic forces affect the drop impact dynamics. Following this idea, I calculated the electrostatic forces acting on rebounding drops by an energy balance approach, which at the same time serves as a tool for drop charge determination.

In this chapter, I will summarize the main findings and conclusions, with an outlook and potential applications of the results.

Electric field method I showed that measuring the lateral trajectory of drops deflected by electric fields is a precise and reliable method for drop charge detection. There is no need of amplifiers or more sophisticated setups. This method is based on very fundamental physics, based on the electrostatic force experience by a charged drop. One advantage is that the possibility of artefacts is low. In particular, the fact that switching the polarity of the field allows drops jump in the opposite direction, is a quite convincing proof of the existence of

charge separation.

The method can be improved by adding two more high-speed cameras to record the impact process from the top and beneath the drop. In principle, this is useful to analyze with more details the contact area, since it is not necessarily always circular as assumed in this thesis. In addition, it is feasible to assemble the setup inside a chamber for experiments under a more controlled relative humidity. all the experiments presented in this thesis were performed at $30-40\%$ of relative humidity, which is a small variation to affect the charging measurements. Although humidity should influence charge separation only in extreme cases, it has not been tested for drop impact so far. In principle, the setup can be inverted to apply vertical electric fields. A hole can be made in one of the copper plates, while the other plate can be located beneath a superhydrophobic/hydrophobic surface. Applying a vertical electric field would detach an impacting drops faster from the surface, thanks to charge separation occurring at the liquid-solid interface. This would be quite useful in the reduction of contact time, which is crucial in a variety of applications.

Charging on superhydrophobic and hydrophobic surfaces I have shown that drops rebound positively charged upon impact on superhydrophobic and hydrophobic surfaces. This is another evidence that moving contact lines can induce charge separation due to ions naturally present in water. Even secondary drops ejected from the top of the primary drop acquire a positive and lower net charge. I have proposed that the phenomenon occurs due to the formation of an electrical double layer at the liquid-solid interface in the spreading phase, where hydroxyl ions are absorbed by the hydrophobic coating. The double layer is in electrical equilibrium, which is broken during the retraction phase. This leaves a rebounding drop positively charged and the surface with the opposite net charge.

In terms of applications, moving drops by electric fields may be important for sorting, manufacturing, and even the control of chemical reactions at a small scale. The drop manipulation opens new possibility in the collection of charged

drops to harvest energy.

Parameters controlling charging I showed experimentally that charging process is strongly dependent on the effective contact area covered by a drop, which is at the same time dependent on the drop volume and Weber number. I derived a theoretical model based on slide electrification, which is compatible with our experimental findings. The model considers a drop as a capacitor that stores charge up to a certain contact area, assuming the deposition of charge at the drop rim during retraction. The dependence of charging with the contact area explains the notorious difference in charging between hydrophobic and superhydrophobic surfaces. While the first surface describes a Wenzel state, where drops are in contact completely with the surface, the second is characterized by a Cassie state wetting with drops interacting with a fraction of the surface. The amount of charge can be even increased by adding small concentration of salt or increasing the PH. Therefore, charging by drop impact can be enhanced by maximizing contact area of water mixed with salts, which may be important in applications of nanogenerators.

The good agreement between theory and experiments becomes promising to determine the necessary drop impact conditions for reaching a desirable amount of charge. For example, for drops rebounding from fluorinated surfaces, which should have similar surface charge densities, questions such as: What is the proper impact speed to reach 20 pC for a 4μL impacting drop? How much charge does a drop acquire according their apparent contact area? can be in advance answered

From a fundamental perspective, it would be interesting to study successive impacting drops. As drops deposit negative charge on the surface, at some point the surface will saturate and drops cannot acquire more positive charge. This would be the same effect reported for slide electrification phenomenon. However, recording multiple drops is not possible with high speed-video imaging and additional electrodes for charge detection would be required. Besides, another interesting experiment is investigating the effect on charging when adding

surfactants in water. This decreases the surface tension of water, which should lead to longer contact times. As charging is a result of a non-equilibrium process, once electroneutrality of the double layer is disrupted, the contact time between the drop and surface should be crucial in the desorption of hydroxyl ions to recover such electroneutrality.

Changing the viscosity of water by adding glycerol is another possibility to explore. Increasing the viscosity contributes to the viscous dissipation, which can slow down the retraction of impacting drops [86, 105] as the impact speed increases. This certainly should change the contact time and may affect the drop charging.

Self generated electrostatic forces In chapter 4, I have described two indicators of the existence of self generated electrostatic forces due to drop charging. Both indicators were evident for low permittivity substrates. The first indicator corresponds to the retardation of the drop recoil for the surface where charging takes place. Here, negative charges deposited as the drop retracts pull outwards the drop rim by attractive electrostatic forces. The second indicator is quite obvious when the rebounding height is measured. Low permittivity surfaces exhibit lower rebounding heights due to attractive electrostatic forces from the negative surface charges to the positive rebounding drop.

The existence of self-generated electrostatic forces change the way to represent the sources of energy dissipation for impacting drops when charge separation arises. This new insight could be helpful for a better understanding of the underlying dynamics of drop impact. Furthermore, it could also help to characterize precisely the hydrophobicity of surfaces, since restitution coefficients can be underestimated because charging effects are not considered.

Bibliography

[1] Young Soo Joung and Cullen R Buie. Aerosol generation by raindrop impact on soil. *Nature communications*, 6(1):1–9, 2015.

[2] Tristan Gilet and Lydia Bourouiba. Fluid fragmentation shapes rain-induced foliar disease transmission. *Journal of the Royal Society Interface*, 12(104):20141092, 2015.

[3] Delphis F Levia, Sean A Hudson, Pilar Llorens, and Kazuki Nanko. Throughfall drop size distributions: a review and prospectus for future research. *Wiley Interdisciplinary Reviews: Water*, 4(4):e1225, 2017.

[4] Lidiya Mishchenko, Benjamin Hatton, Vaibhav Bahadur, J Ashley Taylor, Tom Krupenkin, and Joanna Aizenberg. Design of ice-free nanostructured surfaces based on repulsion of impacting water droplets. *ACS nano*, 4(12):7699–7707, 2010.

[5] R Andrade, O Skurtys, and F Osorio. Drop impact behavior on food using spray coating: Fundamentals and applications. *Food research international*, 54(1):397–405, 2013.

[6] MS Mahdipoor, F Tarasi, C Moreau, A Dolatabadi, and M Medraj. Hvof sprayed coatings of nano-agglomerated tungsten-carbide/cobalt powders for water droplet erosion application. *Wear*, 330:338–347, 2015.

[7] B-J De Gans, Paul C Duineveld, and Ulrich S Schubert. Inkjet printing of polymers: state of the art and future developments. *Advanced materials*, 16(3):203–213, 2004.

[8] Mostafa Kahani, Robert Gordon Jackson, and Gary Rosengarten. Experimental investigation of tio2/water nanofluid droplet impingement on nanostructured surfaces. *Industrial & Engineering Chemistry Research*, 55(7):2230–2241, 2016.

[9] Alexander L Yarin et al. Drop impact dynamics: splashing, spreading, receding, bouncing. *Annual review of fluid mechanics*, 38(1):159–192, 2006.

[10] Wilhelm Barthlott and Christoph Neinhuis. Purity of the sacred lotus, or escape from contamination in biological surfaces. *Planta*, 202(1):1–8, 1997.

[11] Akira Nakajima, Kazuhito Hashimoto, Toshiya Watanabe, Kennichi Takai, Goro Yamauchi, and Akira Fujishima. Transparent superhydrophobic thin films with self-cleaning properties. *Langmuir*, 16(17):7044–7047, 2000.

[12] Xu Deng, Lena Mammen, Hans-Jürgen Butt, and Doris Vollmer. Candle soot as a template for a transparent robust superamphiphobic coating. *Science*, 335(6064):67–70, 2012.

[13] Chaoyi Peng, Zhuyang Chen, and Manish K Tiwari. All-organic superhydrophobic coatings with mechanochemical robustness and liquid impalement resistance. *Nature materials*, 17(4):355–360, 2018.

[14] Yao Lu, Sanjayan Sathasivam, Jinlong Song, Colin R Crick, Claire J Carmalt, and Ivan P Parkin. Robust self-cleaning surfaces that function when exposed to either air or oil. *Science*, 347(6226):1132–1135, 2015.

[15] H Yıldırım Erbil, A Levent Demirel, Yonca Avcı, and Olcay Mert. Transformation of a simple plastic into a superhydrophobic surface. *Science*, 299(5611):1377–1380, 2003.

[16] Ana C Glavan, Ramses V Martinez, Anand Bala Subramaniam, Hyo Jae Yoon, Rui MD Nunes, Heiko Lange, Martin M Thuo, and George M

Whitesides. Omniphobic "rf paper" produced by silanization of paper with fluoroalkyltrichlorosilanes. *Advanced Functional Materials*, 24(1):60–70, 2014.

[17] Philipp Lenard. *Annalen der Physik*, 282(8):584–636, 1892.

[18] J. J. Thomson. *Philosophical Magazine and Journal of Science*, 37(227):341–358, 1894.

[19] Z. Levin and P.V. Hobbs. *Philosophical Transactions of the Royal Society of London. Series A, Mathematical and Physical Sciences*, 269(1200):555–585, 1971.

[20] D. M. Chate and A. K. Kamra. *Atmos. Res.*, 29(1):115–128, January 1993.

[21] Fernando Galembeck and Thiago AL Burgo. *Chemical Electrostatics*. Springer, 2017.

[22] Daniel J Lacks and Troy Shinbrot. Long-standing and unresolved issues in triboelectric charging. *Nature Reviews Chemistry*, 3(8):465–476, 2019.

[23] Irving Langmuir. *J. Am. Chem. Soc.*, 60(5):1190–1194, 1938.

[24] R. Digilov. *Langmuir*, 16(16):6719–6723, 2000.

[25] Qiang-Qiang Sun, Dehui Wang, Yanan Li, Jiahui Zhang, Sj Ye, Jiaxi Cui, Longquan Chen, Zuankai Wang, Hans-Jürgen Butt, Vollmer Doris, and Xu Deng. *Nature Materials*, 18, 09 2019.

[26] Andrew M. Duffin and Richard J. Saykally. *J. Phys. Chem. C*, 112(43):17018–17022, 2008.

[27] Tom Krupenkin and J Taylor. *Nat. Commun.*, 2:448, 08 2011.

[28] Zhaochu Yang, Einar Halvorsen, and Tao Dong. *Appl. Phys. Lett*, 100:213905, 05 2012.

[29] Jong Moon, Jaeki Jeong, Dongyun Lee, and Hyuk Pak. *Nat. Commun.*, 4:1487, 02 2013.

[30] Zong-Hong Lin, Gang Cheng, Long Lin, Sangmin Lee, and Zhong Lin Wang. *Angew. Chem. Int. Ed.*, 52(48):12545–12549, 2013.

[31] Soon-Hyung Kwon, Junwoo Park, Won Keun Kim, YoungJun Yang, Eungkyu Lee, Chul Jong Han, Si Yun Park, Jeongno Lee, and Youn Sang Kim. *Energy Environ. Sci.*, 7:3279–3283, 2014.

[32] Yanbo Xie, Diederik Bos, Lennart de Vreede, Hans de Boer, Mark-Jan Meulen, Michel Versluis, Ad Sprenkels, Albert Van den Berg, and Jan Eijkel. *Nat. Commun.*, 5:3575, 04 2014.

[33] Li Zheng, Zong-Hong Lin, Gang Cheng, Wenzhuo Wu, Xiaonan Wen, Sangmin Lee, and Zhong Wang. *Nano Energy*, 9:291–300, 10 2014.

[34] Qijie Liang, Xiaoqin Yan, Gu Yousong, Kui Zhang, Mengyuan Liang, Shengnan Lu, Xin Zheng, and Yue Zhang. *Scientific reports*, 5:9080, 03 2015.

[35] L. E. Helseth and X. D. Guo. *Langmuir*, 31(10):3269–3276, 2015.

[36] Hao Wu, Niels Mendel, Dirk van den Ende, Guofu Zhou, and Frieder Mugele. *Phys. Rev. Lett.*, 125:078301, Aug 2020.

[37] Thomas Young. Iii. an essay on the cohesion of fluids. *Philosophical transactions of the royal society of London*, (95):65–87, 1805.

[38] Arthur Mason Worthington and Robert Bellamy Clifton. Xxviii. on the forms assumed by drops of liquids falling vertically on a horizontal plate. *Proceedings of the Royal Society of London*, 25(171-178):261–272, 1877.

[39] Arthur Mason Worthington. On impact with a liquid surface. *Proceedings of the Royal Society of London*, 34(220-223):217–230, 1883.

[40] Karl Kaehler. Über die durch wasserfälle erzeugte leitfähigkeit der luft. *Annalen der Physik*, 317(13):1119–1141, 1903.

[41] George Clarke Simpson. Xv. on the electricity of rain and its origin in thunderstroms. *Philosophical Transactions of the Royal Society of London. Series A, Containing Papers of a Mathematical or Physical Character*, 209(441-458):379–413, 1909.

[42] J.J. Nolan. Electrification of water by splashing and spraying. *Proceedings of the Royal Society of London. Series A, Containing Papers of a Mathematical and Physical Character*, 90(621):531–543, 1914.

[43] Ph Lenard. Über wasserfallelektrizität und über die oberflächenbeschaffenheit der flüssigkeiten. *Annalen der Physik*, 352(12):463–524, 1915.

[44] Robert N Wenzel. Resistance of solid surfaces to wetting by water. *Industrial & Engineering Chemistry*, 28(8):988–994, 1936.

[45] ABD Cassie and SJToTFS Baxter. Wettability of porous surfaces. *Transactions of the Faraday society*, 40:546–551, 1944.

[46] Ralf Blossey. Self-cleaning surfaces—virtual realities. *Nature materials*, 2(5):301–306, 2003.

[47] Ivan P Parkin and Robert G Palgrave. Self-cleaning coatings. *Journal of materials chemistry*, 15(17):1689–1695, 2005.

[48] Nenad Miljkovic, Daniel Preston, Ryan Enright, and Evelyn Wang. *Nat. Commun.*, 4:2517, 09 2013.

[49] James K. Beattie. *Lab Chip*, 6:1409–1411, 2006.

[50] Vishal Tandon, Sharath K Bhagavatula, Wyatt C Nelson, and Brian J Kirby. *J. Electrophor.*, 29(5):1092—1101, March 2008.

[51] T. Preočanin, A. Selmani, P. Lindqvist-Reis, F. Heberling, N. Kallay, and J. Lützenkirchen. *Colloids Surf. A*, 412:120–128, 2012.

[52] Konstantin N Kudin and Roberto Car. Why are water- hydrophobic interfaces charged? *Journal of the American Chemical Society*, 130(12):3915–3919, 2008.

[53] Kyoko Yatsuzuka, Yukio Mizuno, and Kazutoshi Asano. *J. Electrostat.*, 32(2):157–171, 1994.

[54] L. E. Helseth and H. Z. Wen. *Eur. J. Phys.*, 38(5):055804, September 2017.

[55] L. E. Helseth. *Langmuir*, 35(25):8268–8275, 2019.

[56] Amir Shahzad, K. Rohana Wijewardhana, and Jang-Kun Song. *Appl. Phys. Lett.*, 113(2):023901, 2018.

[57] Amy Z. Stetten, Dmytro S. Golovko, Stefan A. L. Weber, and Hans-Jürgen Butt. *Soft Matter*, 15:8667–8679, 2019.

[58] Mariana D. Sosa, M. Luz Martínez Ricci, Leandro L. Missoni, Daniel H. Murgida, Antonela Cánneva, Norma B. D'Accorso, and R. Martín Negri. Liquid–polymer triboelectricity: chemical mechanisms in the contact electrification process. *Soft Matter*, 16:7040–7051, 2020.

[59] Mariana D Sosa, Norma B D'Accorso, M Luz Martinez Ricci, and R Martin Negri. Liquid–polymer contact electrification: Modeling the dependence of surface charges and ξ-potential on ph and added-salt concentration. *Langmuir*, 38(29):8817–8828, 2022.

[60] Shiquan Lin, Mingli Zheng, Jianjun Luo, and Zhong Lin Wang. Effects of surface functional groups on electron transfer at liquid–solid interfacial contact electrification. *ACS nano*, 14(8):10733–10741, 2020.

[61] Diego Díaz, Diana Garcia-Gonzalez, Pravash Bista, Stefan A. L. Weber, Hans-Jürgen Butt, Amy Stetten, and Michael Kappl. Charging of drops

impacting onto superhydrophobic surfaces. *Soft Matter*, 18:1628–1635, 2022.

[62] Diego Díaz, Xiaomei Li, Pravash Bista, Xiaoteng Zhou, Fahimeh Darvish, Hans-Jürgen Butt, and Michael Kappl. Self-generated electrostatic forces of drops rebounding from hydrophobic surfaces. *Physics of Fluids*, 35(1):017111, 2023.

[63] R Shuttleworth and GLJ Bailey. The spreading of a liquid over a rough solid. *Discussions of the Faraday Society*, 3:16–22, 1948.

[64] C Huh and SG Mason. Effects of surface roughness on wetting (theoretical). *Journal of colloid and interface science*, 60(1):11–38, 1977.

[65] DW Pilat, P Papadopoulos, D Schaffel, Doris Vollmer, Rüdiger Berger, and H-J Butt. Dynamic measurement of the force required to move a liquid drop on a solid surface. *Langmuir*, 28(49):16812–16820, 2012.

[66] Abhinav Naga. *Capillary interactions in wetting: rotation of particles at interfaces and removal of particles by drops.* PhD thesis, Johannes Gutenberg-Universität Mainz, 2021.

[67] Douglas A Olsen, Powell A Joyner, and Marvin D Olson. The sliding of liquid drops on solid surfaces. *The Journal of Physical Chemistry*, 66(5):883–886, 1962.

[68] Robert Tao-Ping Chow et al. On the ability of drops or bubbles to stick to non-horizontal surfaces of solids. *Journal of Fluid Mechanics*, 137:1–29, 1983.

[69] CW Extrand and AN Gent. Retention of liquid drops by solid surfaces. *Journal of Colloid and Interface Science*, 138(2):431–442, 1990.

[70] Yile Wang, Yage Zhao, Lijie Sun, Abbasali Abouei Mehrizi, Shiji Lin, Jianwei Guo, and Longquan Chen. Successive rebounds of impinging

water droplets on superhydrophobic surfaces. *Langmuir*, 38(12):3860–3867, 2022.

[71] Romain Rioboo, Cameron Tropea, and Marco Marengo. Outcomes from a drop impact on solid surfaces. *Atomization and sprays*, 11(2), 2001.

[72] Mathilde Reyssat, Anne Pépin, Frédéric Marty, Yong Chen, and David Quéré. Bouncing transitions on microtextured materials. *EPL (Europhysics Letters)*, 74(2):306, 2006.

[73] Denis Bartolo, Farid Bouamrirene, Emilie Verneuil, Axel Buguin, Pascal Silberzan, and Sébastien Moulinet. Bouncing or sticky droplets: Impalement transitions on superhydrophobic micropatterned surfaces. *EPL (Europhysics Letters)*, 74(2):299, 2006.

[74] Yizhou Shen, Xinghua Wu, Jie Tao, Chunling Zhu, Yuekun Lai, and Zhong Chen. Icephobic materials: Fundamentals, performance evaluation, and applications. *Progress in Materials Science*, 103:509–557, 2019.

[75] Tanmoy Maitra, Carlo Antonini, Manish K Tiwari, Adrian Mularczyk, Zulkufli Imeri, Philippe Schoch, and Dimos Poulikakos. Supercooled water drops impacting superhydrophobic textures. *Langmuir*, 30(36):10855–10861, 2014.

[76] Chonglei Hao, Yahua Liu, Xuemei Chen, Jing Li, Mei Zhang, Yanhua Zhao, and Zuankai Wang. Bioinspired interfacial materials with enhanced drop mobility: From fundamentals to multifunctional applications. *Small*, 12(14):1825–1839, 2016.

[77] Meirong Song, Zhaohui Liu, Yongjian Ma, Zhichao Dong, Yilin Wang, and Lei Jiang. Reducing the contact time using macro anisotropic superhydrophobic surfaces—effect of parallel wire spacing on the drop impact. *NPG Asia Materials*, 9(8):e415–e415, 2017.

[78] Thomas M Schutzius, Stefan Jung, Tanmoy Maitra, Patric Eberle, Carlo Antonini, Christos Stamatopoulos, and Dimos Poulikakos. Physics of icing

and rational design of surfaces with extraordinary icephobicity. *Langmuir*, 31(17):4807–4821, 2015.

[79] D Richard and D Quéré. Bouncing water drops. *Europhysics Letters (EPL)*, 50(6):769–775, jun 2000.

[80] Christophe Clanet, Cédric Béguin, Denis Richard, and David Quéré. Maximal deformation of an impacting drop. *Journal of Fluid Mechanics*, 517:199–208, 2004.

[81] Fujun Wang, Lei Yang, Libing Wang, Yong Zhu, and Tiegang Fang. Maximum spread of droplet impacting onto solid surfaces with different wettabilities: Adopting a rim–lamella shape. *Langmuir*, 35(8):3204–3214, 2019.

[82] Jiayu Du, Xiong Wang, Yanzhi Li, Qi Min, and Xinxin Wu. Analytical consideration for the maximum spreading factor of liquid droplet impact on a smooth solid surface. *Langmuir*, 37(24):7582–7590, 2021.

[83] Jens Eggers, Marco A Fontelos, Christophe Josserand, and Stéphane Zaleski. Drop dynamics after impact on a solid wall: theory and simulations. *Physics of fluids*, 22(6):062101, 2010.

[84] Yang Zhu, Hao-Ran Liu, Kai Mu, Peng Gao, Hang Ding, and Xi-Yun Lu. Dynamics of drop impact onto a solid sphere: spreading and retraction. *Journal of Fluid Mechanics*, 824, 2017.

[85] Fujun Wang and Tiegang Fang. Retraction dynamics of water droplets after impacting upon solid surfaces from hydrophilic to superhydrophobic. *Physical Review Fluids*, 5(3):033604, 2020.

[86] Binyu Zhao, Xiang Wang, Kai Zhang, Longquan Chen, and Xu Deng. Impact of viscous droplets on superamphiphobic surfaces. *Langmuir*, 33(1):144–151, 2017.

[87] Hans-Jürgen Butt, Karlheinz Graf, and Michael Kappl. *Physics and chemistry of interfaces*. John Wiley & Sons, 2013.

[88] David C Grahame. The electrical double layer and the theory of electrocapillarity. *Chemical reviews*, 41(3):441–501, 1947.

[89] C. S. Tian and Y. R. Shen. *Proc. Natl. Acad. Sci. U. S. A.*, 106(36):15148–15153, 2009.

[90] Robert Andrews Millikan. On the elementary electrical charge and the avogadro constant. *Physical Review*, 2(2):109, 1913.

[91] KL Brown and GW Tautfest. Faraday-cup monitors for high-energy electron beams. *Review of Scientific Instruments*, 27(9):696–702, 1956.

[92] Dongwhi Choi, Horim Lee, Do Jin Im, In Seok Kang, Geunbae Lim, Dong Sung Kim, and Kwan Hyoung Kang. Spontaneous electrical charging of droplets by conventional pipetting. *Scientific reports*, 3(1):1–7, 2013.

[93] Junping Zhang and Stefan Seeger. Silica/silicone nanofilament hybrid coatings with almost perfect superhydrophobicity. *ChemPhysChem*, 14(8):1646–1651, 2013.

[94] Jie Liu, Yuling Sun, Xiaoteng Zhou, Xiaomei Li, Michael Kappl, Werner Steffen, and Hans-Jürgen Butt. One-step synthesis of a durable and liquid-repellent poly (dimethylsiloxane) coating. *Advanced Materials*, 33(23):2100237, 2021.

[95] Enrique S Quintero, Guillaume Riboux, and José Manuel Gordillo. Splashing of droplets impacting superhydrophobic substrates. *Journal of Fluid Mechanics*, 870:175–188, 2019.

[96] Xiaomei Li, Pravash Bista, Amy Z Stetten, Henning Bonart, Maximilian T Schür, Steffen Hardt, Francisco Bodziony, Holger Marschall, Alexander

Saal, Xu Deng, et al. Spontaneous charging affects the motion of sliding drops. *Nature Physics*, pages 1–7, 2022.

[97] M Pasandideh-Fard, YM Qiao, Sanjeev Chandra, and Javad Mostaghimi. Capillary effects during droplet impact on a solid surface. *Physics of fluids*, 8(3):650–659, 1996.

[98] Jae Bong Lee, Dominique Derome, Ali Dolatabadi, and Jan Carmeliet. Energy budget of liquid drop impact at maximum spreading: Numerical simulations and experiments. *Langmuir*, 32(5):1279–1288, 2016.

[99] S Santosh Kumar, Ashish Karn, Roger EA Arndt, and Jiarong Hong. Internal flow measurements of drop impacting a solid surface. *Experiments in Fluids*, 58(3):1–9, 2017.

[100] M Pasandideh-Fard, YM Qiao, Sanjeev Chandra, and Javad Mostaghimi. Capillary effects during droplet impact on a solid surface. *Physics of fluids*, 8(3):650–659, 1996.

[101] Jae Bong Lee, Dominique Derome, Ali Dolatabadi, and Jan Carmeliet. Energy budget of liquid drop impact at maximum spreading: Numerical simulations and experiments. *Langmuir*, 32(5):1279–1288, 2016.

[102] M Reyssat, A Pépin, F Marty, Y Chen, and D Quéré. Bouncing transitions on microtextured materials. *Europhysics Letters (EPL)*, 74(2):306–312, apr 2006.

[103] Matheu Broom and Geoff R Willmott. Water drop impacts on regular micropillar arrays: The impact region. *Physics of Fluids*, 34(1):017115, 2022.

[104] Wei Fang, Hao-Yuan Guo, Bo Li, Qunyang Li, and Xi-Qiao Feng. Revisiting the critical condition for the cassie–wenzel transition on micropillar-structured surfaces. *Langmuir*, 34(13):3838–3844, 2018.

[105] Xu Deng, Frank Schellenberger, Periklis Papadopoulos, Doris Vollmer, and Hans-Jurgen Butt. Liquid drops impacting superamphiphobic coatings. *Langmuir*, 29(25):7847–7856, 2013.